ABSTRACT

NONLINEAR OPTICAL PROPERTIES OF NOVEL NANOSTRUCTURED ION IMPLANTED AND LASER ABLATED SILICON USING FEMTOSECOND PULSE EXCITATION

by

Elaine N. Lalanne

The study of the nonlinear optical properties of novel nanostructured ion implanted and laser ablation of Silicon is motivated by the need for materials that exhibit large values of the real part of the third order nonlinear susceptibility ($\chi^{(3)}_{Re}$). This property is essential for light controlled phase or refractive index modulation at low power, where the optical properties are used for optical switching devices. Previous nanosecond (ns) measurements indicated values of -2.8×10^{-5} esu ($\lambda = 532$ nm) for $\chi^{(3)}_{Re}$.

The characterization of nonlinear optical properties of the samples was studied by the Z-scan techniques using ~ 100 fs pulses. The Z-scan technique is a relatively simple and direct measurement of both the real and imaginary part of $\chi^{(3)}$, where the nonlinear refractive index (n_2) is related to $\chi^{(3)}_{Re}$ and the nonlinear absorption (β) to $\chi^{(3)}_{Im}$. Femtosecond pulse excitation measurements were performed to study ultrafast dynamics by inducing nonlinear optical changes, such as photo-induced absorption and measuring the nonlinear response. For fast optical switching applications, a fast and relatively large electronic nonlinearity is required.

NONLINEAR OPTICAL PROPERTIES OF NOVEL NANOSTRUCTURED ION IMPLANTED AND LASER ABLATED SILICON USING FEMTOSECOND PULSE EXCITATION

by

Elaine Nicole Lalanne

A Dissertation
Submitted to the Faculty of
New Jersey Institute of Technology and
Rutgers, The State University of New Jersey - Newark
in Partial Fulfillment of the Requirements for the Degree of
Doctor of Philosophy in Applied Physics

Federated Physics Department

May 2003

APPROVAL PAGE

NONLINEAR OPTICAL PROPERTIES OF NOVEL NANOSTRUCTURED ION IMPLANTED AND LASER ABLATED SILICON USING FEMTOSECOND PULSE EXCITATION

Elaine Nicole Lalanne

May 2003

Dr. Anthony M. Johnson, Thesis Advisor
Distinguished Professor of Physics, NJIT

Dr. John Federici
Acting Chairperson and Professor of Physics, NJIT

Dr. Haim Grebel
Professor of Electrical and Computer Engineering, NJIT

Dr. Trevor Tyson
Associate Professor of Physics, NJIT

Dr. Richart Slusher
Head, Optical Physics Research Department, Bell Labs, Lucent Technologies

BIOGRAPHICAL SKETCH

Author: Elaine Nicole Lalanne

Degree: Doctor of Philosophy

Date: May 2003

Undergraduate and Graduate Education:

- Doctor of Philosophy in Applied Physics,
  New Jersey Institute of Technology, Newark, NJ, 2003

- Bachelor of Arts in Physics,
  Wellesley College, Wellesley, MA, 1994

Major: Applied Physics

Presentations and Publications:

E. Lalanne, A. M. Johnson, Z. Iqbal, H. Grebel,
"Femtosecond non-degenerate pump-probe measurements of single-wall carbon nanotubes (SWCNTS) within an ordered array of nanosize silica spheres",
Quantum Electronics & Laser Science Conference (QELS), June 1-6, 2003.
Baltimore, Maryland.

H. Han, S. Vijayalakshmi, A. Lan, Z. Iqbal, H. Grebel, E. Lalanne, A. M. Johnson,
"Linear and nonlinear optical properties of single-walled carbon nanotubes within an ordered array of nanosized silica spheres" App. Phys. Lett., 82, 1458 (2003).

E.Lalanne, A.M Johnson, S. Vijayalakshmi, H. Grebel,
"Femtosecond Z-scan and Pump-probe Measurements of Silicon Nanoclusters Made by Laser Ablation And Ion Implantation", National Society of Black Physicists.
March 13-17, 2002, Huntsville, Alabama.

E. Lalanne, A. M. Johnson, S. Vijayalakshmi, H. Grebel,
"Femtosecond Z-scan and Pump-probe Measurements of Silicon Nanoclusters Made by Laser Ablation And Ion Implantation", IEEE Laser & Electro-Optics Society (LEOS) Annual Conference, November 11-15, 2001, San Diego, California.

E. Lalanne, A. M. Johnson, S. Vijayalakshmi, H. Grebel,
"Nonlinear Optical Properties of Silicon Nanoclusters Made By Laser Ablation and Ion Implantation", Optical Society Of America (OSA) Annual Conference, Long Beach, California, October 16-18, 2001.

E. Lalanne, H. Garcia, A .M. Johnson, S. Vijayalakshmi, H. Grebel,
"Nonlinear Optical Properties of Silicon Nanoclusters Made By Laser Ablation and Ion Implantation", Conference Lon Lasers and Electro-Optics (CLEO), Baltimore, Maryland May 8-10, 2001.

E. Lalanne, H, Garcia, A. M. Johnson, S. Vijayalakshmi, H. Grebel,
"Nonlinear Optical Properties of Silicon Nanoclusters Made By Laser Ablation and Ion Implantation", March Centennial American Physical Society (APS) conference, Atlanta, Georgia, March 20-26, 1999.

E. Lalanne, H, Garcia, A. M. Johnson, S. Vijayalakshmi, H. Grebel,
"Nonlinear Optical Properties of Silicon Nanoclusters Made By Laser Ablation", National Society of Black Physics Student, Fisk University, Nashville, Kentucky, March 4-7, 1998.

E. Lalanne, H, Garcia, A. M. Johnson, S. Vijayalakshmi, H. Grebel,
"Nonlinear Optical Properties of Silicon Nanoclusters Made By Laser Ablation", International Quantum Electronics Conference (QELS), San Francisco, California, May 3-8, 1998.

A woman who is convinced that she deserves to accept only the best challenges herself to give the best. Then she is living phenomenally.

When life surrounds me with problems,
I remember
no question can be asked
if the answer is not
already in the universe.
— Maya Angelou

This dissertation is dedicated to my grandmother, Anne Elizabeth Dorlus, who recently passed away, my parent, Nicholas and Bernadette Lalanne, my brothers, John, Nicky, Moses, Nils and Joshua. I would also like to thank my friends for their love and support, especially Hernando, Leslie, and Paulette.

ACKNOWLEDGEMENTS

I would like to thank Professor Johnson for his ongoing support throughout the years. He has constantly provided me with advice and encouragement. He has shared his vast knowledge of ultrafast optics; I would like to express my deepest appreciation.

I would like to thank my committee for their assistance. Professor Grebel for providing the samples that were used in my research and for the many helpful discussions. Special thanks to Professor Federici for his support during my graduate years. Professor Tyson, for his willingness to serve on the committee. Special thanks to Dr. Slusher for his valuable insight and for giving me the opportunity to work at Bell Labs for the summer.

Finally, there are no words to express my appreciation for the love and support of my family throughout my graduate school experience.

TABLE OF CONTENTS

TABLE OF CONTENTS
(Continued)

LIST OF TABLES

LIST OF FIGURES

LIST OF FIGURES

(Continued)

LIST OF FIGURES

(Continued)

CHAPTER 1

INTRODUCTION

Nano-particle materials have been in existence since medieval times with the use of colored glass in Cathedrals. More recently, semiconductor nanostructures have garnered considerable interest because of their potential application as optical switching and optical limiting photonic devices. Nano-composite materials show unique electrical and optical properties, which are not observed in bulk materials. These materials have generated an enormous amount of research and development, particularly in silicon microstructures and nanostructured materials.[1-4] The technological advantage of using such materials is its compatibility with Si based optoelectronics. These novel Silicon materials, made by ion implantation and laser ablation techniques, have been shown to have interesting nonlinear optical properties.[1,2] In the case of the laser ablated material, it has been shown to exhibit large values of the real part of the third order nonlinear susceptibility, $\chi_{\mathrm{Re}}^{(3)}$, and have potentially fast response times.[1,2] These two properties are essential for fast light controlled phase or refractive index modulation at low powers. These nonlinear optical properties are useful for applications such as optical switching devices in the telecommunication industry.

Most networking equipment today is still based on electronic-signals, meaning that the optical signals have to be converted to electrical ones, to be amplified, regenerated or switched, and then reconverted to optical signals.[5] This is generally referred to as an 'optical-to-electronic-to-optical' (OEO) conversion and is a significant bottleneck in transmission. Huge amounts of information traveling around an optical network needs to be switched through various points known as nodes. Information arriving at a node will be forwarded on

towards its final destination via the best possible path, which may be determined by such factors as distance, cost, and the reliability of specific routes.[5] The conventional way to switch the information is to detect the light from the input optical fibers, convert it to an electrical signal, and then convert that back to a laser light signal, which is then sent down the fiber you want the information to go back out on. For example, in a long-haul network, an OEO conversion may occur as often as every 600 kilometers just for amplification. However, optical switching technology is still very much in its infancy .[5]

One application of these novel silicon type structures with an enhanced nonlinearity is to construct an all-optical switching device such as a Mach-Zehnder interferometer (Fig.1a, 1b) [6]. In optical switching, light controls light with the help of a nonlinear optical material. It makes use of direct or indirect effects that occurs at the atomic or molecular level when the presence of light alters the atomic susceptibility or the photon absorption rates of the medium[6]. In this configuration, the input light is split into two inteferometric arms where the nonlinear material is placed in one arm. When the beam interacts with the nonlinear material, it induces a change in the refractive index of the medium through a $\chi^{(3)}$ process, which in turn imparts a nonlinear phase shift to the electric field as it exits. If the change in the phase shifts is a given multiple of π, then the two beams will still be in phase. When they are recombined, they will interfere constructively and it will be detected at the output. If there isn't any change in the phase then the two beams will interfere destructively and a signal will be not detected at the output. This technique may be integrated in a Silicon based optoelectronic telecommunication systems using intense optical pulses and nanostructured ion-implanted or laser ablated silicon as the nonlinear medium to switch out information stored in the beam to various locations.[5,6] Additionally, the advantage of

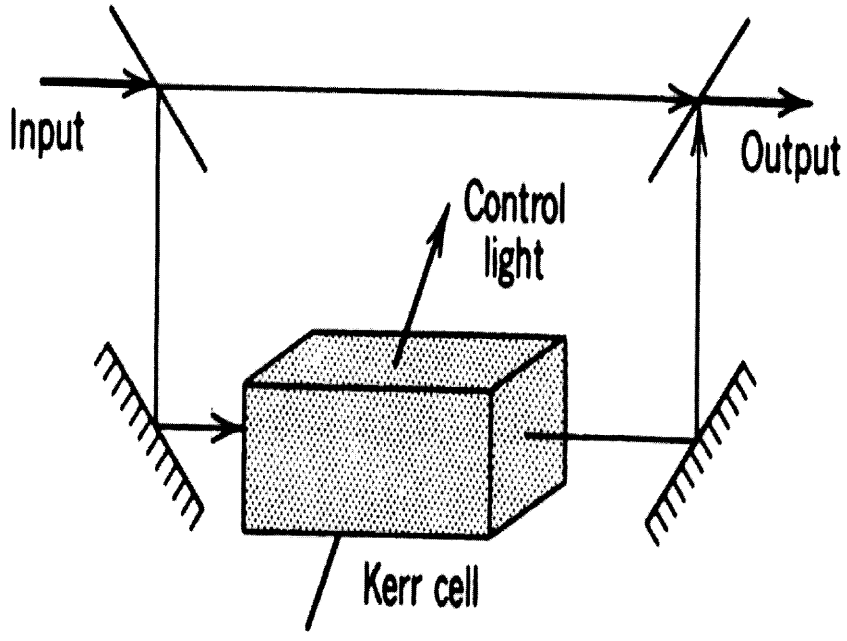

Figure 1.a: An all-optical on-off switch using a Mach-Zender interferometer and a material exhibiting Kerr effect.[6]

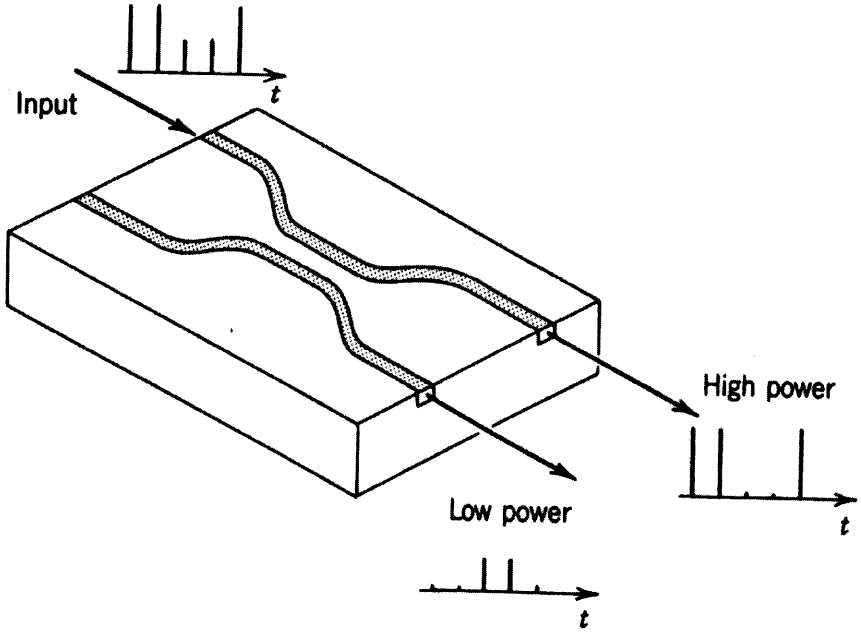

Figure 1.b: A directional coupler controlled by the optical Kerr effect.[6]

incorporating novel silicon structures is that most electronic systems are silicon based. The uses for optical switches are numerous. One such application for optical switching is add-drop multiplexing where it is used to add and drop specific wavelengths from multi-wavelength signals to avoid electronic processing. Additionally, it can be used for fiber restoration and protection switching, where small-size switches are used to restore optical paths in the event of link failure. Another example is its use, as signal monitoring where wavelength-selective switches are commonly used.[5]

To determine the effectiveness of these materials as nonlinear components a thorough investigation of its nonlinear optical properties is required. The benefit of studying various materials with ultrashort intense coherent light is that it is a non-invasive method that avoids permanent damage or destruction of the material. The use of intense ultrashort pulses allows the characterization of the nonlinear optical properties at high intensity but at low average power. Furthermore, ultrashort pulses make it possible to measure the lifetime of optically induced dynamics.

In section 1.1, a basic overview of the properties of bulk silicon and its technological appeal will be given. I will also discuss the various source of enhancement of the nonlinear optical properties due to modification of the energy bandgap. A review of the fabrication processes of these novel structures of silicon made by laser ablation and ion implantation will be examined in section 1.2 and 1.3.

1.1 Background Information Of Silicon

Silicon is the principal material used in the semiconductor industry. The supply for silicon is abundant in that the earth's crust consists of 28% silicon.[7] Therefore; it's non-toxic and environmentally safe. Its bandgap (1.12 eV) is large enough to allow for operation at room temperature because of its stable and sufficient electrical properties. It also has a direct bandgap at 3.4 eV. It possesses fairly large heat conductivity. Its oxide, silicon dioxide (SiO_2), behaves as a good insulator and enables the processing of more than 10^8 transistors on a single chip.[7] However, due to its small and indirect band gap, silicon is inadequate for use in optical applications.

In bulk silicon, light emission is a phonon-mediated process with millisecond recombination lifetime and extremely inefficient. The recombination time is the duration it takes for the electrons at the minimum of the conduction to merge with the holes at the maximum of the valence band. Additionally, the rate of radiative recombination is much lower than non-radiative recombination lifetime. This is a direct consequence in that the majority of electron-hole pairs created optically recombine non-radiatively.[7] Furthermore, the luminescence in silicon has low quantum efficiency. This makes it impossible for its usage as a lasing medium where the main requirement for lasers is large population inversion. In the case of silicon, free carrier or Auger absorption prevents this.

To overcome the features, which prevent the use of silicon as a viable optical material, the leading approach is to modify the electronic energy states of silicon. There are mainly two ways in which this is achieved. The first is to reduce the size of the particles to the order of nanometers.[3] In this case, quantum size effect or confinement plays a major role.

In decreasing the volume in one to three dimensions, it causes the restructuring of electronic density of states that modifies the energy bandgap such as changing an indirect bandgap to a direct bandgap. This can be achieved in quantum dots, wires and wells. In most materials, the confinement of carriers to a small volume results in an increase of the electronic bandgap. The other method of manipulating the energy states of a medium is to introduce defects, which modifies the atomic bonds on the surface.[3] The surface states strongly influence the distribution of the energy states. In the case of silicon nanocomposites, surface energy states can or will alter the energy distribution as well as quantum size effects since atoms are either on the surface or a few lattices sites away. Both methods of transforming the energy states can produce significant efficient radiative recombination over bulk silicon enabling a larger optical nonlinearity for optical applications.[3]

The first silicon nanostructured material studied was porous silicon. It demonstrated reasonably efficient luminescence at room temperature in 1990. Porous silicon consisted of pores and undulating wires, which appeared spongy.[3] The size of the particles is on the order of a few nanometers (nm). It is fabricated using electrochemical anodization with Hydrofluoric acid (Hf) based solutions. The preparation of porous silicon consisted of a teflon cup positioned on the front surface of a silicon wafer and an electrical contact placed on the back surface of the wafer. Hf solution is injected into the front surface and a voltage is applied between the electrodes in the Hf liquid and the electrical contact. This process initiated the dissolution of the silicon and creation of pores ensues.

The fabrication of silicon nanocomposite materials has grown using various methods such as Porous silicon, Plasma-enhanced chemical vapor deposition (PECVD), Laser Ablation, Ion-implantation and Molecular Beam Expitaxy (MBE). The materials under

investigation were made using two different fabrication techniques, which will be discussed in the following sections. They are laser ablation and ion-implantation method.

1.2 Fabrication Of Silicon Nanoclusters By Laser Ablation

Laser ablation otherwise known as pulsed laser deposition entails the removal of material from a target to form a thin film that is then deposited unto a substrate.[1-3] The advantage of the laser ablation process is that it can generate a highly forward directed and closely packed plume of materials that can be deposited with less contamination. Pulsed laser deposition is precise in that it allows one to deposit film with thickness in the nm range. This technique is also a non-equilibrium deposition technique due to the resultant ablation of the material. This non-equilibrium process produces the same composition in the thin film as in the original material, yet may result in different crystal symmetry. The process involves using a focused beam of ultra-violet (uv) pulses with high peak power, which are directed onto a solid target surface (i.e. silicon wafer), where the laser's energy ablates the target's surface. The uv light for most material is only absorbed by the outermost layer of the target, approximately 100 nm in thickness. The procedure results in an explosion of vaporized and ejected fragments of the molecular species. The vaporized substance forms a plume and is deposited as a thin film unto a substrate placed in the path of the ejected particles. The resulting thin film is composed of particles whose size distribution is a function of the sample material and the laser's power density. The characteristics of the laser ablated sample and its structure is contingent on the quality of the material.

The laser ablated Si NC's are fabricated using pulses from a KrF excimer laser with an average power of 3 W focused unto a Si wafer (<100>) in a vacuum chamber. The

wavelength of the beam is 248 nm with a temporal width of 8ns[1,2]. The target of silicon wafer is n-type with a doping level of 10^{+16} cm^{-3}. The resulting plume from the Si wafer is deposited unto a quartz substrate positioned 3 cm away from the target.[1,2] X-ray diffraction and Raman scattering have shown that the resultant film consists of micron-sized droplets (2-3 μm). X-ray photolectron data revealed that the nature of the film's structure is comprised of a silicon microstructure with little surface oxide.[1,2] The film is composed of 3-20 μm size microstructures linked by a smooth featureless matrix. X-ray diffraction has also indicated that the Si NCs are crystalline in nature, where a strong peak was found at <111> in contrast to the target orientation <100>. The morphology of the resulting film is identical to the silicon wafer. However, the crystallography is different. The crystalline nature of the silicon wafer target is cubic where approximately 75% of the deposited thin film is hexagonal-wurtzite in nature and the remainder of the crystallites is cubic.[8] Electron diffraction confirmed the crystal symmetry of the micro-droplets. The symmetry of the featureless matrix is unknown. A TEM image indicated that the clusters are composed of micron size crystals, which are surrounded by nanocrystals. Due to the directional nature of the plume, the samples possessed three regions with varying thickness: 100 nm, 200 nm, and 400 nm.

Additional investigation of the laser-ablated samples was performed by confocal scanning micro-Raman spectroscopy. The spatial resolution is 1 μm across the micron-sized structures. Two different spectra were obtained for the sample with cubic and hexagonal crystal structures (Appendix A). The Raman signal that was attributed to the cubic silicon crystallites was detected at a frequency 519.8 cm^{-1} with a linewidth of 6.2 cm^{-1}. In comparison, for single crystal silicon, the Raman signal is 520 cm^{-1} with a linewidth of 4.5 cm^{-1}. For the 75% of the composition of the laser ablated thin film that is hexagonal-wursite,

the Raman signals were observed at either 516 or 518 cm^{-1}.[51] The corresponding linewidths were 7 cm^{-1} for both peaks. The characteristic of the Raman spectrum for hexagonal structure should contain three peaks. The two peaks are due to vibrations of horizontal plane of the hexagonal layers and one peak is attributed to the vertical plane. However, only two types of peaks were detected. This is due to the fact that two of the peaks overlapped, which may have produced a single inhomogeneously broadened line, as in the case for the hexagonal-wursite structure in diamond. For the area surrounding the microstructures, which consist of nanocrystals, the Raman signal shows a broad spectrum with peak at 480 cm^{-1}. This data is consistent with the observed spectra for amorphous silicon thin films and results taken from electron diffraction data [8].

1.3 Ion Implantation

Si NCs made by ion implantation were also studied by taking advantage of the fact that the size distribution, the precise control of dosage and depth of nano-particles can be controlled in a uniform manner. Ion implantation is the process of using high energetic ions to implant various species into a given substrate. The ions are accelerated to very large kinetic energy and are driven into the target where the dopants are implanted. Through the collisions process with either the nuclei or the electrons within the substrates, the ions lose energy. The collision with both bound and free electrons typically occurs for higher energy and lighter ions. The displacement of the target nuclei usually occurs when lower energy and heavier ions are used.[9,10] As the ions collide with the substrate's nuclei, the nuclei break free from the lattice sites, which unintentionally cause damage to the material. Due to the damage, the SiO_2 atoms are displaced which creates vacancies and self-interstitials of SiO_2 in the lattices.

Because the silicon ions are situated in the interstitial sites they are not electrically active. However, during the annealing process in the material at high temperatures, the majority of the damage to the substrate is repaired. Annealing causes the repositioning of the dopants and the dislocated target nuclei back into the lattice sites. The depth of which the ions can travel is dependent on the ion's velocity and its concentration. The ion implanted Si NC's studied are made by Si (400 KeV) implanted into a fused silica substrate followed by annealing (1000° C) in flowing Ar + 4%H_2.[2] The implantation dose is 6 x $10^{17}cm^{-2}$ with a peak excess Si concentration of 2 x $10^{22}cm^{-3}$. The resultant nanoclusters have a mean size distribution of 5-6 nm and the film thickness of 300 nm. The clusters are spherical and crystalline. Previous measurements done at Oak Ridge National Laboratory demonstrated photoluminescence in both the visible and the near infrared regions.[9] The ion-implanted sample was excited at 488 nm and the luminescence was measured at 650 nm before annealing. The observed photoluminescence was attributed to defects in the silica (SiO_2) substrate cause by the fabrication process. After the annealing process in Ar + 4%H_2 at a temperature of 1100 °c, the silicon nanocrystals began to take form. Again luminescence studies were performed and a more pronounced photoluminescence spectrum was observed at 750 nm. It is believed that the photoluminescence in the ion-implanted samples may have originated either from quantized states or from localized surface/interface states. Furthermore, transient absorption spectra have indicated two ps photoinduced absorption features in the ion-implanted samples. The relaxation of the high-energy band reveals that the population of quantized states is short-lived and is caused by surface trapping[3]. This suggests that the Si/SiO_2 interface states may play an important role in the relaxation of photoexcited carriers.

The bandgap, E_g, may be approximated by analyzing the absorption spectra. In the case of amorphous semiconducting material, the linear absorption, α, is related to E_g as follows:

$$(\alpha E)^{1/2} = \beta(E - E_g) \tag{1.1}$$

Plotting $(\alpha E)^{1/2}$ as a function of E gives a linear relationship with an x-intercept of E_g. The linear plot gives a value of 2.5 eV for the bandgap[9]. This model fits except at low and higher energies. The deviation at higher energies is attributed to absorption saturation and leads to discrepancies in determining the band tails at lower energies.

1.4 Experimental Technique

Previous measurements using nanosecond (ns) pulses from a frequency doubled Q-switched Nd:YAG laser, have indicated values of $\approx 10^{-4}$ esu (λ = 532 nm) for $\chi^{(3)}_{Re}$ and a lifetime of 5 ns, limited only by the laser pulse width[1] for the laser ablated Si NC. In comparison to silica fiber ($\chi^{(3)}_{Re} \approx 10^{-14}$ esu) and porous Si ($\chi^{(3)}_{Re} \approx 10^{-9}$ esu), $\chi^{(3)}_{Re}$ for Si NC's is significantly larger[2]. Further investigation with ultrashort pulses (ps and fs) could lead to a better understanding of the underlying physics.

The nonlinear optical properties of the Silicon nanocrystals were determined by the use of a femtosecond tunable Ti:sapphire laser ((λ: 720-1000 nm) and a regenerativly amplified Ti:sapphire laser. Descriptions of the various laser sources and the characterization of the laser pulses are given in Chapter 2.

I use the Z-scan technique to calculate the nonlinear optical properties of Si NCs[5]. This technique is useful because it can be done at low power. Z-scan allows one to measure

both the real and imaginary part of the third order nonlinear susceptibility ($\chi^{(3)}$) of a material. A detailed description of the Z-scan technique and the experimental analysis is given in Chapter 4.

In order to investigate phenomena that occur on a timescale less than a nanosecond (ns) in duration, one has to use ultrashort pulses. In the various experiments use to study Silicon nanostructures, femtosecond (10^{-15}s) pulses are used. The pump-probe technique enables one to measure the relaxation time of the photo-induced absorption of a given system by using a strong pulse to excite the system and a weaker pulse to probe the system. This allows us to look at the transient transmission changes induced by the excitation pulses. A comprehensive explanation of this method is given in Chapter 5.

CHAPTER 2

EXPERIMENTAL APPARATUS

2.1 Introduction

In this chapter, the main experimental apparatus used to carry out the investigation of the nonlinearity of Silicon nanoclusters will be described. The major components are the modelocked Ti:sapphire laser and the Ti:sapphire regenerative amplifiers. They both produce femtosecond pulses and prove extremely useful in investigating various phenomena that occurs in the ps and fs range in biological, chemical and semiconductors media. A description of the supplementary support equipments such as silicon photodiodes, oscilloscopes and optical spectrum analyzer will be given.

2.2 The Lasers

The Ti:sapphire femtosecond laser system, manufactured by Spectra-Physics, supplies the ultrashort optical pulses for the nonlinear optical measurements[11]. The arrangement of the system, as shown in figure 2.1, consists of four lasers: a Ti:sapphire oscillator (Tsunami), a Ti:sapphire regenerative amplifier (Spitfire-50), an Argon-Ion laser (Beamlok) and a Nd:YLF laser (Merlin). The Ti:sapphire laser and Ti:sapphire regenerative amplifier are the central core of the system while the other two lasers are their optical pumps, respectively. The Ti:sapphire oscillator provides the seed pulses to the Ti:sapphire regenerative amplifier to produce higher energetic pulses with maximum of 10 μJ energy per pulse.[12]

2.2.1 Ti:sapphire Laser

The Ti:sapphire ($Ti:Al_2O_3$) laser is an ultrafast laser and has the broadest tunability in terms of wavelength (670-1100 nm).[11] It also offers the best long-term stability and reliability in both femtosecond and picosecond domains. The laser can operate in both the fs or ps mode with a few changes of optics. Currently it is running in the fs mode. The laser is comprised of ten mirrors in a folded cavity designed for minimal space. The gain medium of the laser is a Ti:sapphire crystal whose surface is cut at Brewster angle to generate parallel (p) polarized light in the resonant cavity. The operation of the laser is as follow (see Fig 2.2). The lasing cavity is situated between the high-reflector mirror (M1) and the output coupler (M10). The Spectra-Physics Beamlok Argon Ion laser pump beam with average power of 12 W and a wavelength range of 458-514 nm is directed by and focused into the lasing medium by mirror pairs (P1, P2) where second mirror is concave to focus the beam. The Ti:sapphire crystal adsorbs the pump beam and light is emitted over a broad range of wavelengths (600-1000 nm). However lasing is only achieved for wavelengths greater than 660 nm because of the overlap between the longer wavelength of the absorption band and the short wavelength end of emission band. The residual pump beam passed through mirror 2 and into a beam dump.

The scattered emission normal to the surface of the cavity-focusing mirror (M2) is directed toward the high reflector (M1) and back to M2 which focuses the infrared light to a narrow line within the rod further amplifying the emitted light. It then bounces off of a second cavity-focusing mirror (M3), which collimates the light and directs it to a pair of folding mirrors (M4, M5).[11] Four prisms (Pr_1- Pr_4) are inserted into the resonant cavity to compensate for positive group velocity dispersion (GVD), the natural pulse spreading in

the Ti:sapphire crystal and the other optical elements in the cavity. The other optical elements are used to direct the infrared light back and forth through the lasing medium for amplification.

The Ti:sapphire laser self-mode locks which frees it from using external element to achieve modelocking.[13] If the laser is operating in a pulsed mode, the focused intensity inside the Ti:sapphire crystal exceeds 10^{11} W/cm^2 – sufficient to induce a strong nonlinear lens which quite significantly focuses the pulse. If this occurs in a laser cavity, which is adjusted for, optimum efficiency without this lens, this self-focusing will simply contribute to loss within the laser cavity. However, modest displacement of one mirror away from the optimum cw position by only 0.5 – 1 mm can result in decreased in loss in the laser cavity when Kerr lensing is present. Thus, the Kerr lensing couples the spatial and temporal modes of the oscillator, resulting in two distinct spatial and temporal modes of operation (cw and pulsed)[14]. The Ti:sapphire requires a starting mechanism for the Kerr lens. Modelocking is initiated by introducing a periodic loss through the use of acoustic-optic-modulator (AOM). AOM is also used to maintain the modelocking. An alternate approach is to use a moving mirror to introduce losses or rapping on the table to start the self-focusing mechanisms.[14]

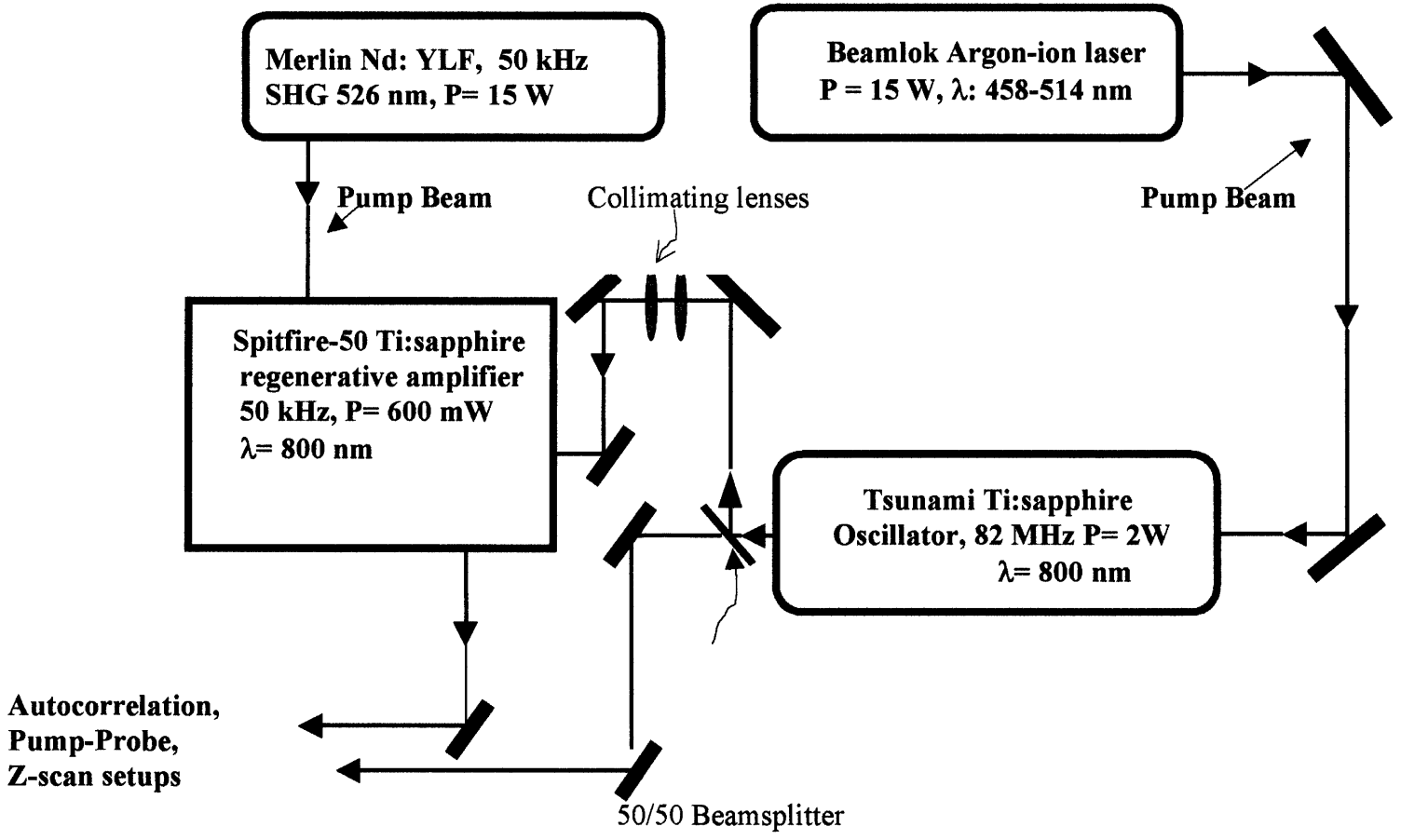

Figure. 2-1 Layout of Ti:sapphire femtosecond laser system

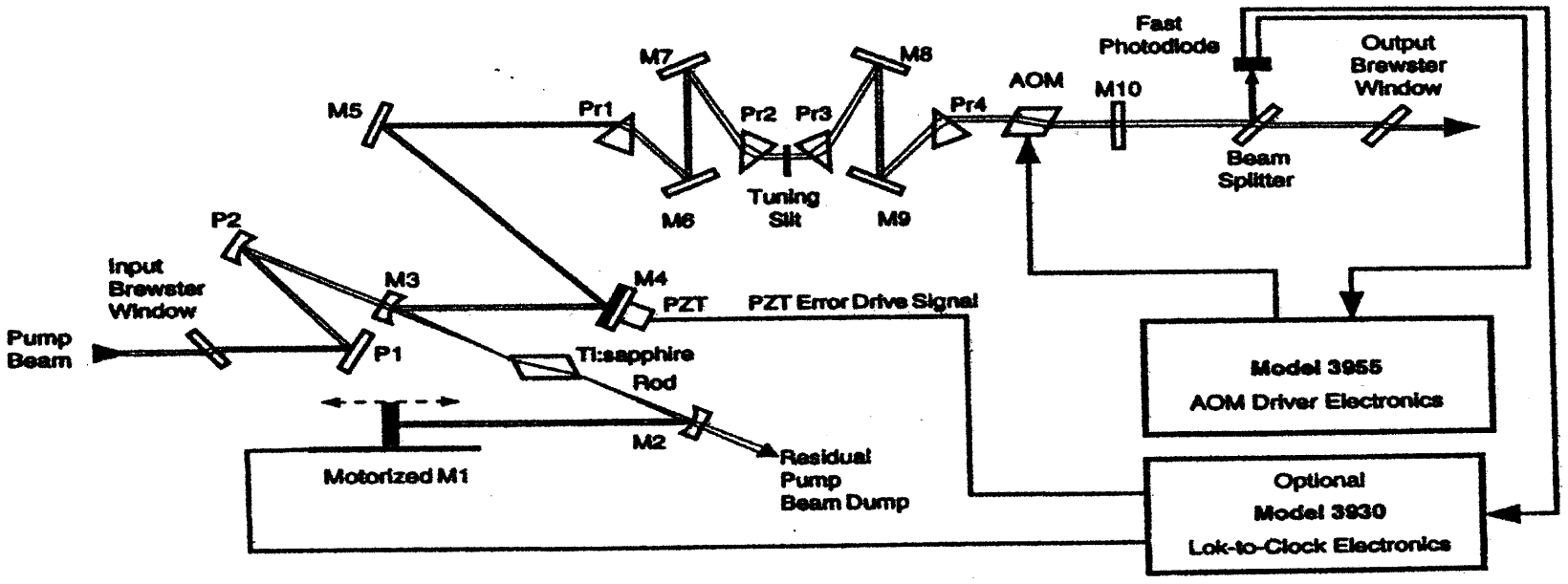

LEGEND

P1: Pump directing mirror
P2: Pump focusing mirror
M3: Cavity focus mirror
M2: Cavity focus mirror
M1: High reflector
M4: Cavity fold mirror
M5: Cavity fold mirror
Pr1: Prism
M7: Mirror
Pr2: Prism
Pr3: Prism
M8: Mirror
M9: Mirror
M10: Output Coupler

Figure. 2.2: Layout of the Spectra Physics Ti:sapphire laser femtosecond configuration[11]

2.2.2 Regenerative Amplifier Ti:sapphire

For some materials, the peak power from the Ti:sapphire laser is not intense enough to observe certain nonlinear processes. In order to produce energetic pulses with energy greater than 1 μJ per pulse, the pulses are amplified through an additional gain medium. In this case, the pulse train from the Spectra-Physics Tsunami (Ti:sapphire) laser is amplified by a Ti:sapphire regenerative amplifier (Spitfire-50) laser.[12] This system uses the chirped pulse amplification (CPA) technique to amplify the pulse without the risk of damaging the optical components in the system. The concept behind CPA is a scheme to increase the energy of a short pulse, while avoiding very high peak powers in the laser amplification process itself.[14] This is done by lengthening the duration of the pulse being amplified, by dispersing, or "chirping" it in a reversible fashion, using the technique of optical pulse compression, developed by Treacy and Martinez.[15,16] By lengthening the pulse in time, energy and be efficiently extracted from the laser gain medium, while avoiding damage to the optical amplifier.[14] This is necessary because pulses with intensity greater than $10\,^{GW}/_{cm^2}$ has the tendency to self-focus thereby increasing the peak power and destructively impact the laser rod. The chirped pulse amplification process occurs as the pulse train from the Tsunami is stretched and then propagate through a gain medium (Ti:sapphire rod), which is pumped by a doubled-frequency Q-switched Nd:YLF (Merlin-50) laser operating at 50 kHz with an average power of 15 W and at 527 nm. Typically, the amplification through the laser rod is minor with the pulses going back and forth through the gain medium 3 times. However with the regenerative amplification technique, it allows the pulses to travel through the Ti:sapphire rod many times consequently producing higher peak power. Afterward it is compressed to nearly the

same pulsewidth as the initial pulses. The Spitfire-50 laser consists of four main components, optical pulse stretcher, Ti:sapphire amplification system , optical pulse compressor and the synchronization electronics.

2.2.2.1 The Stretcher. To produce higher peak power without damaging the laser rod and optics, the pulses are first temporally broaden using a diffraction grating by decreasing its peak power. Before the pulse train is directed toward the stretcher, it first passes through a Faraday isolator, which prevents destabilizing optical feedback to the Tsunami.[12] The Faraday isolator consists of three elements, two polarizes and a Faraday rotator. The beam, which is horizontally polarized, first passes through the input polarizer, which rotates the polarization by 90^0. It then is directed through the Faraday rotator, which changes the polarization by an additional 45^0. The output polarizer, which has been aligned 45° relative to the input polarizer, will then let the light pass through unimpeded. Furthermore, any reflected light from the output polarizer is blocked because it is rotated perpendicularly to the plane of polarization of the input polarizer as it passes back through the Faraday rotator.

The pulse stretcher contains a diffraction grating and folded beam paths to minimize space (Fig.. 2.3a, 2.3c).[12] The transmitted beam from the Faraday isolator is then directed toward the stretching component through the vertically retro-reflecting mirrors. The light is diffracted by the grating and is transmitted toward a curved mirror, which focused the beam to a flat end mirror. The grating causes the beam to disperse where the red edge of the pulse travels shorter distance that the blue edge. The curve

mirror has two basic functions; it serves to make the pulse positively chirped by reversing the group velocity dispersion and changes the height so it can be pick off when it bounces off the grating a second time. At this point the beam is shifted vertically below the input beam. Then the beam retraces it path back to the grating. It then reflects off the grating to the vertical retroreflector where the beam is redirect upwards by it. At this point the beam is spatially broadened. To spatially reconstruct the beam, the beam is then rerouted back toward the grating by the vertical retroreflector at different heights. Within its whole journey inside the stretcher, the beam hits the grating four times, twice on its way to the focusing mirror and twice after being reflected by vertical retroreflector.

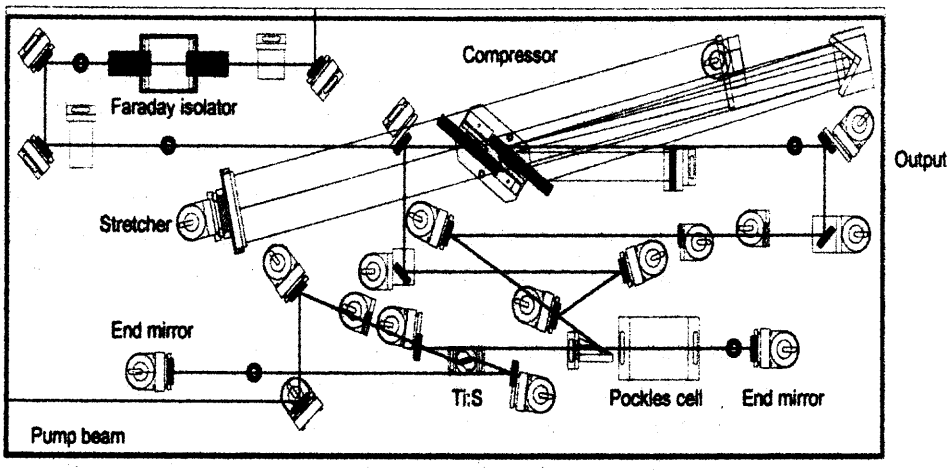

Figure 2.3a Layout of the Ti:sapphire regenerative amplifier laser (Spitfire-50)[12]

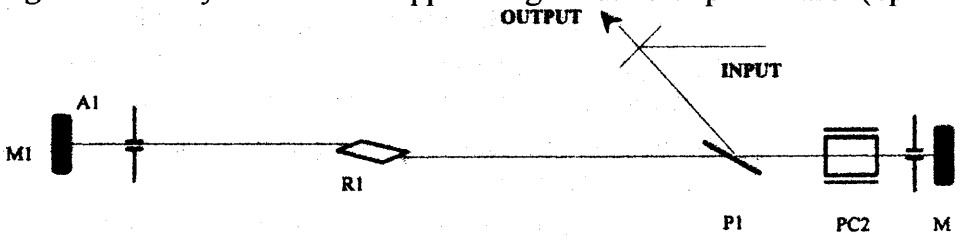

M1, M2	Resonator end mirror	A1	Aperture
PC1	Pockels cell.	P1	Output polarizer
R1	Ti:Sapphire laser rod.		

Figure 2.3b Resonator layout[12]

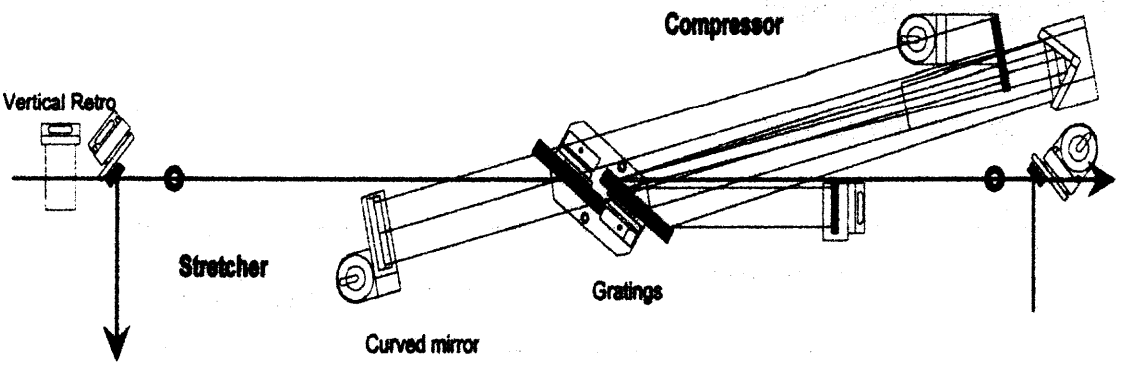

Figure 2.3c Pulse stretcher and compressor layout[12]

On the return from the grating it bounces off from a pick-off mirror, that directs the beam to the amplifier section of the Spitfire. At this point the temporal pulsewidth is in the picoseconds time scale and s-polarized.

2.2.2.2 Amplifier. The lasing medium is also a Ti:sapphire (at Brewster angle) rod which is optically excited by 20 μs second pulse from the frequency doubled Q-switched Nd:YLF laser at 526 nm with an average power of 15 W(Fig.. 2.3a, 2.3b). A Pockels Cell and polarizer are placed within the cavity. The vertically polarized seed pulses are injected into the regenerative amplifier cavity by the reflection from a polarizer. The Pockels cell can change its polarization with an applied biased voltage time synchronized with the Q-switch timing. The amplifier cavity consist of a Ti:sapphire rod as the gain medium, two resonator mirrors (M1, M2), polarizer and a Pockels cell. The elongated 82 MHz pulse train is injected into the cavity by the reflection off the polarizer. The Pockels cell is situated between the polarizer and the M2. The Pockels cell operates as a gate, which allows a single pulse to enter the regenerative amplifier cavity. A DC bias voltage is applied to the Pockels cell that allows it to behave as a static quarter waveplate for 800 nm. When there is no pump beam present the pulses are ejected out of the cavity after a single roundtrip. However, when the pump beam is present, the Q-switch signal activates the Pockels cell to begin the amplification process. The pulses enter the resonator from the reflection off the face of the laser rod. The pulses passes through the Pockels cell and when it is reflected by M2 it retraces it step it has undergone a half wave rotation because it has traveled through the Pockels cell twice. As the pulse leave the Pockels cell a biased voltage is applied to it where it now acts a half waveplate. Consequently, the pulse is

trapped within the resonator. This pulse then makes approximately 20 roundtrips through the resonator cavity where it has experience a gain of over 10^5. Then a quarter-wave voltage is applied to the Pockels cell, causing a half-wave rotation to the pulse after it has transverse through the Pockels cell. The pulse is then ejected from the resonator by the polarizer because the polarization of the pulse is perpendicular to that of the polarizer.

Regenerative amplifiers, seeded by low energy laser pulses, are an extremely efficient means of obtaining high energy and high peak power pulses. The benefit of the regenerative amplification process is its ability to confine, by polarization a single pulse (switched out from a mode-locked pulse train), amplify it to an appropriate energy level, then cavity switch out.[12,14]

2.2.2.3 The Compressor. The compressor reverses the effect of the stretcher and compresses the pulse to near its original pulsewidth (Fig. 2.1a, 2.1c). The compressor is comprised of a grating, and horizontal and vertical retroreflectors. The grating in the compressor exhibits negative group delay and can therefore be used to compensate the dispersion imposed by materials.[12, 14] The compressor is configured in a manner such that the redder frequencies travel the longest path and hence move toward the bluer frequencies. The ejected beam from the regenerative amplifier resonator cavity is directed toward the grating. The grating reflects the broadened beam towards a horizontal retro-reflector. The beam is sent back to the grating, however, it has beam displaced horizontally by two inches. The beam retraces it path and bounces off a vertical retroreflector, which shifts its position vertically. The beam then returns to the grating, spatially broadened at this point. When the beam passes through the compressor

a second time, the stretching is reversed and the pulse is compressed close to its original duration.

2.3 Autocorrelation

Before any experiments are initiated, the temporal width of the pulse must be determined. A common technique for pulse measurement utilizes the optical pulse itself. The intensity profile of the optical pulse is correlated with itself by mixing two optical pulses in a nonlinear optical medium to yield sum frequency generation (second harmonic generation in this case, SHG). The intrinsic speed of this electronic nonlinearity is on the order of 10^{-15}. This speed is utilized in the measurement of the pulsewidth.[17,19]

Nonlinear optical techniques for pulse measurement do not provide a direct display of the pulse shape but give instead measurements of the correlation function. The second-order autocorrelation function of the intensity I(t) is given by

$$G^{(2)}(\tau) = \int_{-\infty}^{\infty} I^{(\omega)}(t) I^{(\omega)}(t+\tau) dt \qquad (2.1)$$

where τ is the optical delay between the two pulses. This is the function we obtain by SHG in BBO since the SHG intensity $I^{(2\omega)}(\tau)$ is proportional to the product of the intensities of the two fundamental pulses

$$I^{(2\omega)}(\tau) \propto G^{(2)}(\tau) \qquad (2.2)$$

If $I^{(\omega)}(\tau)$ is a single isolated pulse, $G^{(2)}(\tau)$ vanishes for large delay τ and its half-width provides a measure of the duration of $I^{(\omega)}(\tau)$. Precise determination of a pulsewidth requires further knowledge about the shape of $I^{(\omega)}(\tau)$. $G^{(2)}(\tau)$ is always symmetric regardless of any symmetry in $I^{(\omega)}(\tau)$ as can be seen from the nature of equation 2.1.

We utilized noncollinear background-free SHG in a 1 mm Beta Barium Borate (BBO) nonlinear crystal to measure $G^{(2)}(\tau)$ of the Ti:sapphire oscillator and 50 KHz regenerative Ti:sapphire amplifier. The output from the laser was divided and directed into two arms of a modified Michelson interferometer. The relative time delay between the two beams was achieved by leaving one arm of the interferometer fixed and varying the other by Newport MM 3000 Translation stage with incorporated stepper motor. The translation stage has a total travel range of 10 mm with a resolution step size of 0.1 μm.

The two beams, parallel but noncollinear were focused into the BBO crystal. These fundamental beams were blocked, by appropriate beams stops, upon passage through the BBO crystal. Second harmonic generation proportional only to the product of the two beams intensities, is detected at an angle bisecting the angle between the two focused fundamentals beams. The BBO crystal was oriented for phase matching at this angle bisecting the two beams. Thus second harmonic radiation was produced only when both pulses were present in the crystal, thereby elimination a background signal (background-free SHG).

The detection systems consisted of a silicon photodiode detector whose output was filtered by an EG&G lock-in amplifier. One arm of the interferometer was chopped at 1.5 kHz by an EG&G Chopper which provided the reference signal for the lock-in amplifier. A schematic experimental setup for the autocorrelation measurement is illustrated in Fig. 2.4. The computer read the signal from the lock-in amplifier triggered by the pulses from the stepper motors and the plots the signal as a function of relative time delay. The temporal resolution depended upon ability to accurately control the path

difference between the two arms of the interferometer (0.1 μm step size) and the speed of the electronic nonlinearity responsible for SHG.

The optical autocorrelation function of the Ti:sapphire oscillator is shown in Fig. 2.4 As mentioned earlier, to obtain the precise pulse duration from the FWHM of $G^{(2)}(\tau)$, some form for the shape of $I^{(\omega)}(\tau)$ must be assumed. The pulses out of the Ti:sapphire laser are hyperbolic secant and its pulse shape is expressed[18]

$$I(t) = \sec h^2\left[\frac{1.76t}{\Delta t_p}\right] \tag{2.2}$$

A simple division of τ_{auto} by a factor of 1.55 will give the real value for the temporal width of the pulse.[18] The pulses are also transform-limited The full-width half-maximum of an autocorrelation trace, t_{ac}, is related to that of the original pulses, t_p, by a constant, P, such that

$$\tau_p = \frac{\tau_{auto}}{P} \tag{2.3}$$

The value of P depends on the pulse shape. For the Ti:sapphire laser the pulse shape is assumed to be $sech^2$ and for background free intensity autocorrelations P =1.543. The pulses are transform limited where the time-bandwidth product, $\Delta\tau\Delta\omega$, is 0.315. Time bandwidth describes the relationship between the pulse duration and its spectral bandwidth. These quantities are related through the Heiseberg Uncertainty Principle, $\Delta\omega\Delta t \geq k$ [18,19]. For a Gaussian beam, k is 0.441. An experimental autocorrelation trace of the pulses from the Ti:sapphire laser at 800 nm (τ_p = 77 fs) is depicted in Fig. 2.5. A typical autocorrelation trace for 150 fs amplified pulse generated by the 50 KHz

regenerative Ti:sapphire amplifier at 800 nm is shown in figure 2.6. In this case the pulse shape is Gaussian however, the pulses are near transform-limited where the time-bandwidth product is multiplied by a factor of 1.5. The intensity profile for a Gaussian pulse shape is expressed as [18]

$$I(t) = \exp\left[\frac{-2\sqrt{\ln 2}t}{\Delta\tau_p}\right] \tag{2.4}$$

where the constant P that relates the temporal pulse width, $\Delta\tau_p$, to $\Delta\tau_{auto}$ is $\sqrt{2}$.

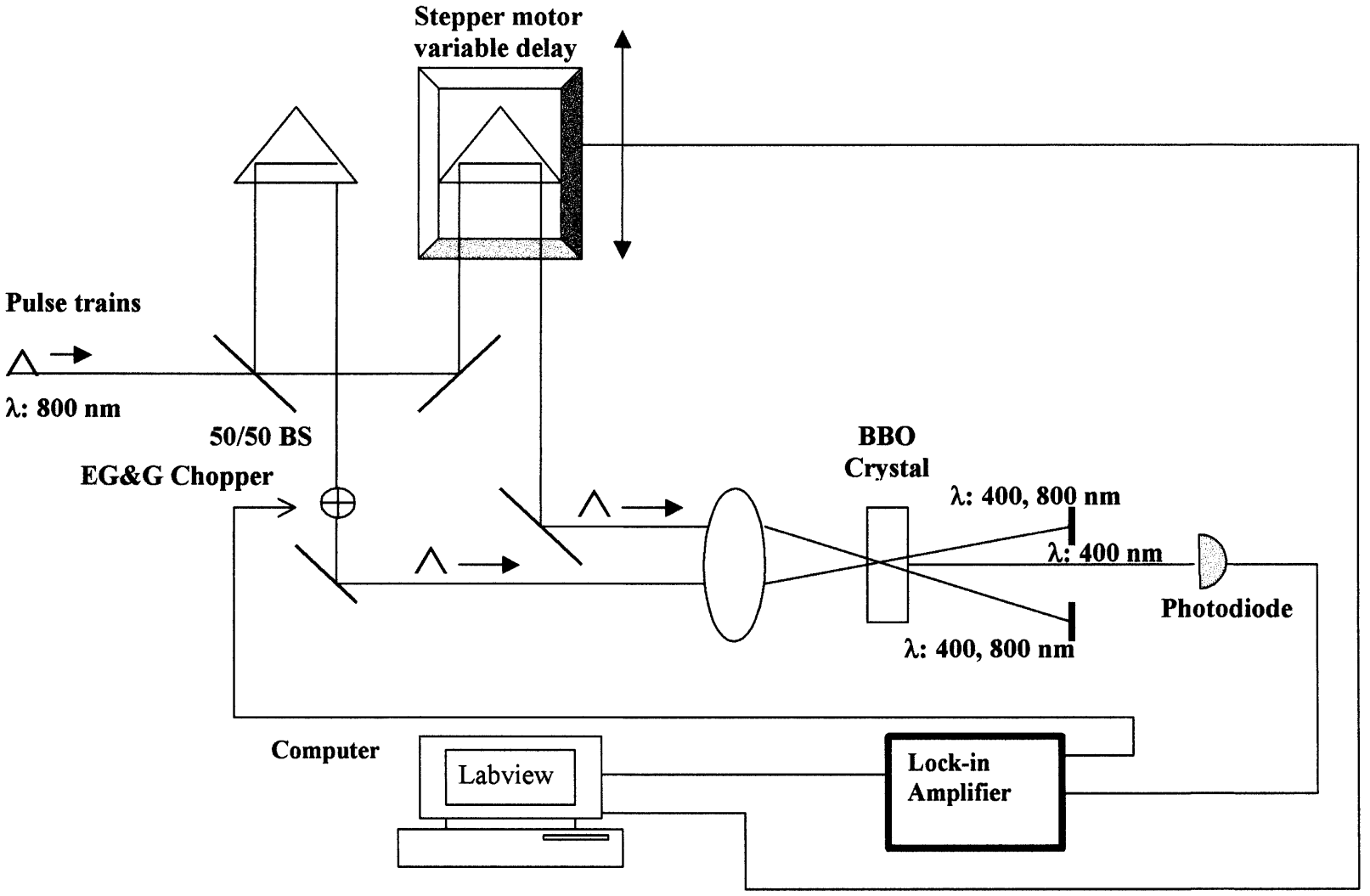

Figure2.4 Autocorrelation Experimental Setup

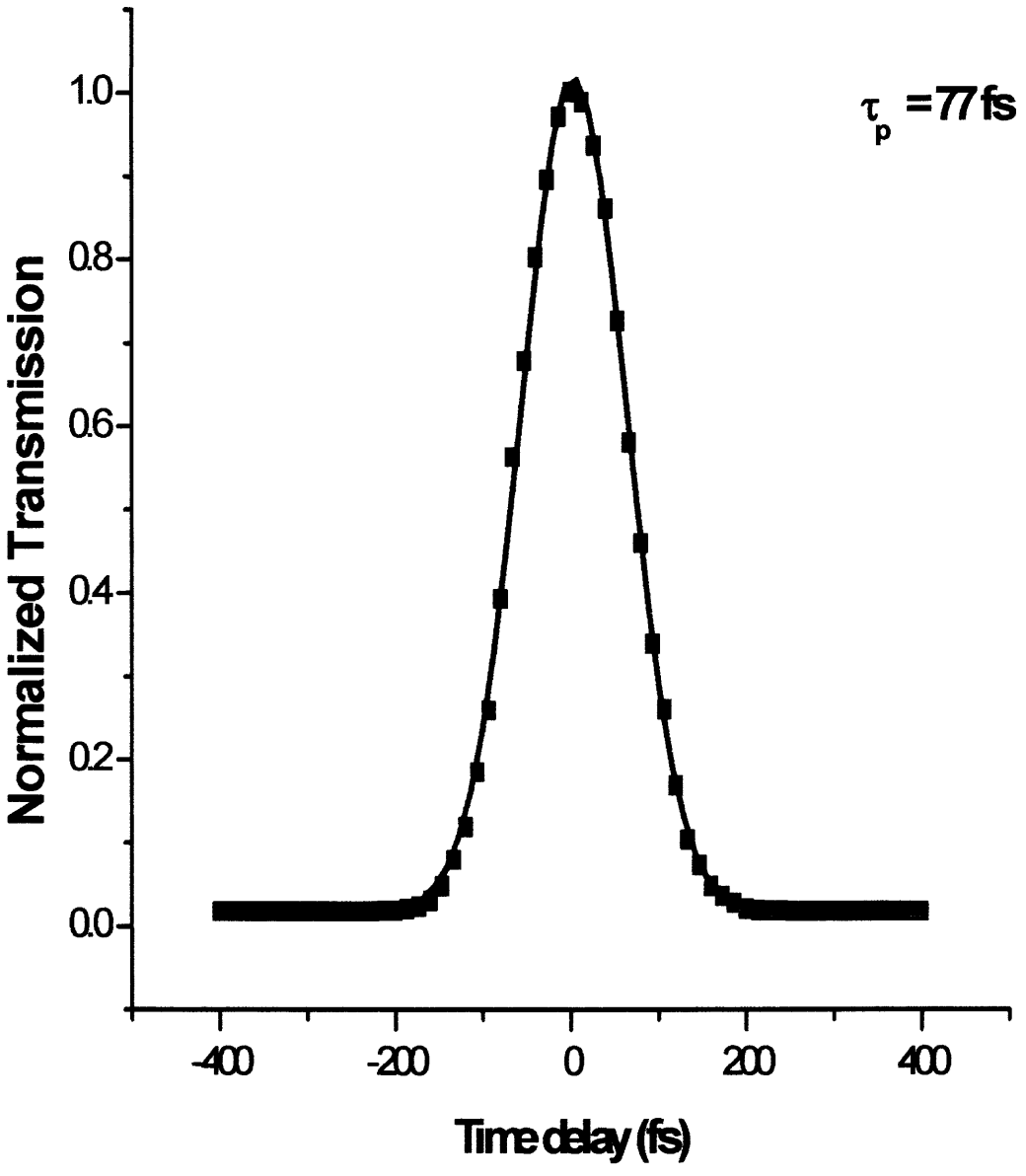

Figure. 2.5. Autocorrelation trace of Ti:sapphire laser at 800 nm. The experimental data are represented by squares and the solid line is a fit to the data.

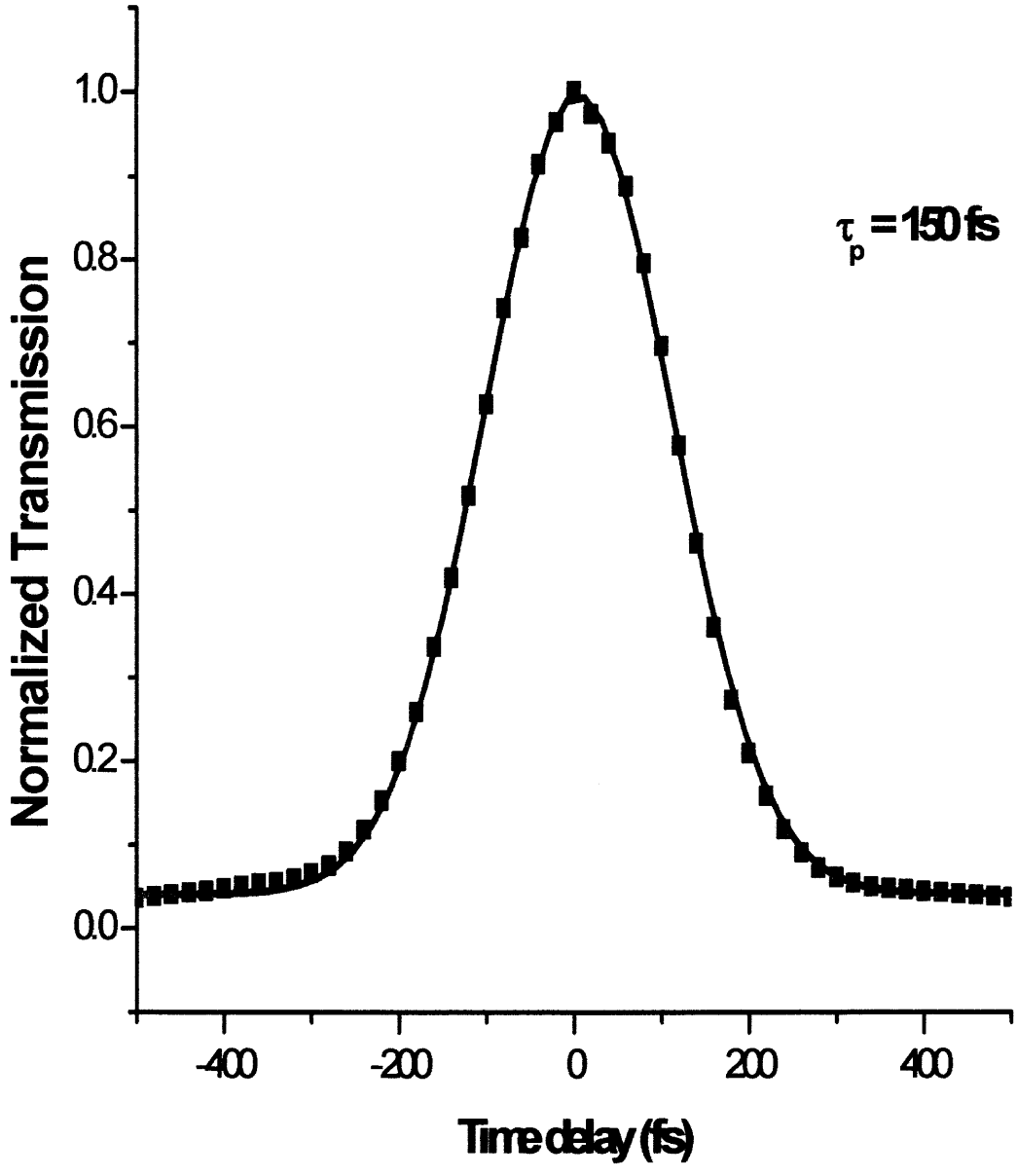

Figure. 2.6. Autocorrelation trace of Regenerative Amplifier Ti:sapphire Laser at 800 nm. Circles represent the experimental data and the solid line is a fit to the data.

2.4 Measurement of the Optical Spectrum

An Advantest 83381A optical spectrum analyzer (OSA) measures the optical spectrum of the femtosecond pulses generated by the respective lasers used in the various experiments. The OSA has a wavelength range of 0.35 to 1.75 μm. The OSA employs a Michelson interferometer, with a resolution of 0.1nm. It also included a built-in Helium-Neon laser that is used as the reference wavelength that produces a wavelength accuracy of ±0.1 nm at 1.3 μm. The add advantage of having a reference beam is that it ensures the long-term measurement stability even without wavelength calibration. The light from the laser is directed toward a fiber input with a core diameter of 200 μm whose output is connected to the unit and bandwidth of the laser is determined. The data from the unit can be extracted with the use of a computer using a program written by LABVIEW 5.1.

The spectrum of the Ti:sapphire laser operating at 805 nm is depicted in Fig. 2.7. The measured bandwidth is 9 nm. Diagnostic equipments such as a Tektronix TDS 210 oscilloscope with a bandwidth of 60 MHz combined with a REES E2000 laser spectrum analyzer are used for real time diagnostics, tuning and continuous monitoring of the spectral output of Ti:sapphire laser. Also an EOT ET-3000 InGaAs pin detector with a rise time of less than 200 ps in conjunction with a Tektronix 11801C digital sampling oscilloscope to monitor the contrast ratio of the pre-and post pulse to the switched pulse as well as monitor the amplified pulse train. The contrast ratio of the pre-pulse is 200:1 and post-pulse is 25:1

Table 2.1 Specification of Ti:sapphire laser systems.

Specification	Ti:sapphire laser (Tsunami)[11]	50kHz Regenerative (Spitfire) Amplifier Ti:sapphire laser[12]
Pulse duration	100 fs	< 130 fs
Wavelength	750-950 nm	750-850 nm
Power	< 2 W	600 mW
Pulse broadening	N/A	< 150 % of the input duration
Energy	20 nJ	10 μJ
Polarization	Linear, S	Linear, P
Pulse Shape	$Sech^2$	Gaussian
Repetition rate	82 MHz	50 kHz

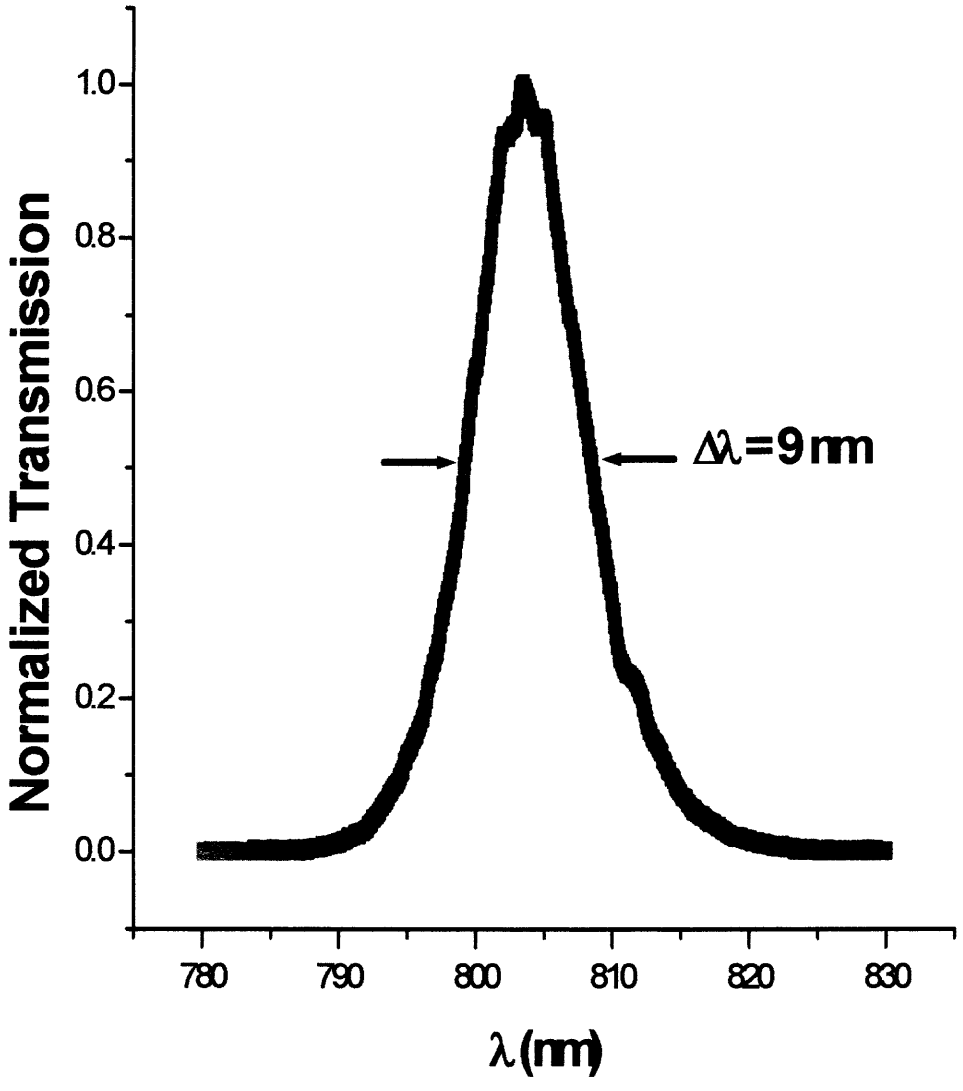

Figure 2.7. The spectrum of the Ti:sapphire laser

CHAPTER 3

NONLINEAR OPTICAL SUSCEPTIBILITY

3.1 Nonlinear Optics

Nonlinear optics refers of the interaction of an intense optical field with matter. The induced polarization of the medium due to the incident electromagnetic radiation is modified and therefore the electric field is also altered as it exits the medium. The advent of nonlinear optics began in 1960 with the creation of the first ruby laser and detection of second harmonics generation in quartz by Franken et al in 1961.[20] The various contributions to the optical nonlinear changes in the medium depend on the intensity of the light and the underlying crystal symmetry of the medium.

The nonlinear optical response occurs when certain materials are irradiated by an intense electromagnetic field. In the area of linear optics the induced macroscopic polarization (polarizability) of a medium irradiated by electromagnetic radiation is given by[21]

$$P(\omega) = \chi E(\omega) \tag{3.1}$$

where χ is the linear susceptibility of the material and $E(\omega)$ is the electric field at frequency ω.[21,22] The effects associated to the linear susceptibility, χ, are refractive index, absorption and dispersion. To derive the nonlinear optical properties of a given medium, the Boyd's nomenclature will be used.[21] At very large intensity, the polarization can be expanded with a Taylor expansion in terms of $E(\omega)$:

$$P(\omega) = \chi^{(1)}(\omega) : E(\omega) + \chi^{(2)}(\omega;\omega_1,\omega_2) : E(\omega_1)E(\omega_2) + \chi^{(3)}(\omega;\omega_1,\omega_2,\omega_3) : E(\omega_1)E(\omega_2)E(\omega_3) + \ldots \quad (3.2)$$

The first term, $\chi^{(1)}$, is the linear susceptibility. The second term, $\chi^{(2)}$ (second order nonlinear susceptibility) represents three waves interaction. It is the source for second harmonic generation, sum and difference frequency mixing. $\chi^{(2)}$ is a third rank tensor and contains 22 terms. For example, for a centrosymmetric system $\chi^{(2)}$ vanishes.$\chi^{(3)}$, the third order nonlinear susceptibility, involves a four wave interaction (three inputs and one output beam) and is source for such processes as third harmonic generation, self-phase modulation, cross phase modulation, self-focusing and stimulated Raman scattering. $\chi^{(3)}$ is a complex quantity where the real part is related to nonlinear refractive index and the imaginary part to nonlinear absorption. $\chi^{(3)}$ is a fourth rank tensor and contains 81 terms. The tensor indices will be suppressed for this chapter to facilitate an understanding of the nonlinear optical effects.

3.2 Dielectric Constant

The dielectric constant is a measure of the material's effectiveness as an electrical insulator or the amount of electrical energy stored in the medium when an electro-magnetic field is applied across it. In the linear regime, the dielectric constant, $\varepsilon(\omega)$, of a material is related to $\chi^{(1)}$ by[21]

$$\varepsilon(\omega) = 1 + 4\pi\chi^{(1)}(\omega) \quad (3.3)$$

In nanocomposite materials, the dielectric function is more complicated. The complication arises from the influence of the microstructured materials on the

macroscopic dielectric response. In this case, effective medium theory must be taken into account, where the effective dielectric function is a combination of, the host material, with dielectric function ε_h and the silicon nanocrystals (ε_i.).[23] For the purpose of the calculation of the refractive index, the dielectric function can be replaced by a uniform effective medium with a dielectric constant $\varepsilon_{eff.}$. In the next section the indices will be dropped with the understanding that the dielectric constant refers to the uniform medium, which include the response due to both the host and inclusion materials[23].

3.2.1 Refractive Index

The refractive index, n (ω), at low optical field is related to the linear dielectric, $\varepsilon(\omega)$, and susceptibility, $\chi^{(1)}$, by

$$n(\omega) = \sqrt{\varepsilon(\omega)} = \sqrt{1 + 4\pi\chi^{(1)}(\omega)} \tag{3.4}$$

At large optical fields, the refractive index is a function of the incident electromagnetic field at frequency (ω). The change in the refractive index can be expressed as[21]

$$n = n_o + 2\bar{n}_2 |E(\omega)|^2 = n_o + n_2 I \tag{3.5}$$

Where n_o denotes the weak field linear refractive index defined by equation (2.3) and $\bar{n}_2$ is the second order refractive index that describes the enhancement in the refractive index .as the intensity increases. The nonlinear index of refraction, n_2, is related to $\bar{n}_2$ by $n_2 = \frac{4\pi}{n_o c}\bar{n}_2$. This effect is used in optical switching and optical limiting devices. The third order susceptibility, $\chi^{(3)}$, is associated to the microscopic structure of the medium and can only be fully treated using quantum mechanical analysis. However, using a

simple model such as anharmonic oscillation gives an adequate description of the origin and the characteristic nature of the optical nonlinearity. Assuming an isotropic and centrosymmetric material, the induced nonlinear polarization that is generated by the propagation of a linearly polarized light beam at frequency ω through the medium is

$$P^{(3)}(\omega) = 3\chi^{(3)}(\omega = \omega + \omega - \omega)|E(\omega)|^2 E(\omega) \tag{3.6}$$

Therefore, the total polarization of the material is described as

$$P(\omega) = \chi^{(1)}E(\omega) + 3\chi^{(3)}|E(\omega)|^2 E(\omega) \tag{3.7}$$

An effective susceptibility can now be defined as $\chi_{eff} = \chi^{(1)} + 3\chi^{(3)}|E(\omega)|^2$. [21,22] To determine the relationship between the change in the refractive index and the nonlinear susceptibility we need to introduce the general expression for the refractive index, which is expressed as

$$n^2 = 1 + 4\pi\chi_{eff} \tag{3.8}$$

Substituting Eq. (2.4) on the left-hand side and the expression for χ_{eff} on the right-hand side of the above equation, then the expression becomes

$$\left(n_o + 2\bar{n}_2|E(\omega)|^2\right)^2 = 1 + 4\pi\chi^{(1)} + 12\pi\chi^{(3)}|E(\omega)|^2 \tag{3.9}$$

Ignoring any terms higher than $|E(\omega)|^2$, then the expression becomes

$$n_o^2 + 4\bar{n}_2|E(\omega)|^2 = 1 + 4\pi\chi^{(1)} + 12\pi\chi^{(3)}|E(\omega)|^2 \tag{3.10}$$

where the linear and nonlinear terms are related by

$$n_o = \left(1 + 4\pi\chi^{(1)}\right)^{\frac{1}{2}} \tag{3.10a}$$

and

$$\bar{n}_2 = \frac{3\pi\chi^{(3)}}{n_o} \tag{3.10b}$$

The alternate way of defining the nonlinear component of the intensity-dependent refractive index is to relate it to the intensity given below

$$2\bar{n}_2|E(\omega)|^2 = n_2 I \tag{3.11}$$

where I is the time-averaged intensity and is defined as $I = \frac{1}{\varepsilon_o}|E(\omega)|^2$. Therefore n_2 is proportional to $\bar{n}_2$ by $n_2 = \frac{4\pi}{n_o c}\bar{n}_2$. Thus n_2 is defined as the nonlinear refractive index and in SI units is related to real part $\chi^{(3)}$

$$n_2 = \frac{12\pi^2\chi^{(3)}_{\mathrm{Re}}}{n_o^2} \tag{3.12}$$

Usually one experimentally measures the nonlinear refractive index and relates it back to $\chi^{(3)}_{\mathrm{Re}}$. There are several methods to determine n_2 such as Z-scan and degenerate four waves mixing (DFWM), which will be described in the following chapters.

3.3 Mechanisms for Nonlinear Effects

If the size of the crystal is smaller than the optical wavelength, then its physical properties, i.e electronic structure are modified in many ways. The most significant changes occur as the fraction of atoms at the surface becomes larger, the arrangement of the nuclei changes in order to relax the energy of the system as a whole, i.e., a transition from crystalline to molecular (cluster) behavior takes place. This effect arises as the

crossover to the bulk structure takes place if the number of atoms is ~10^3. . The critical cluster size for crystalline behavior can be much smaller because of the saturation of surface bonds by host atoms when the particles are embedded in a host material. [23].

The purpose of these experiments described in the next chapters is to understand the underlying physics that give rise to the nonlinearity. Currently, two models, the local field and defects models, are used to explain the large nonlinear characteristics of nanoclusters.

The basis for the enhancement in the nonlinear absorption and refraction in bulk semiconductors are the creation of electron-hole pairs by interband optical absorption, which subsequently, modifies the absorption spectrum. As the electron-hole pairs completely fill up the states in the conduction band it prevents further absorption into the occupied states by Pauli exclusion. This produces saturation in the absorption. It also impacts the nature of the electronic states because of coulomb or exchange interactions where both of these interactions greatly influence the exciton absorption spectrum.

In the case of quantum dots, it's argued that only state filing is the major mechanism for absorption saturation of the lowest transition as in two level systems, one for each spin. The absorption saturation is defined as[24]

$$\varepsilon = \frac{\varepsilon_\infty + \beta(\delta + i)}{1 + \delta^2 + \frac{I}{I_s}} \tag{3.13}$$

where I is the intensity and I_s, the saturation intensity, as $I_s = \hbar/(\beta\tau V)$,$\tau$ is the recombination time and is dependent on the medium[24]. When the polarization is such that the transitions are allowed for both spins, complete saturation of the absorption will occur when there is one excited electron-hole pair per quantum dots. The changes in absorption

and in the index of refraction can be much larger because of its volume before the transition saturates.

Previous studies on surface-oxidized silicon nanocrystals concluded that these materials fundamentally behaves as indirect bandgap materials with low oscillator strength although they yield high luminescent at 630 nm. (Wilson., Science) The purpose of these experiments carried out within the next chapters is to understand the underlying physics that give rise to the nonlinearity. Currently, two models, the local field and defects models, are used to explain the large nonlinear optical characteristics of nanoclusters

3.3.1 Local Field Model

In nanostructured materials embedded in the dielectric, their effect may be described qualitatively by a quasi-static theory.[26] Local fields due to dielectric confinement will strongly affect the optical properties. The internal electric field within the particle is smaller relative to the external field in the surrounding medium. The internal field can strongly generate major changes in the optical response .The total electric field is therefore composed of two components: the external field E_0 and the internal field, E_i...For geometrical shape such as spheres, the field inside the particle is uniform and proportional to the surrounding field. The effective dielectric constant, ε_{eff}, and the electrical polarizability,α_e, of each individual cluster, can be written as[27]

$$\varepsilon_{eff} = \varepsilon_d \left[1 + N\alpha_e / (1 - \alpha_e C) \right] \tag{3.14}$$

where ε_e is the permittivity of the dielectric matrix and N is the density of the electrical dipoles formed by the clusters. The coupling constant, C, couples the internal field. E_i, to the polarization, P, by $E_i = CP/\varepsilon_d$. The permeability, μ_{eff}, can also be expressed as

$$\mu_{eff} = \mu_d \left[1 + N\alpha_m / (1 - \alpha_m C) \right] \tag{3.15}$$

where α_m is the magnetic polarizability. In the case of spherical clusters, the polarizability is proportional to their radius cubed. Macroscopically, the strength of an electric dipole is related to the amount of charge separation while the magnetic dipole is proportional to the current loop's area and both parameters are related to the electronic mean free-path.

Non-linear effects may be explained and included into this simple model by appropriately modifying the polarizability constants. Here we expand the polarizability of the cluster by a series.

$$P = \alpha_e E + \beta_e EE + \gamma_e |E|^2 E \tag{3.16}$$

And the effective permittivity for symmetrical and isotropic clusters, to the first order in P. is

$$\varepsilon_{eff} = \varepsilon_d \left[1 + N\alpha_e + \frac{N\gamma_e |E_0|^2}{\left(1 - \left(\alpha_e - 3\gamma_e |E_o|^2\right) C\right)^4} \right] \tag{3.17}$$

In this case it is evident that the effective dielectric constant is modified by the intensity through the coupling factor, which is proportional to the square of the amplitude of electric field.

CHAPTER 4

Z-SCAN TECHNIQUE

4.1 Z-SCAN

The Z-scan technique is a relatively simple and direct method to characterize both the nonlinear refraction and nonlinear absorption.[28] The Z-scan technique is a single axis beam distortion measurement, which makes use of self-focusing. At high intensity levels, self-focusing transpires because the index of refraction of a medium is modified by the presence of the beam itself. The refractive index at high intensity is given by

$$n = n_o + n_2 I(r,t) \tag{4.1}$$

where n_2 (the nonlinear refractive index coefficient) is proportional to real part of χ^3 . Through the intensity dependent refractive index, the material acts as a nonlinear lens. The absorption of the material is also intensity dependent given by

$$\alpha = \alpha_o + \beta I(r,t) \tag{4.2}$$

where the nonlinear absorption coefficient (β) is related to the imaginary part of χ^3. The maximum index change $(\Delta n = n_2 I)$ will occur at the largest intensity because the Δn is a function of intensity. This means that Δn is at its highest at the beam center for a Gaussian beam and decreases to zero at the wings of the beam, which causes the wave fronts of the beam to bend. The phase fronts will become concave when $n_2 > 0$ about z and focus the beam. Furthermore, if $n_2 < 0$, the wave phase front will become convex about z and this will cause the beam to defocus. Therefore the nonlinear material

behaves as thin lenses provided that the thickness of the material, L, is less than the Raleigh range (diffraction length of the beam) where $z_o = \frac{\pi\omega_o^2}{\lambda}$, ω_o is the radius of the beam at the focal point, and λ is the wavelength of the beam. Therefore, the focal length of the nonlinear medium is related to the change in the refractive index by[29]

$$f^{-1} = L\frac{\partial^2 \Delta n}{\partial^2 r^2}\Big|r = 0 \cdot \tag{4.3}$$

For a Gaussian beam the equation become

$$f = \frac{r_o^2 c\varepsilon_0 n_0}{n_2 I_o L} \tag{4.3.1}$$

The Z-scan technique allows us to measure the modification of a focused gaussian beam through a nonlinear medium as the medium is moved about the focal point.[28] Because of the intensity dependent refractive index, one is able to measure the distortion of the beam, in the farfield through an apertured detector, as the nonlinear medium further focuses or defocuses the beam. From the Z-scan measurement, one can derive the value for both the real and imaginary part of $\chi^{(3)}$.[28]

4.2 The Calculation of Nonlinear Components

In the Z-scan experiments, TEM_{oo} Gaussian beam is assumed with a waist of ω_o propagation in +z direction. The optical electric field is expressed as

$$\vec{E}(z,r,t) = E_o(t)\frac{w_o}{w(z)}e^{\left(-\frac{r^2}{w^2(z)}-\frac{ikr^2}{2R(z)}\right)}e^{-i\Phi(z,t)} \tag{4.4}$$

where $\omega^2(z) = \omega_o^2(1+\frac{z^2}{z_o^2})$ is the beam radius and $R(z) = z(1+\frac{z_o^2}{z^2})$ is the radius of wavefront curvature and $k = \frac{2\pi}{\lambda}$ is the wave vector. E_o represents the electric field at the focus and contains the temporal envelope of the laser pulse. For a thin material, the amplitude and nonlinear phase change, $\Delta\phi$, of electric field are now given by

$$\frac{d\Delta\phi}{dz} = k\Delta n(I) \tag{4.5}$$

$$\frac{dI}{dz} = -\alpha(I)I \tag{4.6}$$

where I and α are the intensity and linear absorption coefficient.[28] Solving the equations give $\Delta\phi$, the phase shift at the exit surface of the medium, which arises from the radial variation of the incident intensity at a given location within the sample and is defined as

$$\Delta\phi(r,z,t) = \frac{\Delta\Phi_o(t)}{1+z^2/z_o^2}\exp\left[-\frac{2r^2}{w^2(z)}\right] \tag{4.7}$$

with $\Delta\Phi(t)$, the on-axis phase shift at the focus, given by

$$\Delta\Phi(t) = \frac{2\pi}{\lambda}\Delta n_o(t)L_{eff} \tag{4.8}$$

$$L_{eff} = \frac{1-e^{-\alpha L}}{\alpha} \tag{4.9}$$

and $\Delta n_o(t)$ is the instantaneous on axis index change at the focus and is given by $\Delta n_o(t) = \gamma I_o(t)$. I_o is defined as the on-axis intensity at the focus (z=0) and γ is the nonlinear refraction in unit of cm^2/W.. It is related to the instantaneous input (peak) power within the sample by this relationship, $P_i(t) = \pi\omega_o I_o(t)/2$. The $\vec{E}$ at the exit surface of the sample, z_1, which include the nonlinear phase variation is now given by

$$\vec{E}'(r,z,t) = \vec{E}(r,z_1,t)e^{(-\frac{\alpha L}{2})}e^{[i\Delta\varphi(r,z_1,t)]} \tag{4.10}$$

Using a numerical Gaussian decomposition method derived by Weaire et al.[30] and determining the pattern of the beam in the far field one is able to calculate the Z-scan power transmittance given by

$$T(z,t) = \frac{\int_0^{r_a} |E_a(\Delta\phi_o,r,z,t|^2 rdr}{S\int_0^{\infty} |E_a(0,r,z,t)|^2 rdr} \tag{4.11}$$

where r_a is the aperture radius and S is the aperture transmittance in the linear regime. To determine the nonlinear absorption, β, the aperture is removed and the transmittance is no longer sensitive to the beam distortion and Z-scan data is a function of nonlinear absorption. The total transmittance is given by

$$T(z,S=1) = \sum_{m=0}^{\infty} \frac{\left[\frac{\beta I_o L_{eff}}{1+z^2/z_o^2}\right]^m}{(m+1)^{3/2}} \tag{4.12}$$

The first two terms in the summation is generally sufficient to determine β. By fitting the open aperture data (Fig. 4.1) to the above equation one derives the value for β. The

nonlinear absorption coefficient β is related to imaginary part of χ^3 by $\chi^3_{\mathrm{Im}} = \frac{n_o^3 \varepsilon_0 c^2}{w}\beta$.,

where w is the optical frequency.

The nonlinear refraction is estimated by measuring the farfield output with an apertured detector. The expression for the closed aperture Z-scan transmittance, which is sensitive to the on axis phase distortion, is written as

$$T(z,\Delta\Phi_o) = 1 - \frac{4\Delta\Phi_o \frac{z}{z_o}}{\left[\left(\frac{z}{z_o}\right)^2 + 9\right]\left[\left(\frac{z}{z_o}\right)^2 + 1\right]} \tag{4.13}$$

For a sample that exhibits both nonlinear absorption and refraction, their contribution to the farfield beam profile and Z-scan transmittance are coupled. However, it is simple to eliminate the nonlinear absorption contribution to the closed apertured data. To determine the correct value for $\Delta\Phi(t)$, the normalized closed aperture Z-scan data should be divided by the open Z-scan data to retrieve n_2. The Z-scan gives the value for $\Delta\Phi(t)$ directly and substitution in the equation for nonlinear refractive index ($\gamma = \frac{\Delta\Phi_o}{I_o L_{eff}}$), gives the value for χ^3_{Re} ($\chi^3_{\mathrm{Re}} = 2n_o^3 \varepsilon_o c\gamma$). γ is related to n_2 by $n_2(esu) = \frac{cn_0}{40\pi}\gamma\left(\frac{cm^2}{W}\right)$[29]. A computer generated trace for the closed-apeture Z-scan is shown in Fig. 4.2

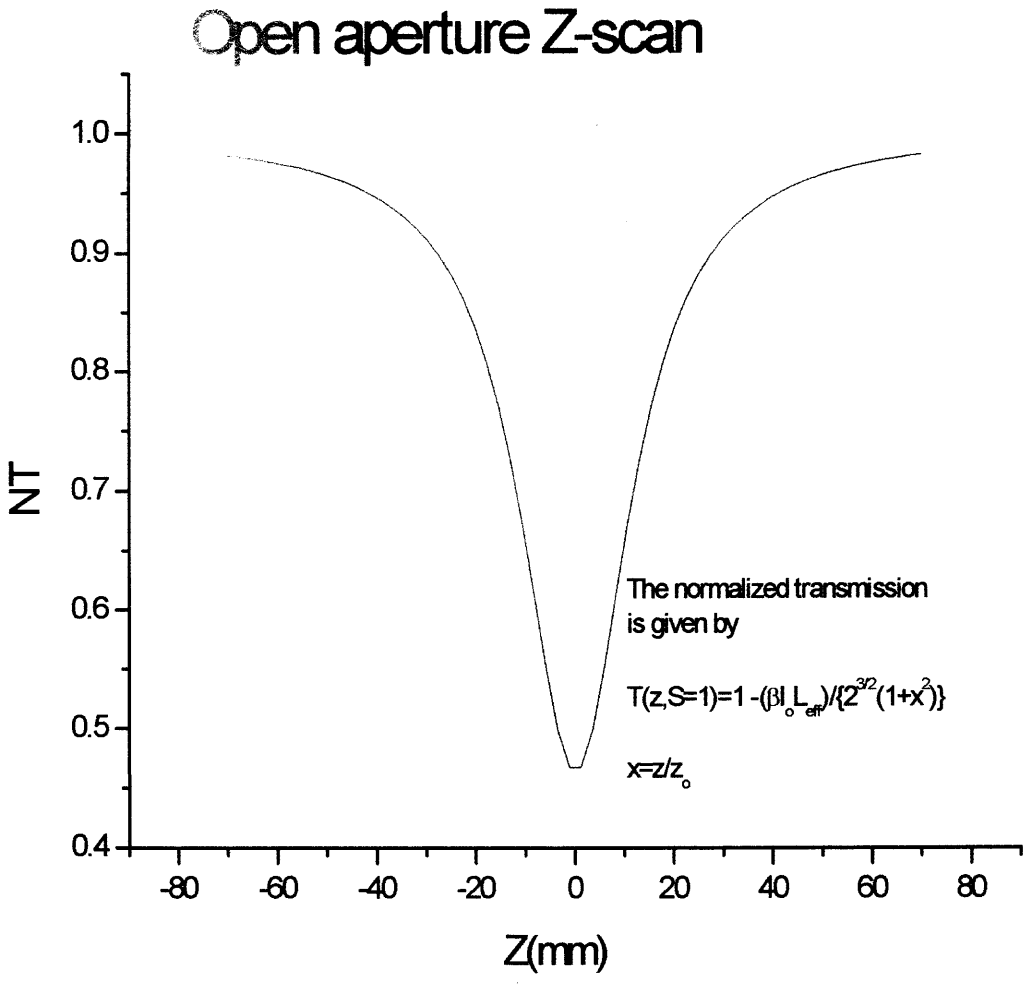

Figure 4.1 Simulated open aperture Z-scan

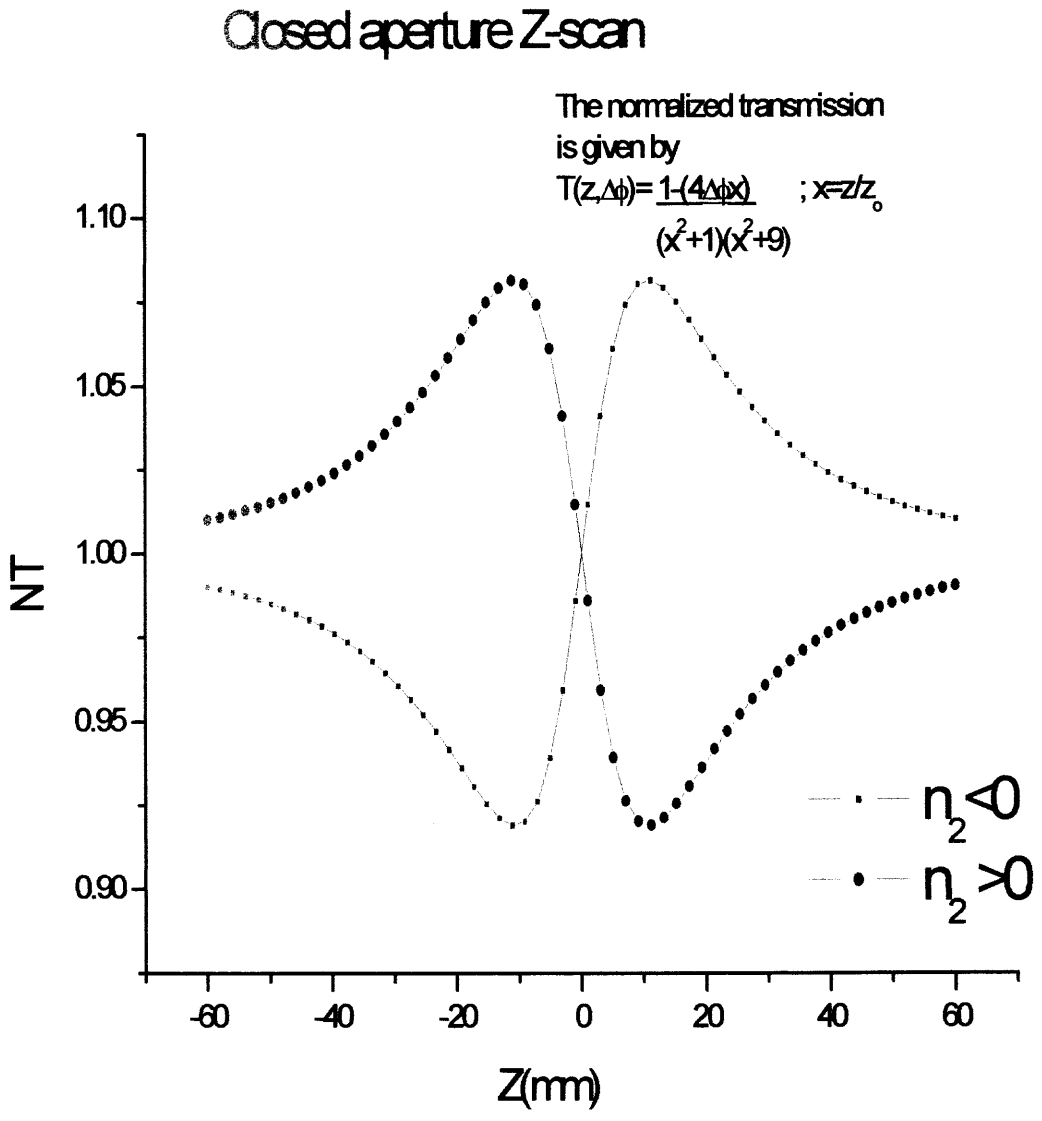

Figure 4.2 Simulated closed aperture Z-scan

4.3 Experimental Setup

In the experimental setup (Fig.4.3), a stepper motor stage is used to move the sample about the focus of a lens and transmission is detected as a function of distance from the focal point. Ultrashort pulses are either the Ti:sapphire laser or the regenerative Ti:sapphire amplifier laser are utilized. These pulses are also frequency doubled in a 1mm BBO crystal. Additionally, 70 ps pulses at 532 nm are derived from frequency doubled modelocked and Q-switch Nd:YAG laser, switched out of a 36 kHz q-switched train by a Pockels cell. The beam is mechanically chopped and its signal is used as the reference signal for the lock-in amplifier. For the open aperture Z-scan scheme, the entire beam is measured. The detection scheme involves the use of a silicon photodetector and an analog EG&G 5209 or digital EG&G 5270 lock-in amplifier. For the closed aperture experiment, a 1 or 2mm aperture is positioned in front of the detector at a minimum of 2 focal lengths away from the lens focus. A lens of 15 cm is typically used. The data is collected using a Labview 4.1 software package, which also controls the stepper motor and the lock-in amplifier. The experimental data is analyzed with fitting routines written in Mathematica 4.1 and MathLab 6.

4.3.1 Calibration

CS_2 is used to calibrate and measure the spot size of the beam in the experimental Z-scan setup. CS_2 is a well-known and extensively studied liquid whose nonlinear refractive index is 1.3×10^{-11} esu (3.9×10^{-14} m^2/W)[28]. Using a calibrated 0.1mm cell, 15 cm lens and n_2 (CS_2) as a fixed parameter in the fitting routine, the spot size, ω_o, at the focus can be determined. In Figure 4.4, an experimental closed-aperture z-scan trace CS_2 is

illustrated. The output from the regenerative amplifier Ti:sapphire(λ=800nm, τ_p= 138 fs) is used to investigate the nonlinearity of the material.. The average power is 900 μW taking into account 10% loss due to reflection from the front surface. The calculated intensity at the focus, I_o, is estimated $6.7x10^8 \frac{W}{cm^2}$. From the fitting routine, the experimental data resulted in a value of 0.0204 for the nonlinear phase shift and a spot size of 21.8 μm. This correspond to a value for n_2 $1.48x10^{-11} esu$ or $3.89x10^{-14} cm^2/W$. The percentage error from published results for CS_2 is 13%. This is confirmation that Z-scan experimental setup is calibrated.

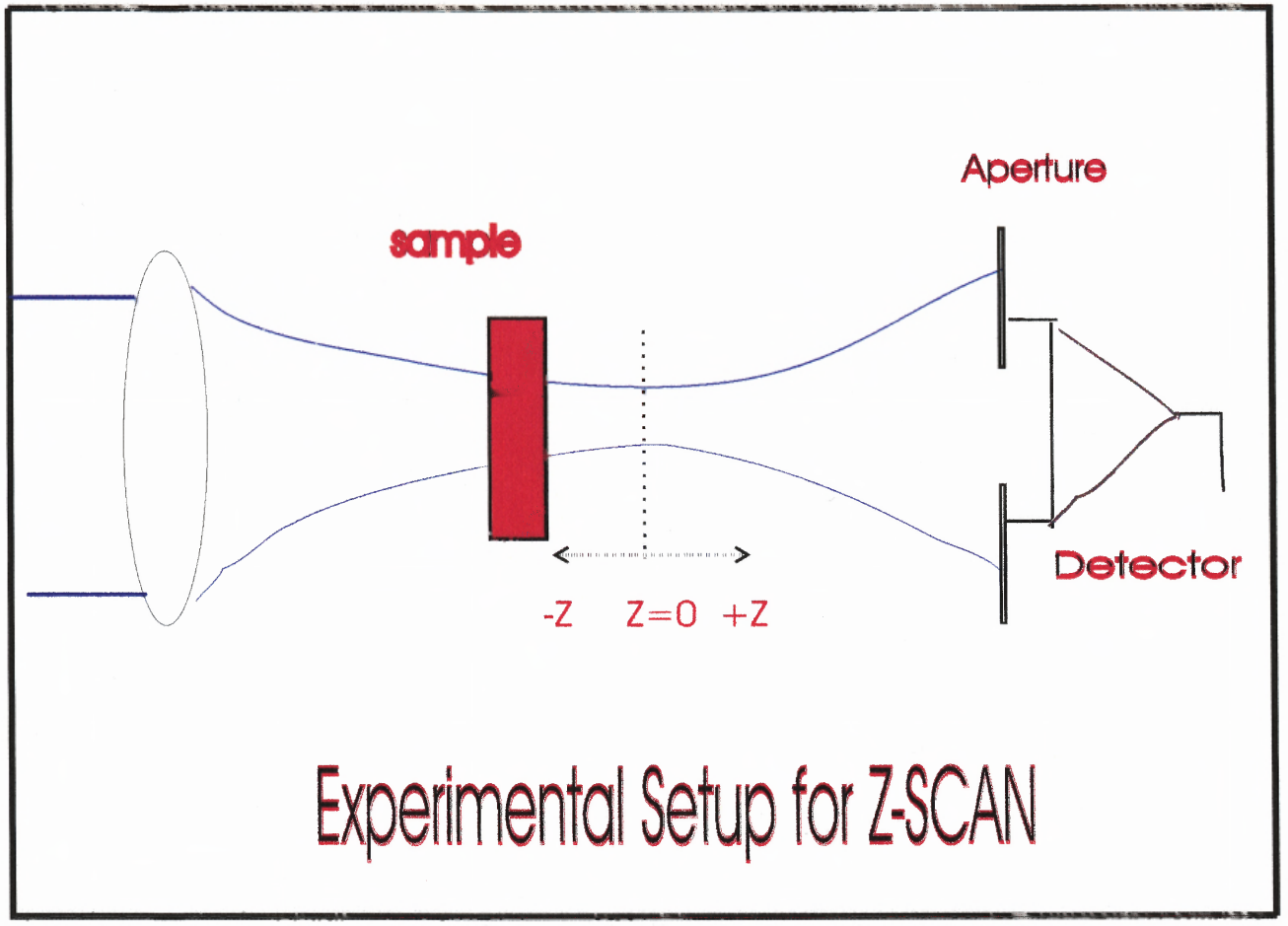

Figure 4.3a Z-scan setup

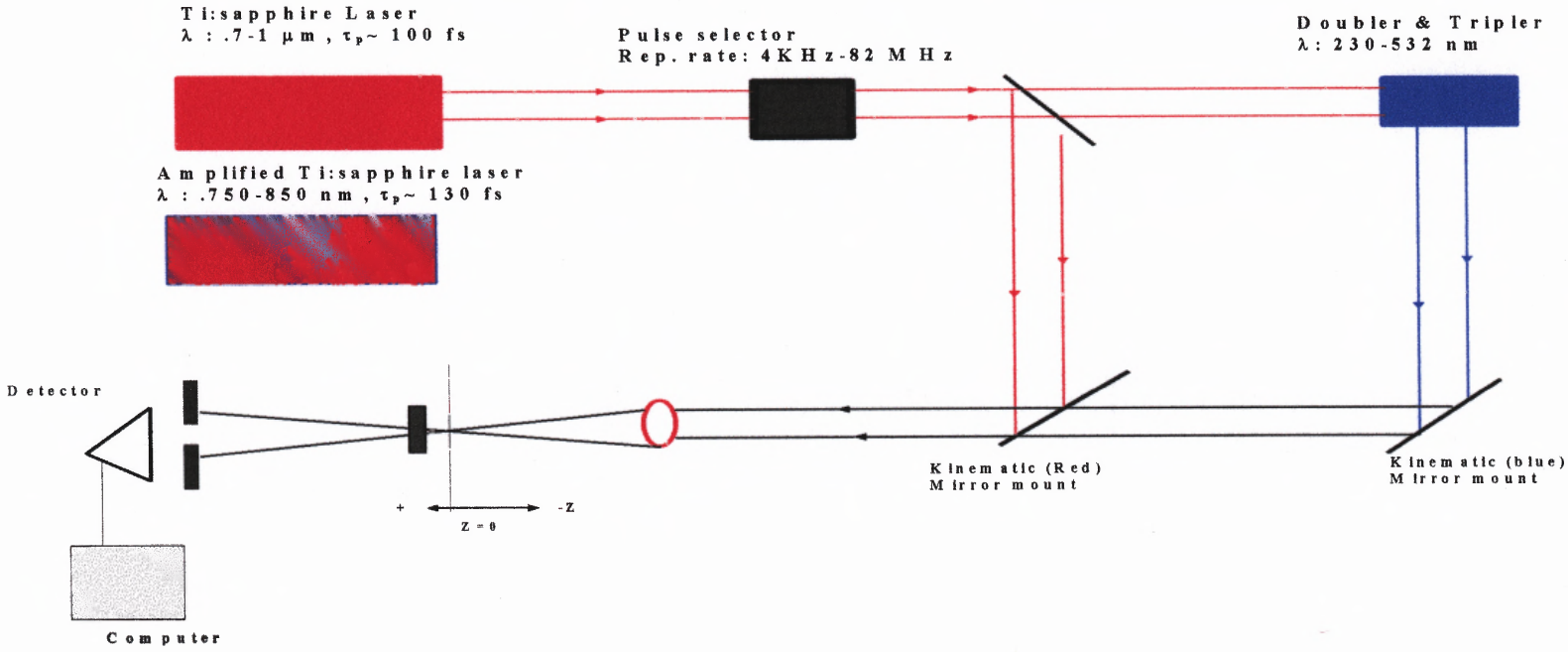

Figure.4.3b Experimental setup for the Z-scan measurement

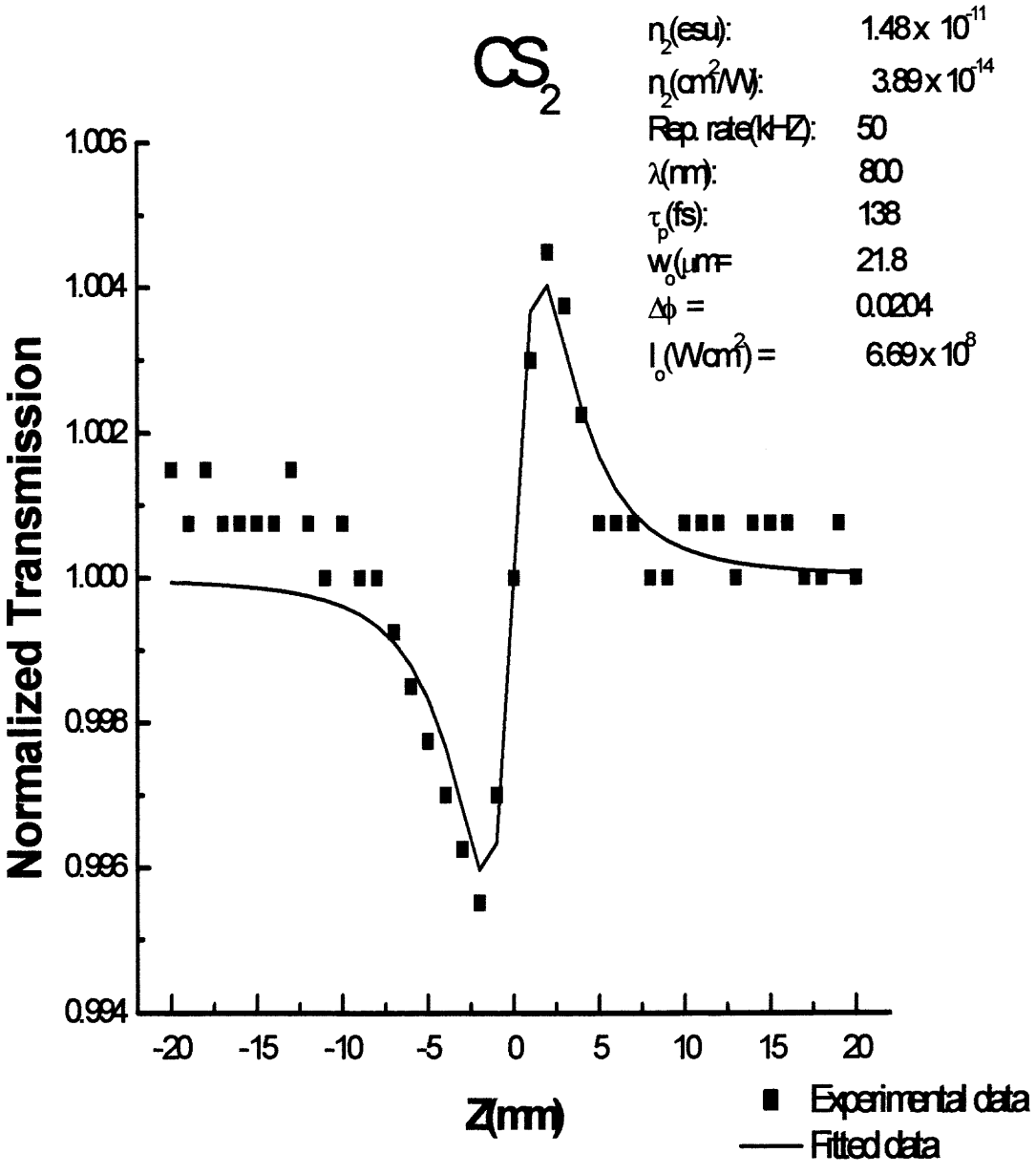

Figure 4.4 closed aperture Z-scan for CS_2

4.4 Experimental Result

Initial experiments were done at 790 nm from the Ti:sapphire oscillator at 90 fs. The intensity was $2.9x10^{8}\,W/cm^{2}$. The linear absorption, α, was $1.4/\mu m$. For the laser ablated Si sample β was estimated at $1.4x10^{-4}\,cm/W$ with a spot size of 30 μm (Fig4.5). For the close aperture data, which was divided by the open aperture data, a value of – 0.8346 was obtained for the phase shift which gives a value $\gamma = -2.1x10^{-9}\,cm^{2}/W$ ($\chi^{3}_{\mathrm{Re}} = -1.2x10^{-7}\,esu$)as shown in Figure 4.6.

For the ion-implanted Si sample, the same measurements were performed. We were able to measure nonlinear absorption ($\beta = 7.9x10^{-4}\,cm/W$) however; we were unable to extract any meaningful information about the nonlinear refraction from the closed Z-scan data even after dividing by the open Z-scan data (Fig. 4.7, 4.8). We attributed this to the large nonlinear absorption due to the ion implantation damage.

The materials were also studied at 375 nm. Using a Spectra Physics tripler, the fundamental output of the Ti:sapphire laser can be frequency doubled and then that light can be mixed with the fundamental to produce a frequency tripled output. Here we used the frequency-doubled output at 375nm at an estimated pulsewidth of 70 fs. The linear absorption (α) is $4/\mu m$ for the laser ablated Si and $1.2/\mu m$ for the ion-implanted Si .The value obtained nonlinear index of refraction for the laser-ablated sample is $\gamma = -1.6x10^{-9}\,cm^{2}/W$ and $\chi^{3}_{\mathrm{Re}} = 9.2x10^{-8}\,esu$ for $I_o = 8x10^{7}\,W/cm^{2}$. For the nonlinear absorption we estimated $\beta = 1.6x10^{-3}\,cm/W$ (fig.4.9b). For the ion-implanted sample

were unable to extract any information for the change in the index of refraction consistent with the 800 nm data but we were able to fit the open aperture data for.

Z-scan experiments were performed at 800 nm with the amplified pulses with a pulsewidth 138 fs. The intensity was 1.58 x 10^7 W/cm^2. The estimated value for the nonlinear index of refraction, γ, is 1.08 x 10^{-8} cm^2/W ($\chi^3_{Re} = 6.15x10^{-7} esu$) (Fig.4.10). A value of ($\beta = 1.4x10^{-4}\, cm/W$) was obtained from the fitting routine for the nonlinear absorption fig 4.11). Si NC's made by ion implantation were studied to take advantage of the fact that the size distribution of nano-particles can be controlled in a uniform manner. However, we found that the nonlinearity of the ion-implanted sample was dominated by nonlinear absorption attributed to 2-photon absorption ($\beta = 6.1x10^{-4} cm/W$) and we were unable to extract information for $\chi^{(3)}_{Re}$

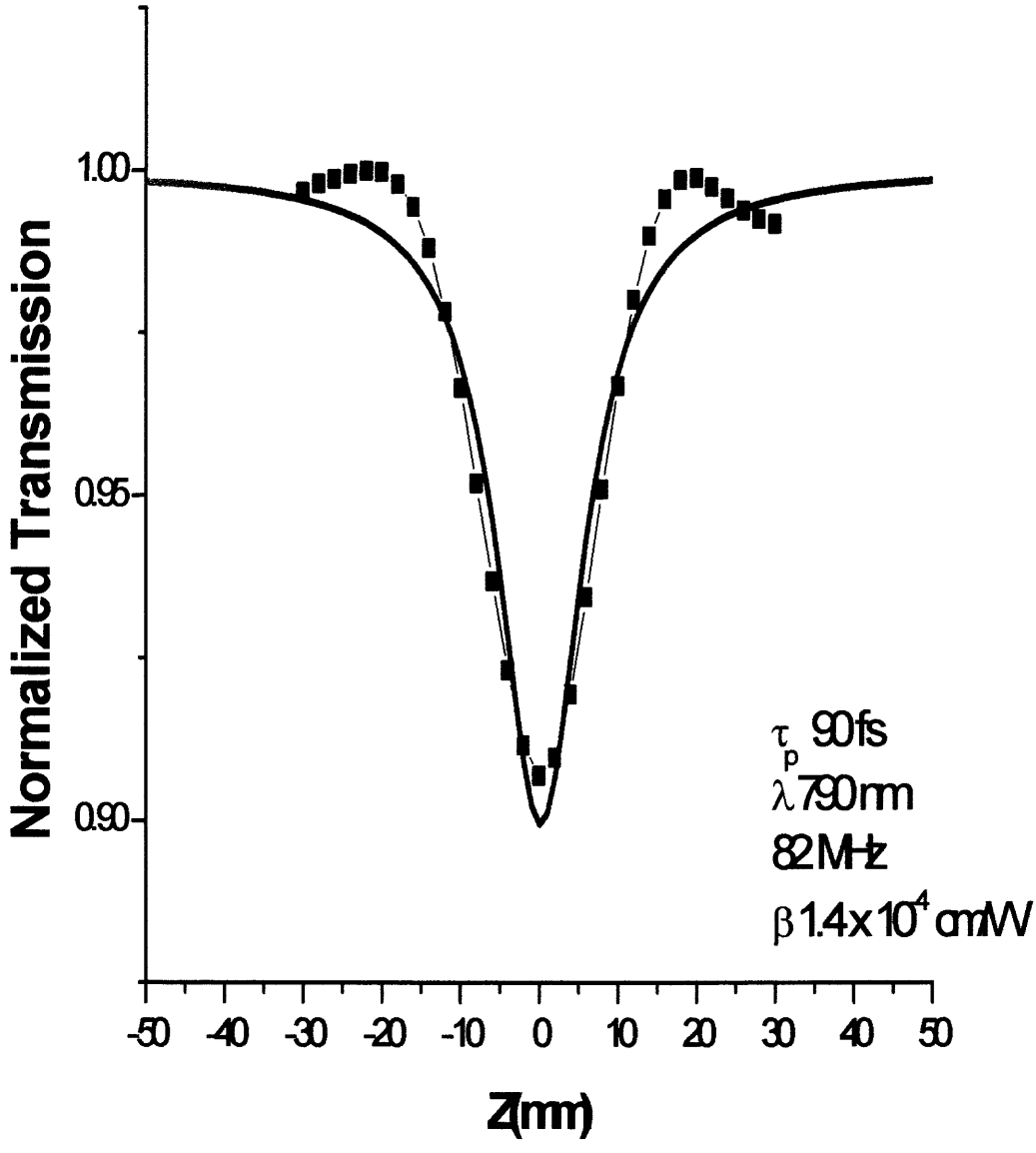

Figure. 4.5 Open Z-scan @790 nm, 82 MHz for laser ablated Si

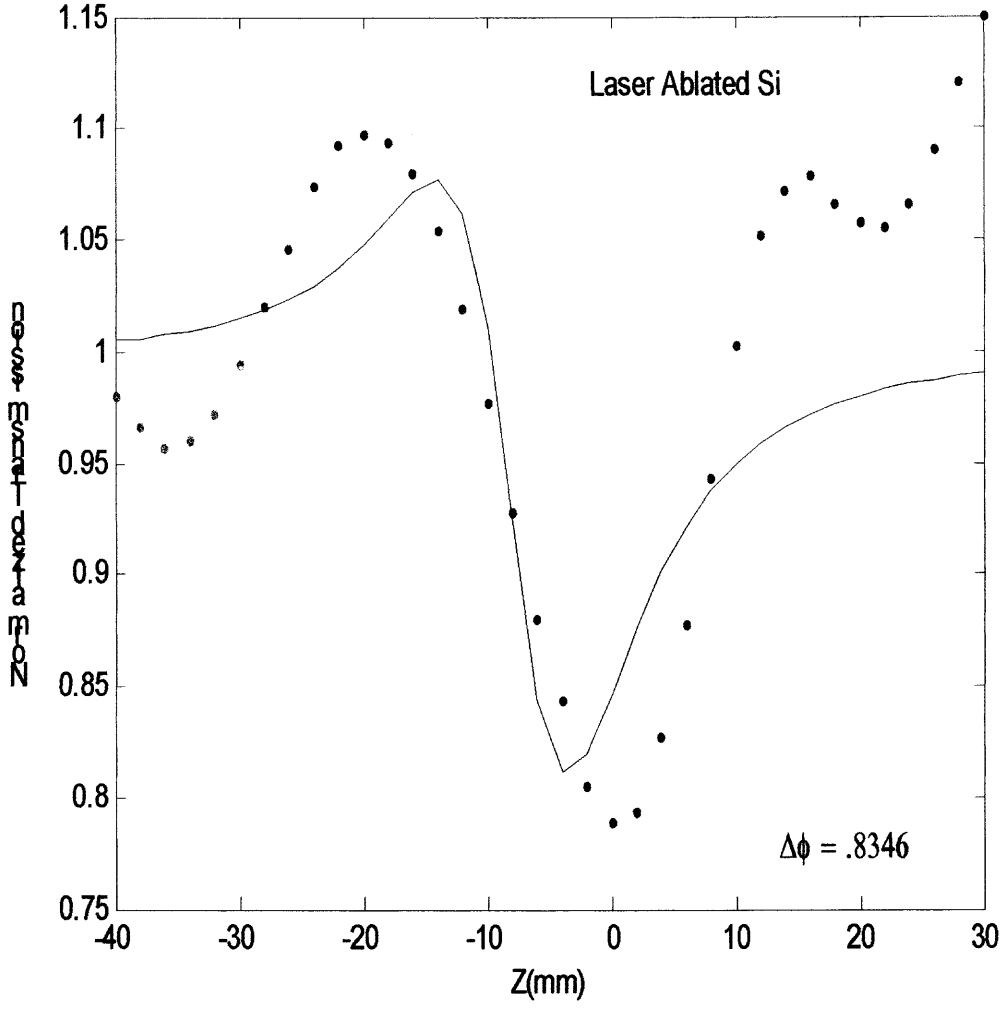

Figure 4.6 closed-apertured Z-scan @ 790 nm, 82 MHz, laser ablated Si

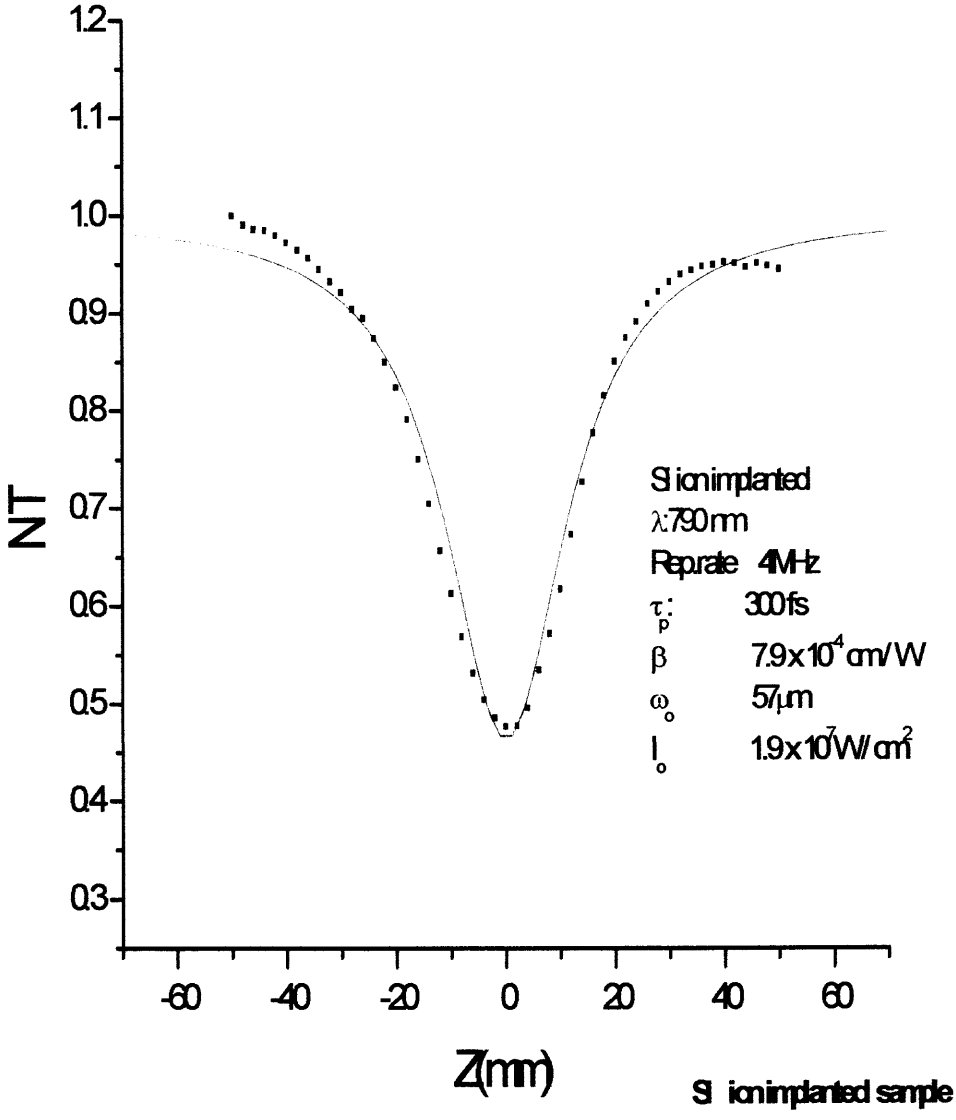

Figure. 4.7 Open Z-scan @790 nm, 4 MHz for ion-implanted Si NC's

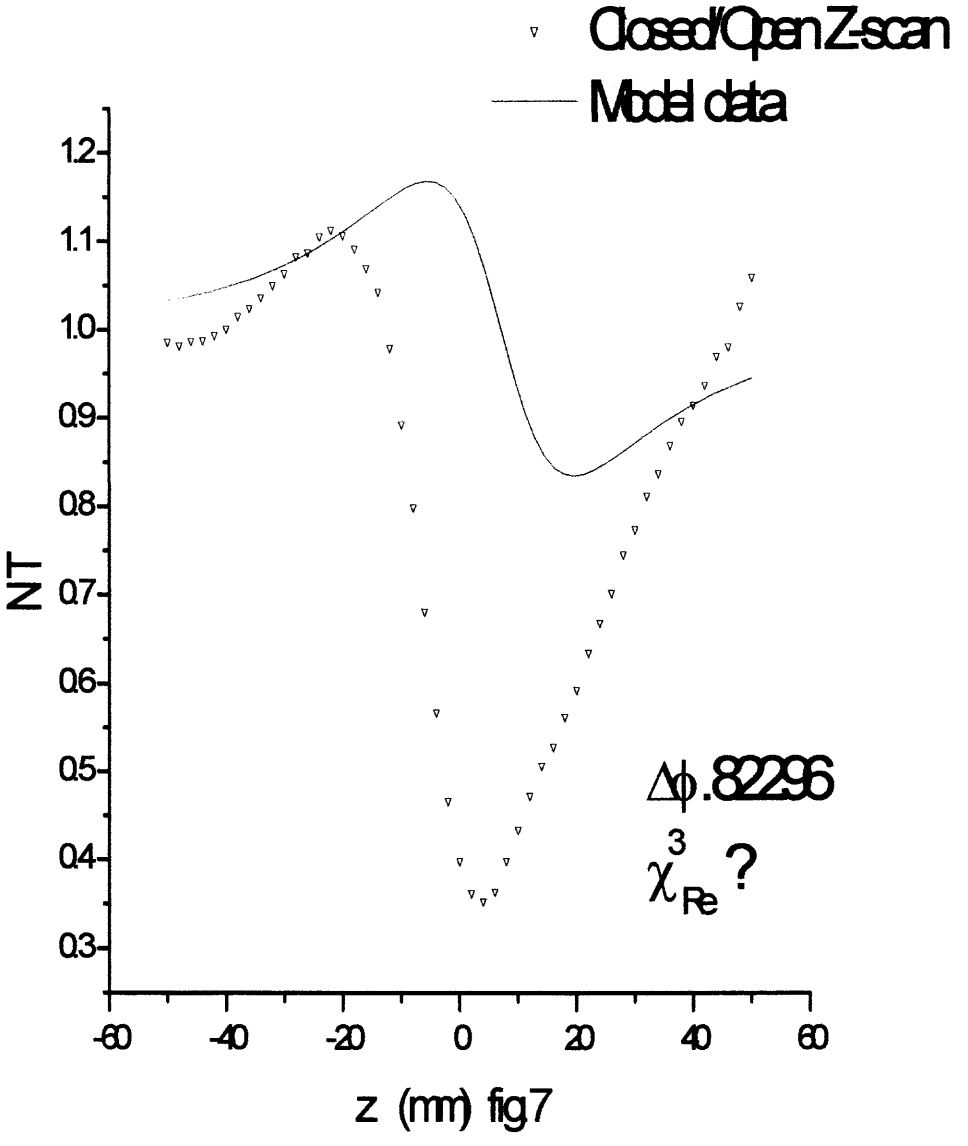

Figure. 4.8 Ion-implanted Si NC's Closed Z-scan @790 nm, at 4 MHz using a Spectra acoustic pulse picker

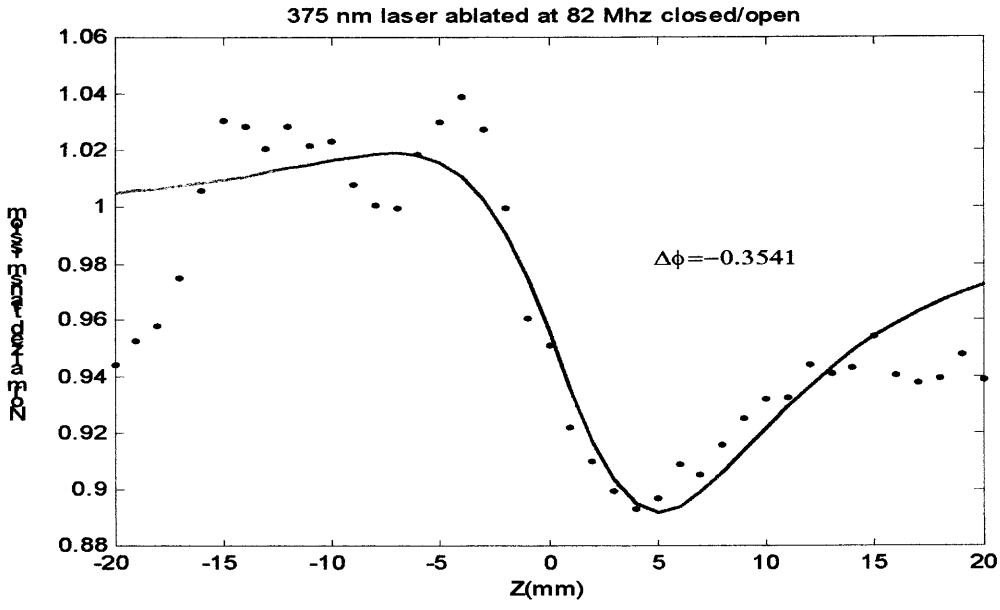

Figure. 4.9a Closed Z-scan @375 nm, 82 MHz for laser ablated Silicon

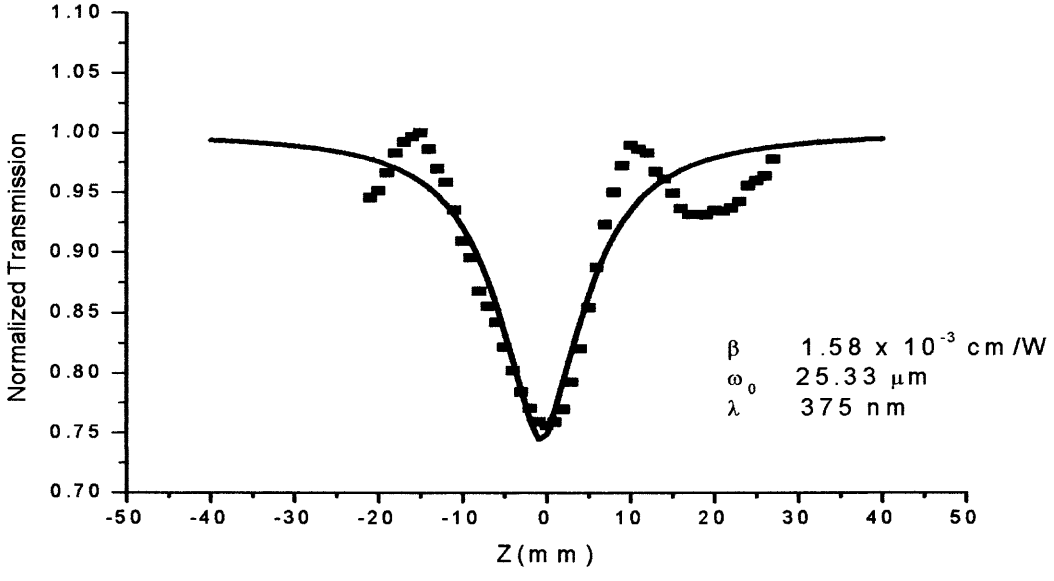

Figure. 4.9b Open Z-scan @375 nm, 82 MHz for laser ablated Silicon

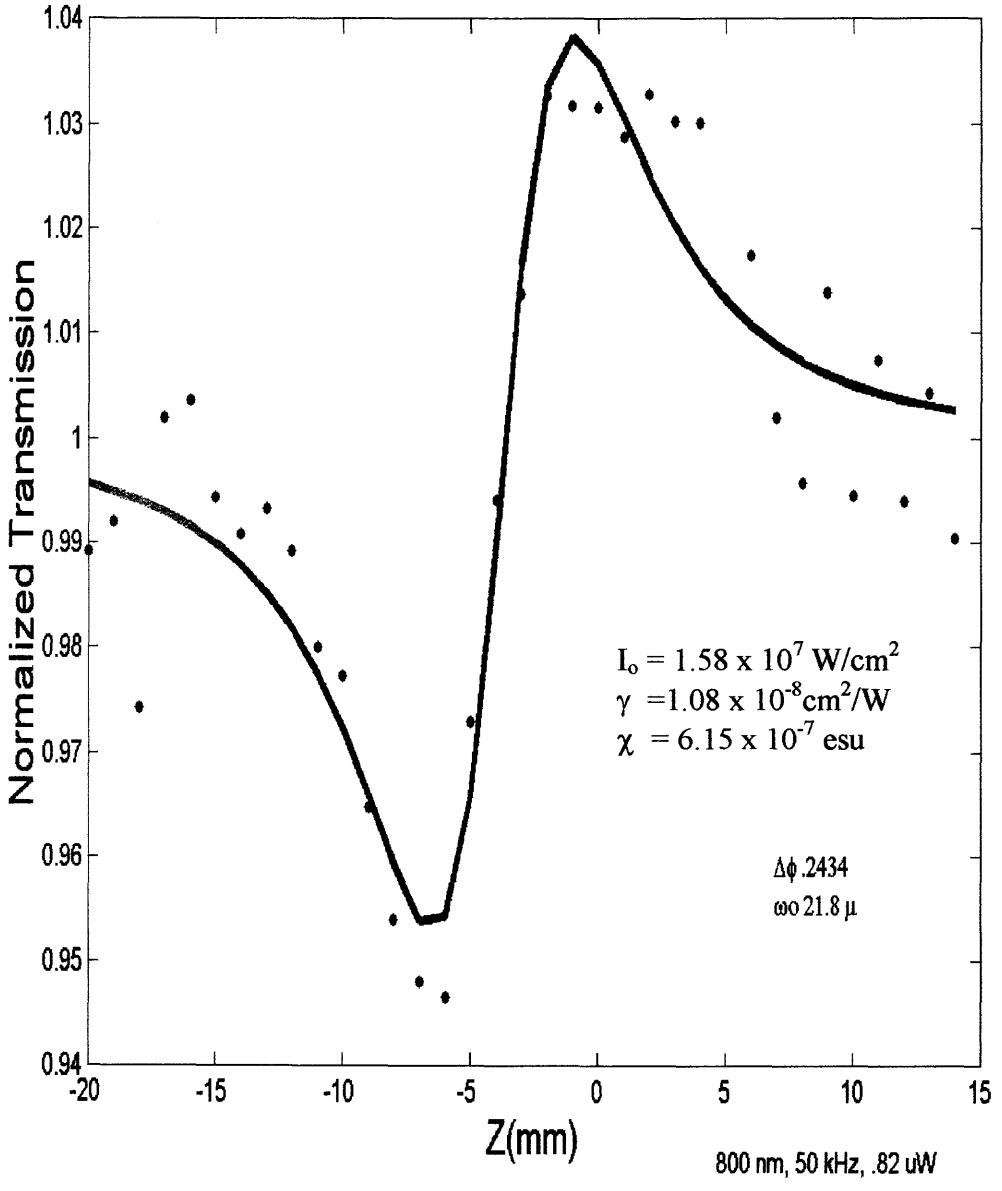

Figure 4.10 Laser ablated Si closed-apertured Z-scan @ 800 nm, 50 kHz,

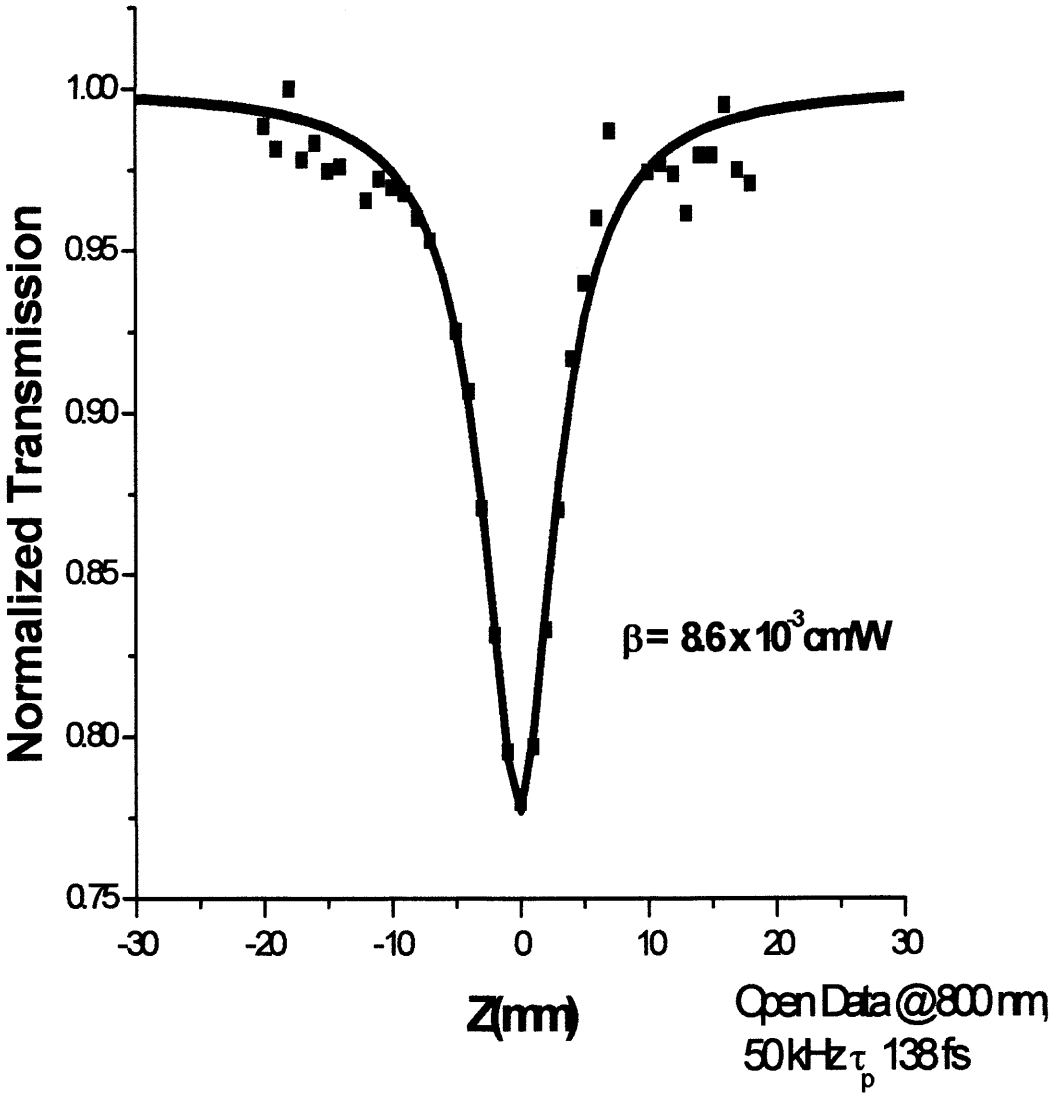

Figure 4.11. Laser ablated Si open-apertured Z-scan @ 800 nm, 50 kHz,

4.4.1 Z-scan at 532 nm

Measurements were also done using 70 ps pulses at 532 nm with a frequency doubled cw modelocked-Q-switched Nd:YAG laser at pulse train of 100MHz and a Q-switching frequency of 36 kHz. A single pulse was selected from the Q-switched envelope using a Quantum Technology Pockels cell pulse picker. A contrast ratio for the main pulse at 1064 nm was 200:1. The beam was frequency doubled with the use of a 5mm KTP crystal which greatly enhanced the contrast ratio. A digital picture was taken of the frequency doubled single pulse monitored on the screen of a Tektronix 7904 oscilloscope using an EOT fast detector with 300 ps rise time is shown in Fig. 4.12. The time scale is 100 ns per division and vertical scale is 10 mV per division. In the Z-scan setup the beam was split and the reflected light was used as a reference beam. The reference signal was used to ratio out any fluctuation in the beam's power in the Z-scan measurement. We also calibrated the setup using CS_2 in 1.6 mm cell. Based on the data, we estimated the beam spot size 52.7 μm and for n_2 1.3 x 10^{-11} esu (Fig. 4.13). This value is an excellent agreement with previously reported value (1.3 x 10^{-11} esu). [28]

For the laser ablated Si sample, an average power 6.5 mW .was used for the measurement. The calculated intensity at the peak is 5.79 x 10^7W/cm^2. Based on the fitting routine, the nonlinear phase shift (0.1742) is used to calculate γ. We calculated for γ a value of 5.56 x 10^{-10} cm^2/W and for $\chi^{(3)}_{\mathrm{Re}}$, $3.16x10^{-8}esu$ (Fig 4.14). In comparison to the value published by Vijayalaksmi et al., they estimated a value for γ to be (0.5 ± 0.13) x 10^{-7} cm^2/W for the laser ablated sample at 532 nm. There is a discrepancy of two orders of magnitude between the respective values.. We attribute this discrepancy in the nonlinearity to the thermal contribution inherent in the use of ns

pulse excitation as opposes to ps and fs pulse excitation. The good news is despite the thermal contribution, the electronic contribution to the nonlinearity still appears to be relatively large.

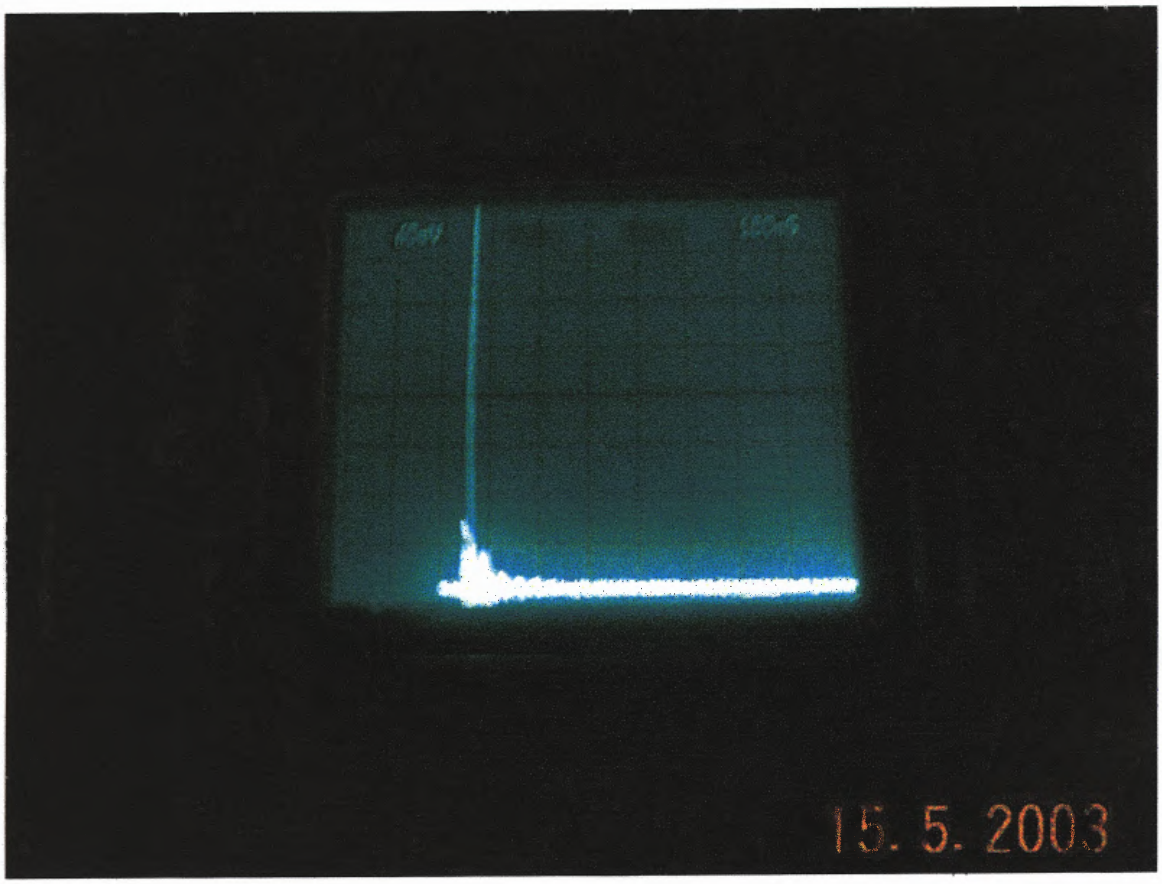

Figure 4.12. •A single pulse was selected from the Q-switched envelope using a Quantum Technology Pockels cell pulse picker

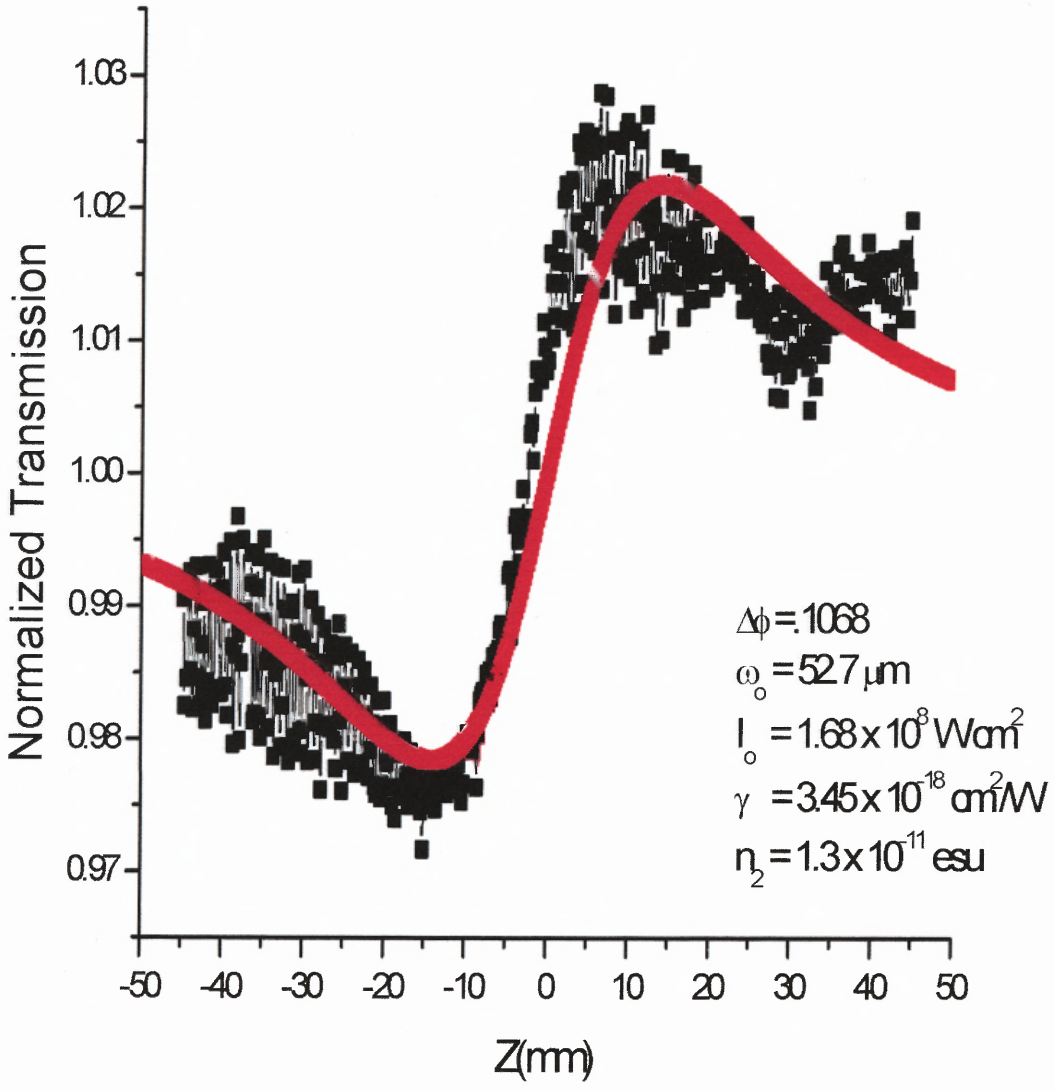

Figure 4.13 CS_2 at 532 nm

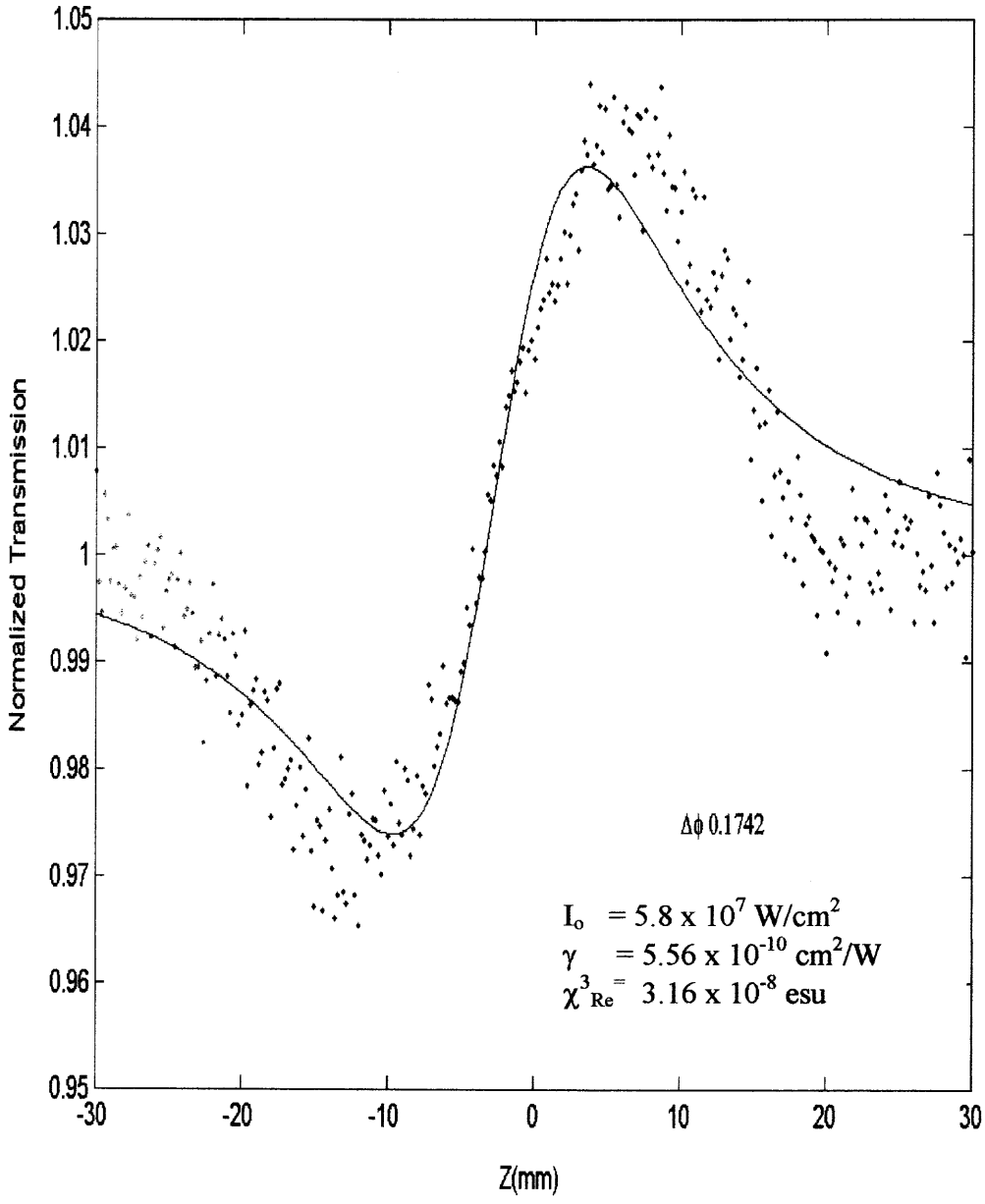

Figure 4.14laser ablated sample at 532 nm

CHAPTER 5

TEMPORAL MEASUREMENT

5.1 Pump Probe Technique

With the advent of the ultrashort pulse laser, the investigation of a medium's photo-induced changes and its lifetime as it interacts with intense light was made possible. The two main advantages of using ultrashort pulses are the high peak power at relatively low average power and the ability to observe and record the time evolution of an event on a very fine time scale limited by the temporal width of the pulse. However, since the standard electronic devices are limited in their temporal response, experimental methods are employed using the pulse itself to observe ultrafast phenomena. One method to measure the photo-induced change or response of a given medium and the duration of the response is the pump probe technique. The pump-probe experiment entails the use of two beams, which are spatially overlapped in a nonlinear medium, to measure the decay lifetime or photo-induced absorption recovery time. Additionally, with the use of a high repetition rate laser, the detection of weak signals is possible. For example, this technique makes it possible to observe events such as creation of carriers in the conduction band in a semiconducting material or induced changes to the refractive index as in glass. In the case of the glass, one studies the phase changes in the beam by looking at the diffracted beam. For the generation of carriers, the absorption changes are recorded by measuring the changes in the probe beam. The data will provide vital information of the dynamics of the system and duration of the event.[19]

In this chapter we will investigate time-resolved absorption. The detection of the induced changes of a weaker probe beam as it interacts with the stronger pump beam will be

analyzed. The two beams usually stem from the same laser source. The pump or excitation beam perturbs the medium at time t=0. The probe beam is spatially overlapped with the pump beam in the sample and the probe beam is temporally delayed and transmission of the probe beam is detected as a function of delay.

5.2 Theory

In the pump-probe beams configuration using ultra-short pulses, the amplitude and phase information can be obtained.[17,31] The detection of the probe gives information about the photo-induced absorption and the diffracted beam the phase. The measured probe signal can include both coherent and incoherent terms, where the coherent term is related to the changes in the index of refraction and therefore to the real part of $\chi^{(3)}$. The incoherent term is associated to the change in absorption and likewise to imaginary part of $\chi^{(3)}$. In the usual experimental arrangement in which the excitation and the probe pulses overlap at an angle, they create a spatial modulation or grating in the material's optical properties. If the both pulses are transformed-limited and equally coherent the photons are then scattered from the pump beam into the probe beam due to the induced grating thereby modifying the intensity of the probe beam. If the grating produced is due to the modulation of the amplitude in the electric field in the medium, i.e. changes in the absorption coefficient, then the scattered light from the excitation pulses will be in phase with the probe. Likewise, if the induced grating is created from the modulation of the phase which is directly cause by a change in the refractive index, then the scattered photons will be diffracted and will be out of phase relative to the probe. Whichever type of grating is generated from the interaction of the two beams within the material for the most part means that only the amplitude gratings will produce a

significant change in the probe beam. However, there is an exception in which the phase gratings contribute to the transmitted probe light as in the case of a material, which possesses a finite relaxation time. Therefore, if the phase difference for the pulses varies with time then the diffracted light can interact with the probe beam and thereby influence the transmitted probe's intensity.

In order to understand the changes undergone by the optical pulses within the material, we must take into account the induced change within the polarization and in our case the absorption change with respect to time, which is correlated to the modification of the probe field. The total absorption of the system is described by $\alpha(t) = \alpha_o + \Delta\alpha(t)$. The α_o term is the linear absorption at low field and the induced absorption term, $\Delta\alpha(t)$, due to the excitation beam is expressed as[17]

$$\Delta\alpha(t) = \int_{-\infty}^{\infty} I(t')A(t-t')dt' \tag{5.1}$$

where $I(t')$ is the intensity of both beams within the medium and is given by $I(t') = \left|E_{pump}(t) + E_{probe}(t)\right|$. The amplitude of the electric fields are given by $E_{pump}(t)$, $E_{probe}(t)$ where the electric field has a time dependence of e^{-iwt} and $A(t-t')$ is the impulse response of the system.[31-33]

In the case of semiconductor, the third order polarization arises from the population changes from the valence to the conduction band due to the previous pulses which modifies the linear polarization of the material and the interaction of both beams within the material as in the case of rapid dephasing. Using the nomenclature in Palfrey and Heinz's journal article, the induced third order polarization can be described as[31]

$$P_i^{(3)}(t) = E_j(t)\int_{-\infty}^{\infty} E_k^*(t')E_l(t)\left[A'_{ijkl}(t-t') + A''_{ijkl}(t-t')\right]dt' \tag{5.2}$$

In this case, the impulse response consists of two components: $A'(t-t')$ term is related to $\chi_{\mathrm{Re}}^{(3)}$ and $A''(t-t')$ to $\chi_{\mathrm{Im}}^{(3)}$. In the pump-probe scheme, both beams are normally derived from the same laser source and therefore; the probe beam is typically a weaker identical version of the pump. They are usually noncollinear and thus have different propagation $\vec{k}$ vectors. Consequently, the probe beam is then described in term of the pump beam and is given by

$$E_{probe}(t) = aE_{pump}(t-t')e^{iwt} \tag{5.3}$$

If we take the field polarization along the x-direction than the change experience by the probe energy is given by[31]

$$S(\tau) = \gamma(\tau) + \beta_1(\tau) + \beta_2(\tau) \tag{5.4}$$

where the first the first term $\gamma(\tau)$ is the incoherent signal and is equal

$$\gamma(\tau) = \int_{-\infty}^{\infty}\int_{-\infty}^{\infty} |E(t-\tau)|^2 |E(\tau)|^2 A''_{xxxx}(t-t')dt'dt \tag{5.5}$$

$\gamma(\tau)$ contains information about both the response function for the induced absorption or bleaching in the medium and the autocorrelation function of the pulse. This term does not contain any phase information leading to the changes in the index of refraction. The incoherent signal will last as long as long as it takes for the system to relax. However, the other two terms, which are coherent, will only exist as long as the pump and probe pulses are temporally overlapped. $\beta_1(\tau)$ and $\beta_2(\tau)$ are defined as[31]

$$\beta_1(\tau) = \mathrm{Re}\left\{\int_{-\infty-\infty}^{\infty}\int^{\infty} E^*(t-\tau)E(t)E^*(t')E(t'-\tau)A''_{xxxx}(t-t')dt'dt\right\} \tag{5.6}$$

and

$$\beta_2(\tau) = \mathrm{Re}\left\{\int_{-\infty}^{\infty}\int_{-\infty}^{\infty} E^*(t-\tau)E(t)E^*(t')E(t'-\tau)A'_{xxxx}(t-t')dt'dt\right\} \qquad (5.7)$$

If the beams are not mutually coherent then these terms are zero because of its inability to create a stable grating. The first term is due to the amplitude grating formed in the sample and is limited by coherence or the temporal pulsewidth of the pulse. Additionally, it only detected when the pulses are transform–limited pulses, although it has been observed in flowing cell with nontransform-limited pulses. The second term is zero for tranform-lmited pulses and its contribution is related to the phase grating. In that case, the term in the polarization relating to the change in the index of refraction is always in phase with the probe electric field and therefore will not impact the probe signal to the first order. The exception is in the case of non-transform-limited pulses where the relative phase between the pump and probe fields fluctuate as the induced polarization develops with time. Since the relative phase is not constant then the change in the index of refraction can contribute to the term in polarization that is in quaduature with the probe field and influence the transmitted probe signal.

5.3 Modeling Pump Probe Measurement

The probe transmittance is plotted with respect to the relative time delay between the probe and excitation beam. The resolution of the absorption recovery time is limited by the temporal pulse width of the probe beam. As the pump pulse excites the molecules from the ground state into the excited state, there are fewer molecules to absorb as the probe pulses passes through the sample. Hence, the medium's absorption coefficient, α_0, is decreased by $\Delta\alpha_0$. The lifetime of the excited states exists for a finite time, which indicates that the

absorption of the system recovers to its initial state. Additionally, if there is a change in the index of refraction, it also recovers before the arrival of the next excitation pulse. Usually, the excited state decays exponentially, therefore, the change in the absorption can be described as[17,34]

$$\Delta\alpha(\tau) = \Delta\alpha_0 \exp\left(\frac{-\tau}{\tau_{decay}}\right) \tag{5.8}$$

where τ is the delay after the excitation, and τ_{delay} is the excited state lifetime. Given a medium with a thickness, L, the measured probe beam average power and consequently, the intensity and pulse energy will depend on the delay and the lifetime. The intensity of the probe can be expressed as

$$\begin{aligned} I_{transmitted}(\tau) &= I_{incident} \exp\left\{-\left[\alpha_0 - \Delta\alpha_0 \exp\left(-\tau/\tau_{decay}\right)\right]L\right\} \\ &= I_{incident} \exp\{-\alpha_0 L\} \exp\left\{-\left[\Delta\alpha_0 \exp\left(-\tau/\tau_{decay}\right)\right]L\right\} \end{aligned} \tag{5.9}$$

If the change, $\Delta\alpha_0$, is small and coupled with a thin film sample then the second exponential term can be expanded using the Taylor expansion and keeping the first two term product assuming $\Delta\alpha_0 L << 1$. The probe's intensity is then written as

$$\begin{aligned} I_{transmitted}(\tau) &\approx I_{incident} \exp\{-\alpha_0 L\}\left\{1 + \Delta\alpha_0 \exp\left(-\tau/\tau_{decay}\right)L\right\} \\ &\approx I_{Transmitted}(0)\left\{1 + \Delta\alpha_0 \exp\left(-\tau/\tau_{decay}\right)L\right\} \end{aligned} \tag{5.10}$$

where $I_{transmitted}(0) = I_{incident} \exp\{-\alpha_0 L\}$. The measured transmittance change in the probe beam with respect to the time delay is

$$\frac{\Delta T(\tau)}{T_0} = \frac{\{I_{transmitted}(\tau) - I_{transmitted}(0)\}}{I_{transmitted}(0)} = \Delta\alpha_0 \exp\left(\frac{-\tau}{\tau_{decay}}\right) L \tag{5.11}$$

The experimental data are subsequently fitted with the above model.

5.4 Experimental Setup

The femtosecond experiments were conducted using an 82 MHz modelocked Ti:sapphire laser or a 50-kHz Ti:sapphire regenerative amplifier which was seeded by the modelocked Ti:sapphire laser. The beam emitted from either laser is split in half by a 50/50 beamsplitter and sent through a modified Michelson interferometer as shown in Figure 5.1. The transmitted beam enters a fixed optical path length (temporal delay). The reflected light enters a variable Newport UTM translation stage. The resolution of the stepper motor is 1 μm (~3.33fs) with a total travel of 250mm. Both beams propagate noncollinearly separated by an approximately 10° angle at the sample. Before the two beams recombine in the sample a pair of a λ/2 waveplates and polarizing prisms are placed along each path to adjust the average power. The probe beam's average power, which is delayed by the stepper motor, is reduced to 10% of the pump's power. The pump beam is modulated with the use of a mechanical chopper at 1-2 kHz, which is used as a reference by the lock-in amplifier. Both beams are focused into the sample by different lenses where the probe (f = 10 cm) is focused tighter to accommodate any spatial shift as it overlapped with the pump beam (f = 25 cm). The probe beam is detected at this modulation frequency for improved signal to ratio by a Hamamatsu silicon photodiode detector. The computer reads the signal from the lock-in amplifier

triggered by pulses from the stepper motor and plots the signal as a function of the time delay.

5.5 Calibration

A GaAs quantum well sample was used to calibrate the setup by finding the temporal (τ=0) and spatial overlap of the two beams into the medium. Observing the transmission signal of the probe pulse, the transfer of energy (modulation) from the pump to the probe can be determined. The sample responds to a broad range of wavelengths and as a result it was used to calibrate the system. A typical pump probe trace is depicted in Figure 5.2 where the calibration was performed for pulses from the Ti:sapphire laser at 82 MHz with both pump and probe beam at 790 nm.. Two time lifetimes were observed: τ_1 = 1.9 ps and τ_2 = 21.5 ps. Non-degenerate pump-probe transmission experiments were also performed by frequency doubling the 800 nm pulses to 400 nm using a 1 mm nonlinear BBO crystal. An example of a non-degenerate pump-probe signal using excitation pulses at 400 nm and probe pulses at 800nm from the Ti:sapphire regenerative amplifier at 50kHz is shown in Figure 5.3. A relaxation time was estimated to 35 ps. With degenerate 790 nm pumping the photogenerated carriers quickly thermalize to the band edge and then recombine. In contrast, the nondegenerate 400nm pulses produce photogenerated carriers high in the band with a great deal of excess kinetic energy and thus a longer time is needed to thermalize to the band edge before recombination.

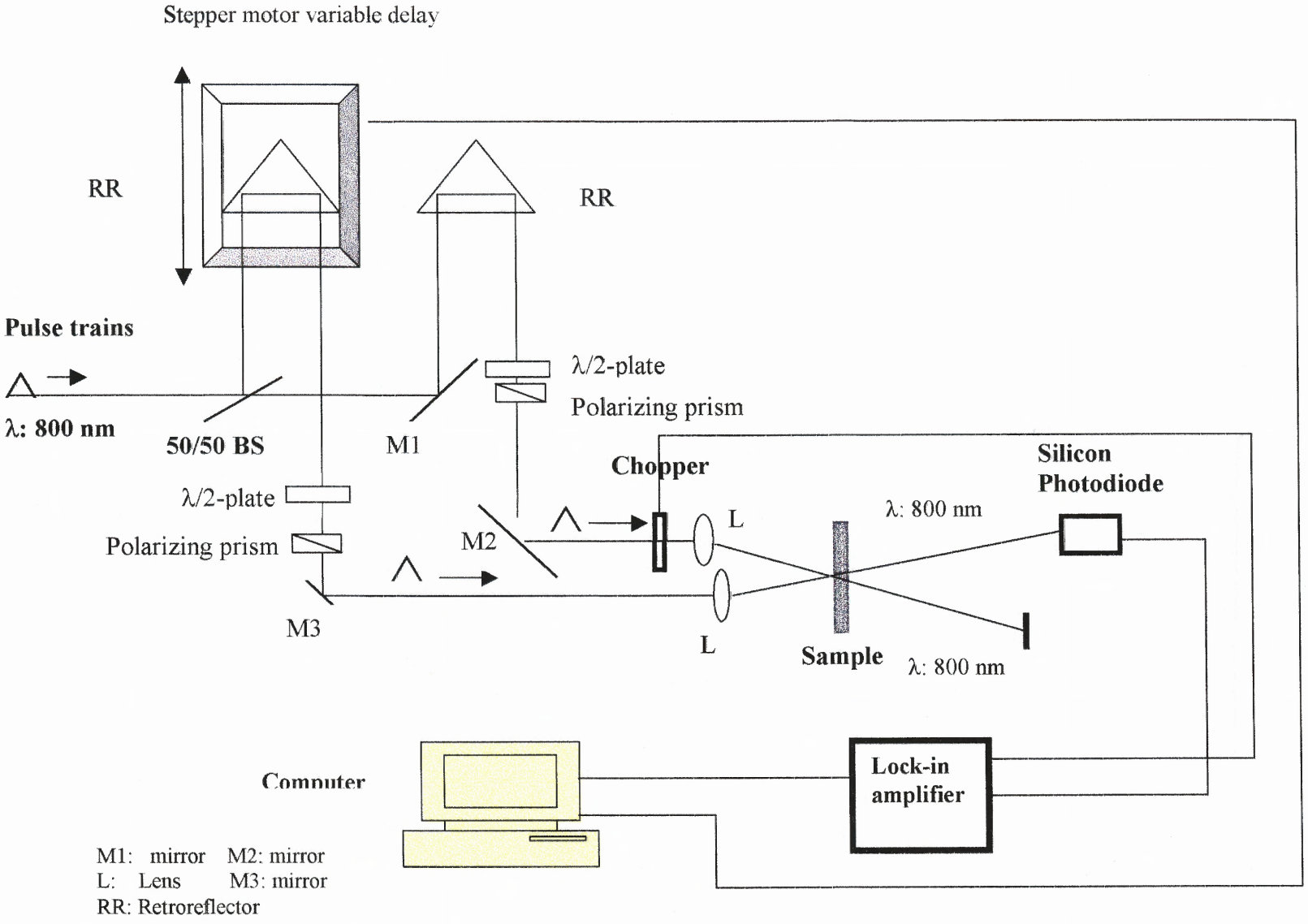

Figure. 5.1 Pump-Probe Experimental Setup

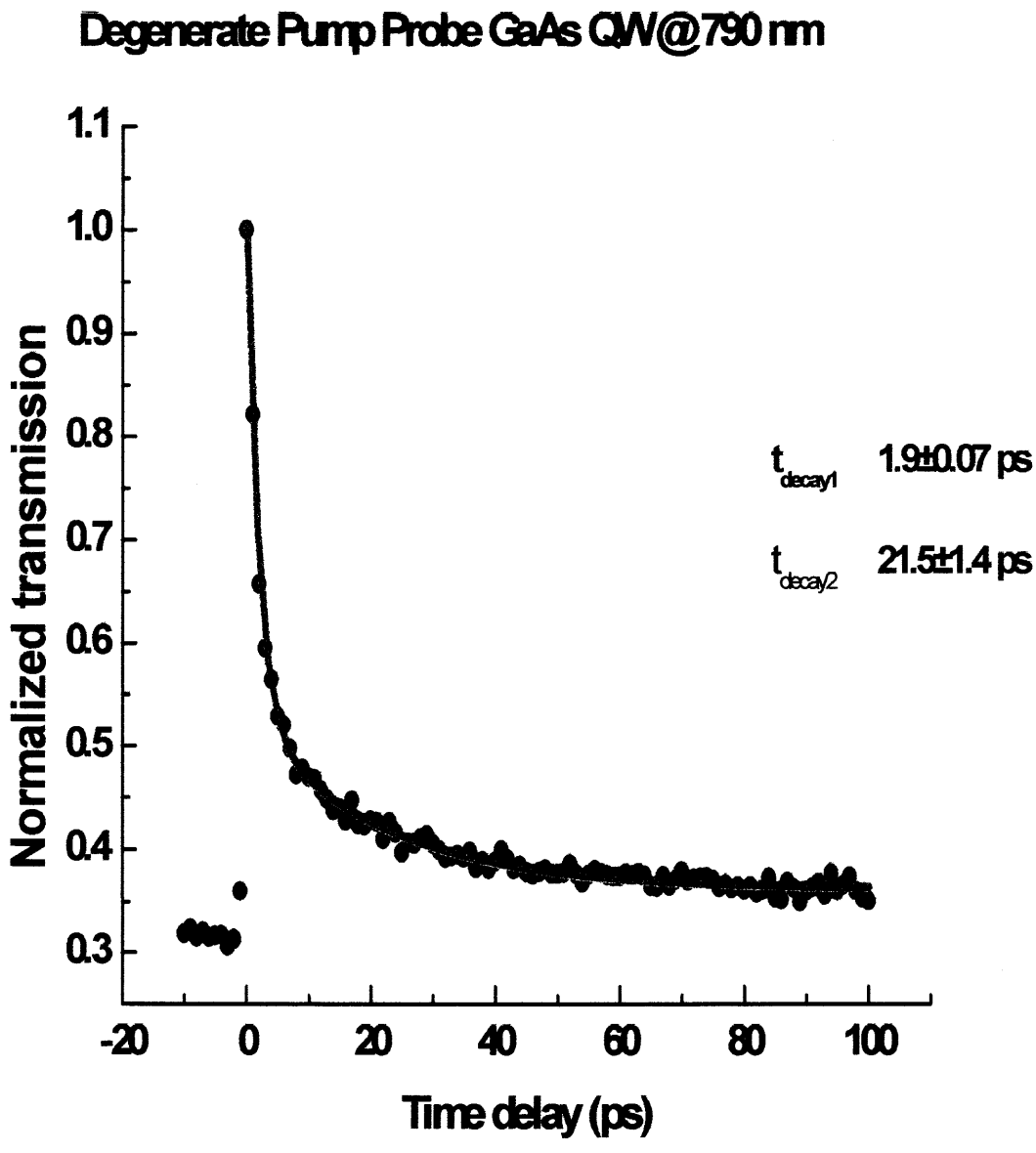

Figure 5.2 Femtosecond lifetime measurement of GaAs QWs at 790 nm

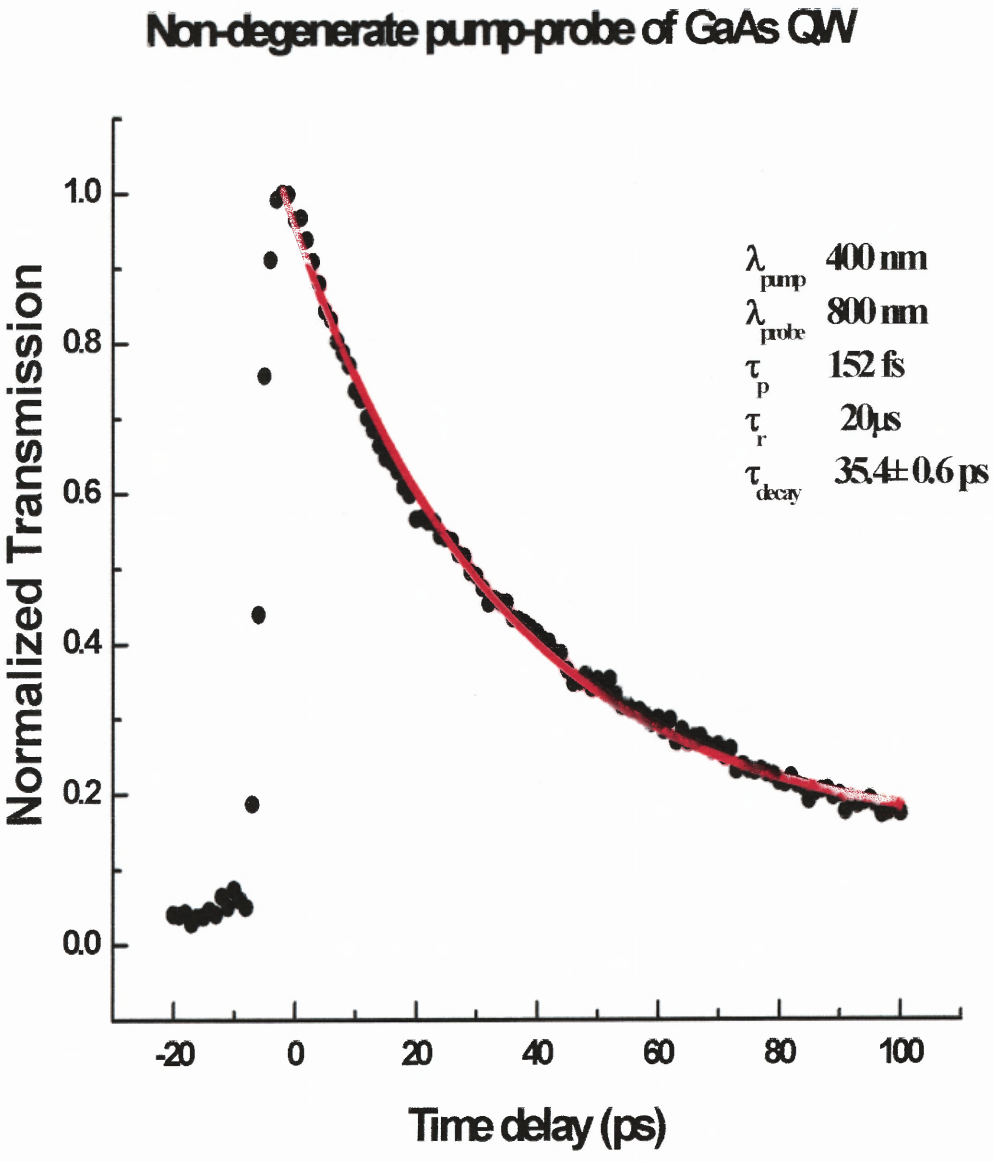

Figure 5.3 Femtosecond lifetime measurement of GaAs QWs at 800 nm with amplified pulses

5.6 Experimental Results

We initially performed the degenerate case setting both pump and probe wavelength to 810 nm, using pulses from both Tsunami and Spitfire lasers. The intensity of the pump and probe beams are 20 GW/cm^2 and 2 GW/cm^2 respectively for both laser systems. We were unable to find any pump probe signal for either the laser ablated and ion implanted samples. We were able to detect the coherent artifact for both samples limited temporal autocorrelation of the pulses. We concluded that for the ion implanted sample that the zero background implies photoexcitation too small to measure the dynamics within the sensitivity of our measurement as seen in Figure 5.4. For the laser-ablated sample (Fig 5.5) we attributed the constant background signal as indicative scattered pump signal into the detector.

The non-degenerate time resolved measurements were motivated by previous transient photo-induced measurement ion-implanted Si nanocrystals with amplified fs pulses by Klimov et al., (λ_{pump} = 400 nm, λ_{probe} = 750 nm) at Los Alomos National Laboratories.[4] For their measurement, they estimated two lifetime constants. The first short lived decay time, τ_1, was 1.5 ps and a second longer decay time, τ_2, was 8 ps. Using a similar setup, we conducted femtosecond measurement using excitation pulses at 405 nm and probe pulses at 810 nm. The pump beam was generated through second harmonic generation using a 1-mm BBO crystal. The intensity of the pump beam at the focus was $9.6\,^{GW}/_{cm^2}$ and the probe intensity was $0.89\,^{GW}/_{cm^2}$. The pulses from the 50-kHz regenerative amplifier were 160 fs pulses. In Figure. 5.6, we observed two decay times:τ_1= 2.3 ± 0.7 ps, which is attributed to the ultrafast dynamics of quantized states in the nanoclusters. The second relaxation time,τ_2= 150 ± 23 ps, is attributed to the interface states from the damage generated by the ion implantation process.

In the same setup, we examined at the laser-ablated sample with the pump at 16.8 GW/cm^2 and the probe at 1.31 GW/cm^2. A trace of the transmission of the probe is shown in Fig. 5.7 where a lifetime of 5.7 ± 0.3 ns was measured. The lifetime of the laser ablated sample is attributed to the creation of photoinduced carriers population.

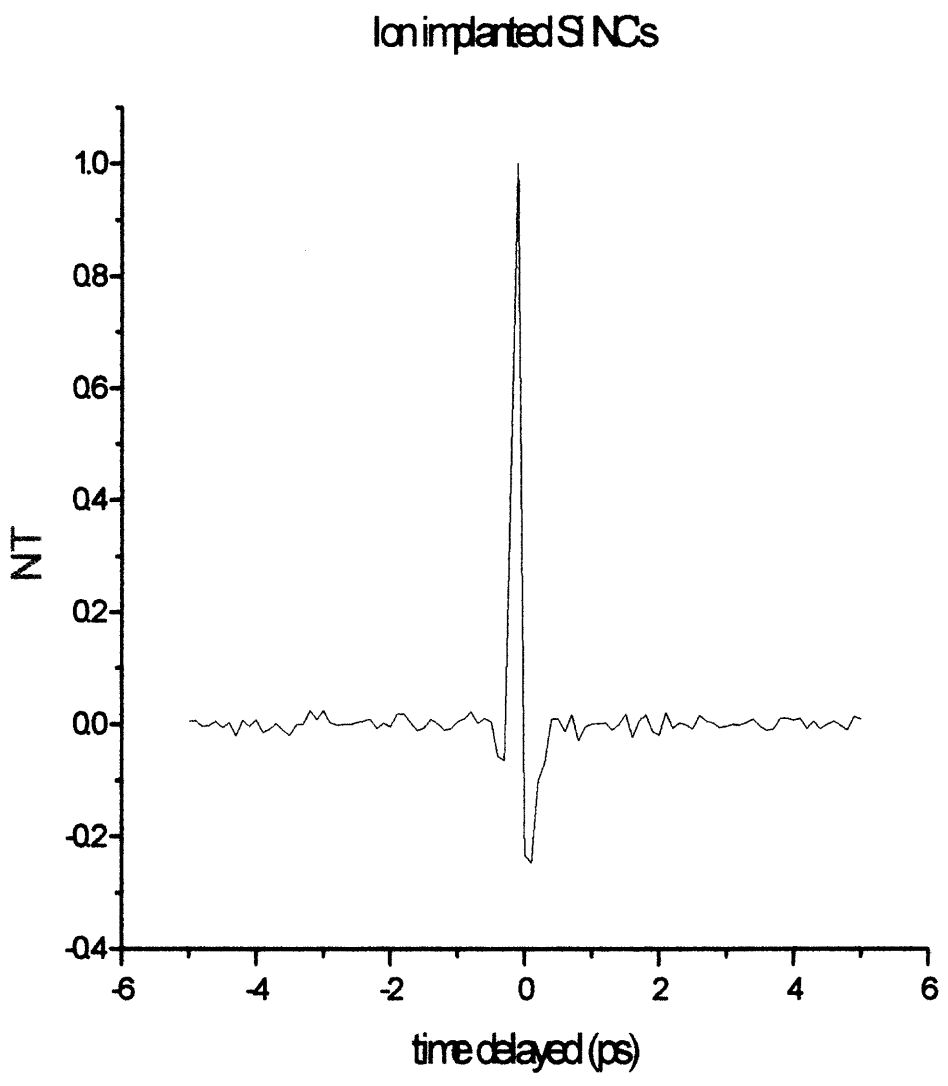

Figure 5.4 Degenerate pump probe signal of ion-implanted Si sample at 800 nm. The coherent artifact signals signifies temporal overlap of the two beams

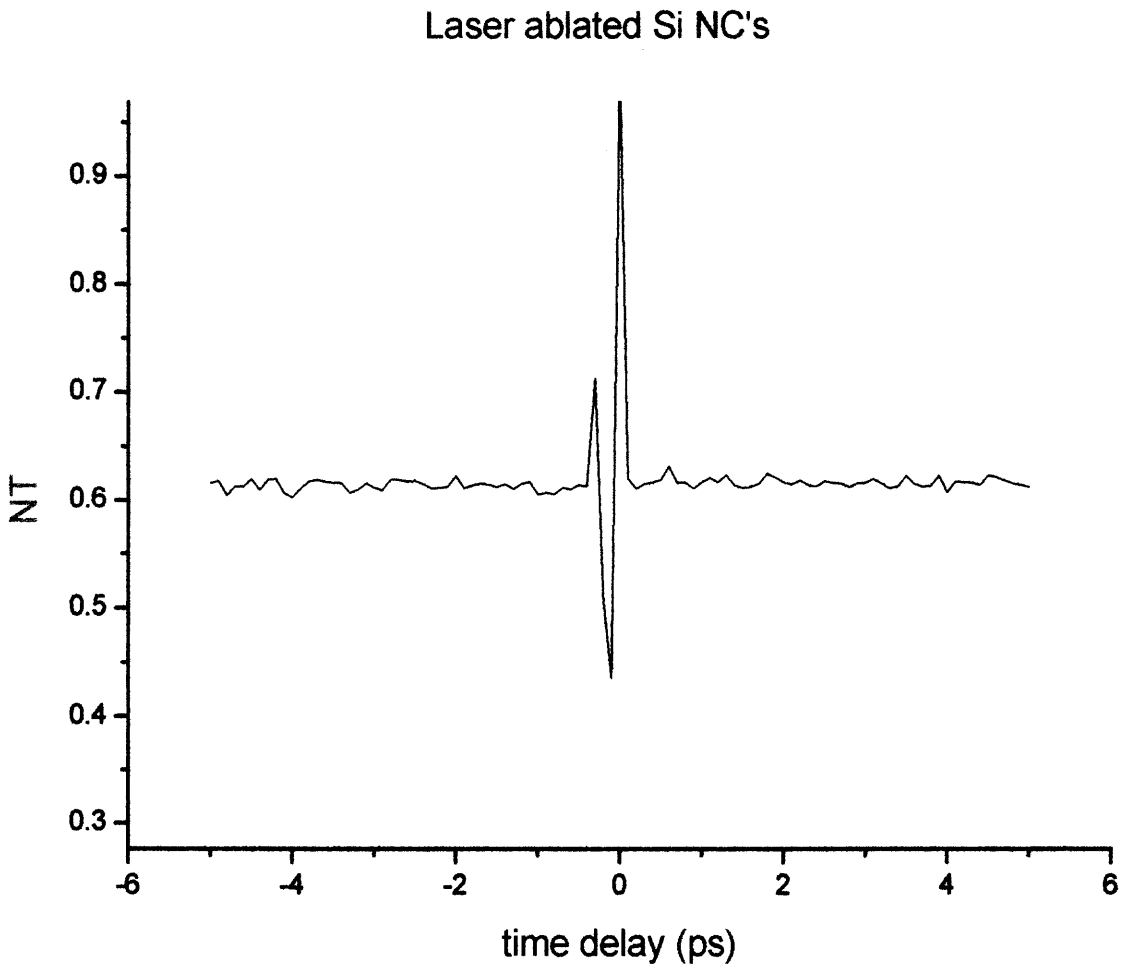

Figure 5.5 Degenerate pump probe signal of laser ablated Si sample at 800 nm. The coherent artifact signals signifies temporal overlap of the two beams

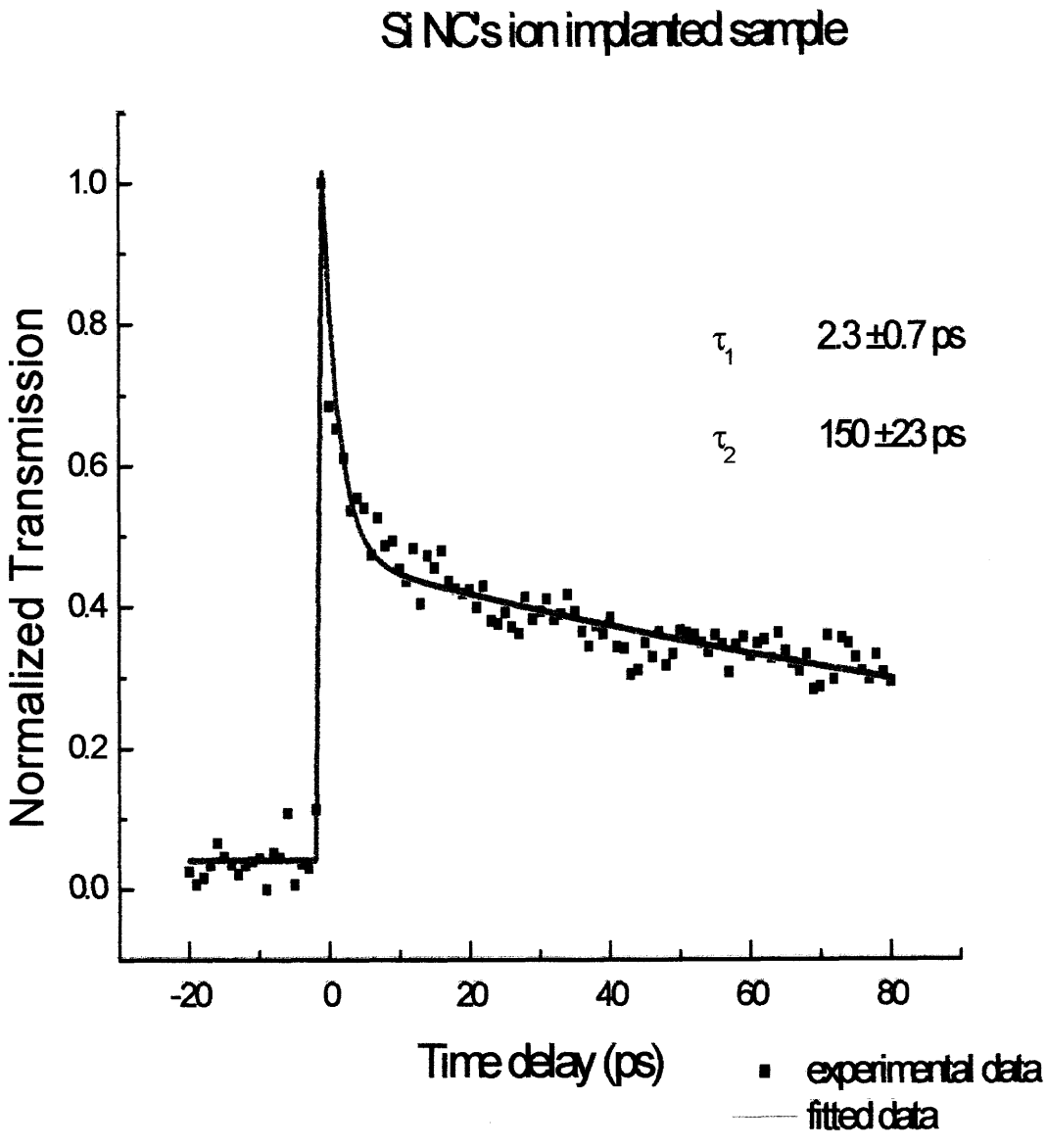

Figure 5.6 Non-degenerate time-resolved trace of ion-implanted Si sample at λpump=400nm and λprobe=800 nm

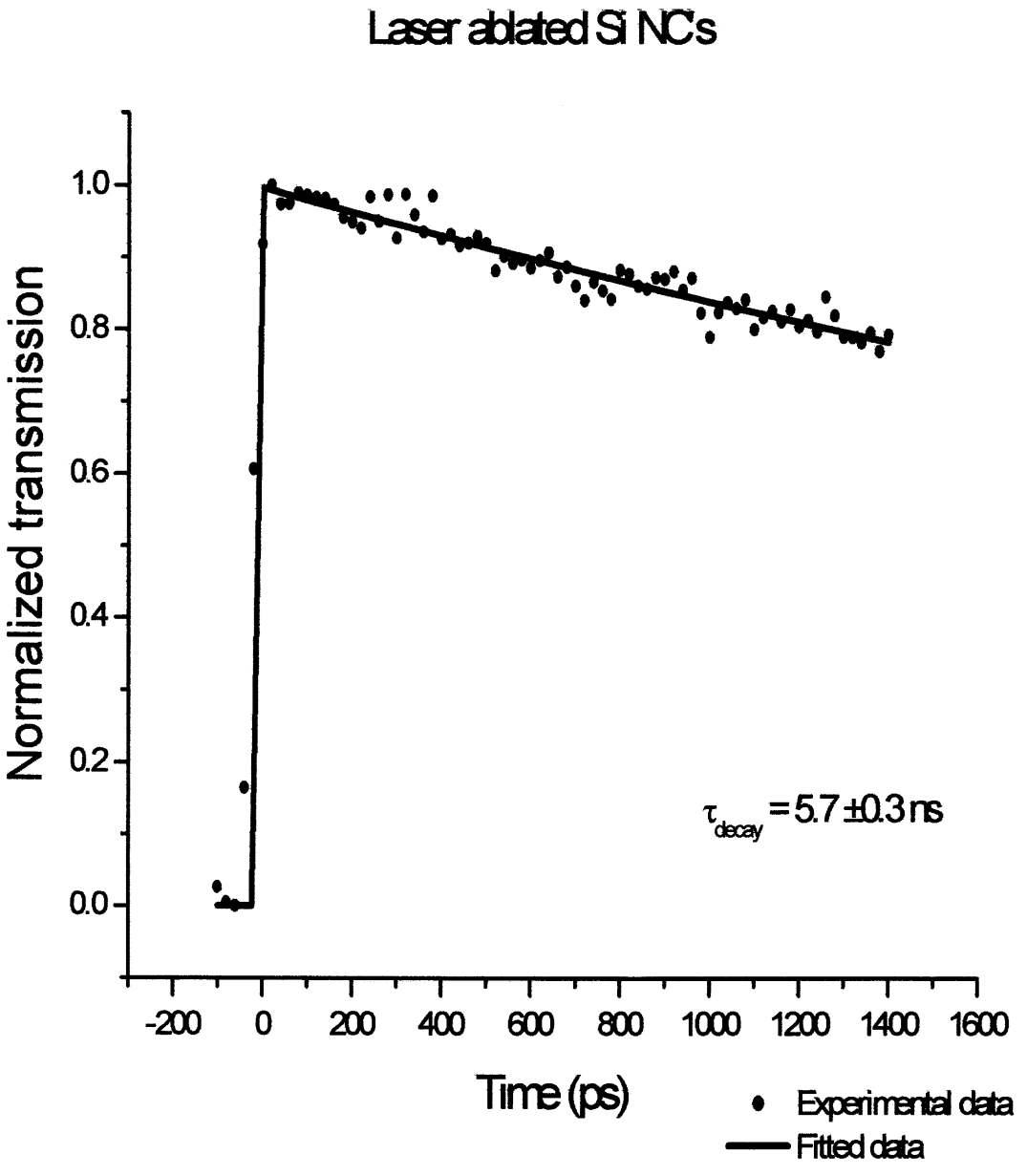

Figure 5.7 Non-degenerate time-resolved trace of laser ablated Si sample at λpump=400nm and λprobe=800 nm

5.7 Single-Wall Carbon Nanotubes (SWCNT's)

Another example of the usefulness of the pump probe technique is the estimate of the nonlinear time constant in SWCNTs. Single-wall carbon nanotubes have stimulated extensive attention due to their extraordinary electronic and optical properties.[35-38] At the same time, three-dimensional periodic structures (photonic crystals), which are able to strongly confine optical beams, have gained much interest as well. These structures are particularly attractive upon embedment of nonlinear material such as quantum silicon dots[39] germanium dots[40] or, erbium ions [41]The combination of strong optical confinement with large dispersion of the structure has been proven useful for nonlinear ultra-short pulse control.[42] Recently, well-separated SWCNTs were synthesized within the voids of an ordered array of silica spheres[43], otherwise known as opals. Thus, one hopes to combine the novel optical properties of the tubes with the unique confining environment of the three-dimensional opalline matrix.

The SWCNTs were synthesized using a CVD method at a relatively low temperature of 700° C .[39] It resulted in well-separated, mostly chiral tubes with an average diameter of 0.9 nm. Such chiral tubes are known to be of semiconductor type .[37] Ordered arrays of silica spheres served as the catalyst support matrix for the bimetallic Mo/Co particles. As the authors shall see later, these nanosize metallic clusters did not contribute to the nonlinear optical measurements. Various opal films, each made with a different silica sphere diameter, ranging between 200-650 nm, were prepared by hydrolysis of tetroethoxysilane in a mixture of ammonium hydroxide, water and ethanol.[44] A typical sample thickness was 10 μm.

Initial degenerate pump-probe data were obtained with femtosecond optical pulses. Femtosecond measurements were conducted using a modelocked Ti:sapphire laser which seeds a 50-kHz Ti:sapphire regenerative amplifier. The inset to Fig. 8 shows a typical background-free nonlinear optical autocorrelation of the 50-kHz, 800-nm pulses with duration of 160 fs, assuming a Gaussian intensity profile. Non-degenerate pump-probe transmission experiments were performed on the SWCNTs under the same condition as the laser ablated and ion implanted Si samples. Non-degenerate pump-probe transmission experiments were conducted on an array of 200 nm diameter spheres with a pump wavelength at λ=400 nm (pulse energy of 28 nJ) and a probe wavelength at λ=800 nm (pulse energy of 6 nJ). The experimental data shown in Fig. 5.8 can be fit with an exponential decay time of τ_r=319±25 fs, much longer than the laser pulse width at λ=800 nm. Pump-probe experiments were also performed with the opal alone and with the catalyst embedded in the opal and in both cases no transient transmission signal was observed. The null experiment with the metal catalyst precursor and no SWCNT eliminates the possibility of a fast nonlinear transient due to surface plasmons. The measured ultrafast decay appears to be entirely due to the presence of the SWCNT. This data is consistent with recent pump-probe experiments performed at 0.78μm/1.55μm.[40] Preliminary time resolved data in SWCNT within an ordered of silica spheres has shown a fast decay making this structure a potentially good candidate for all-optical switching. Further studies are required to examine time resolved data as a function of the photonic crystal orientation and beam polarization.

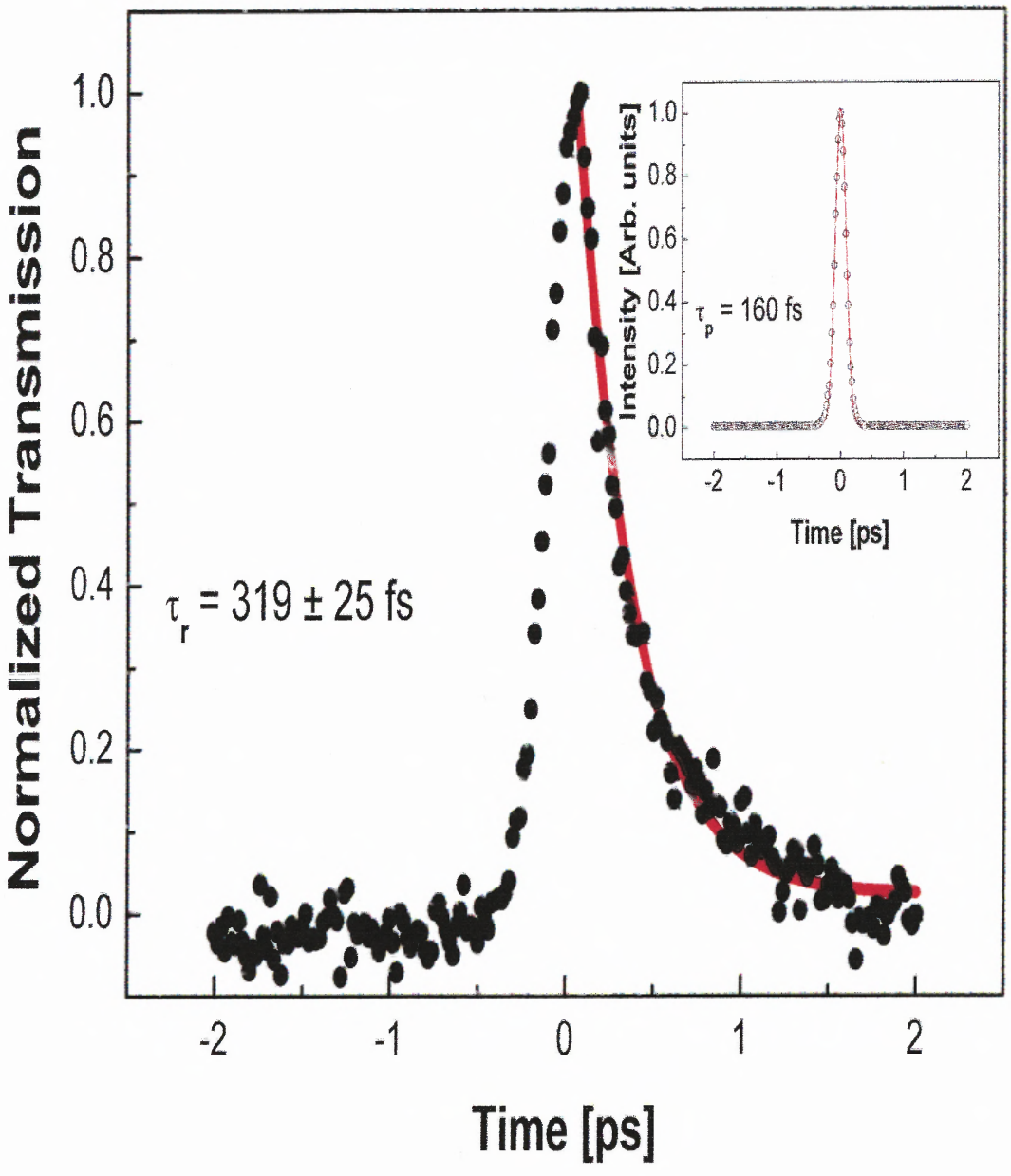

Figure. 5.8 . Pump (λ=400 nm)/Probe (λ=800 nm) experiment SWCNT's. Data (•) are exponentially fit (solid curve) with a decay time of τ_r=319±25 fs. The inset shows the autocorrelation of the probe pulse (λ=800 nm) with a pulse width of τ=160 fs.

5.7 Degenerate Four Wave Mixing

The degenerate four wave mixing technique allows one to study the change in the refractive index by creating a phase grating within the medium under investigation. In this scheme two synchronized pulses with momentum k vectors, k_1 and k_2 interfere in the sample to form a grating by spatially modulating its optical properties.[31] In the previous section the authors looked at the amplitude grating thereby measuring its photo induced absorption properties. The authors now look at the case in which a phase grating is created which in turn gives information about nonlinear index of refraction (Fig. 5.9). After the pulse interaction, the amplitude of the modulation decreases and is dependent on the dynamics due to the changes in the refractive index. To observe the phase change, a third beam, in the direction k_3, is directed into the sample and is diffracted by the grating in the direction of k_0. Where the k-vector of the diffracted beam is equal to $k_0 = k_1 - k_2 + k_3$. By varying the time delay with respect to the two excitation pulses, the time evolution of the diffracted intensity, I_D, can be measured. The diffracted intensity is given by[19]

$$I_D = \frac{\omega^2 d^2}{\varepsilon_0 n_o^4 c^4} \left|\chi^3\right|^2 \left(\frac{1-e^{-\alpha d}}{\alpha d}\right) e^{-\alpha d} I_1 I_2 I_3 \qquad (5.12)$$

The diffracted intensity is dependent on the change in the third order nonlinear susceptibility, $\chi^{(3)}$, of the medium. Where I_1, I_2, I_3 are the intensities of the three beams respectively, ω is the pulse frequency and α and L are the absorbance and thickness of the sample. The experiment was initially set-up in the forward scattering configuration as described above setting the wavelength at 800 nm.

The authors were unable to observe or detect any diffracted signals. We believe

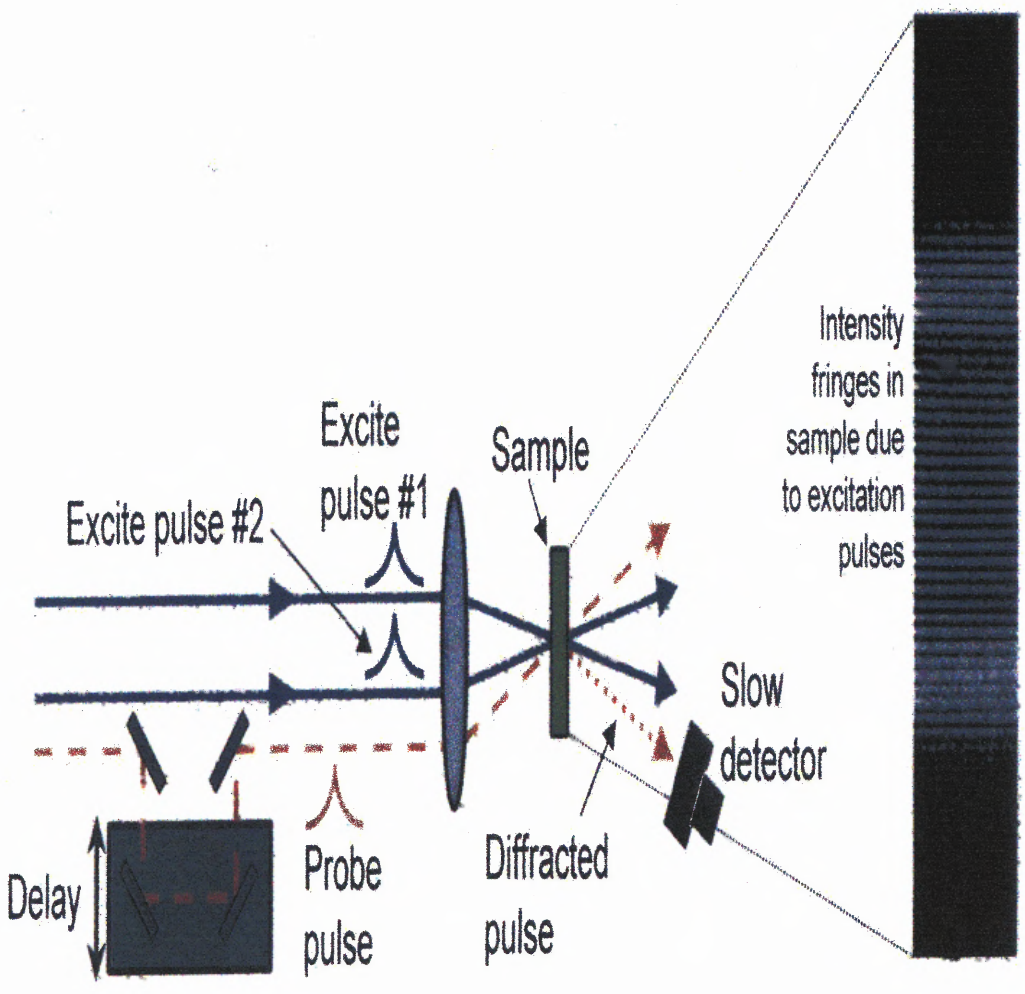

Figure 5.9. Schematic of four wave mixing experimental setup.[34]

this is due to thickness of the film, which is approximately 200 nm for the samples, and we were not able to generate a measurable diffracted signal. However, if the enhanced nonlinearity is purely due to electronic effect, the diffracted signal should be observed according to the expression for the diffraction efficiency given by[34, 55]

$$\eta(\tau) = \left[\Delta\alpha(\tau)L/4\right]^2 + \left[\Delta n(\tau)kL/2\right]^2 \tag{5.13}$$

The first term is due to the absorption (amplitude) grating generated in the sample and the second component is due to refractive index (phase) grating. Setting τ=0 corresponding to the temporal overlap of the excitation pulses. Using the experimental values (β=1.5 x 10^{-5} cm/W, γ=1.1 x 10^{-8}) obtained from the Z-scan with amplified pulses at 800 nm, the calculated value for the diffraction efficiency is 2.6×10^{-4} using the expression below

$$\begin{aligned}\eta(\tau) &= \frac{I_D}{I_3} \\ &= \frac{\omega^2 d^2}{\varepsilon_0 n_o^4 c^4}\left|\chi^3\right|^2\left(\frac{1-e^{-\alpha d}}{\alpha d}\right)e^{-\alpha d} I_1 I_2\end{aligned} \tag{5.14}$$

To easily detect the diffracted signal an efficiency of 10^{-5} is required [53]. The calculated value for the diffraction efficiency is an order of magnitude larger however; we could not experimentally detect the diffracted FWM signal. This suggests that there are other competing nonlinear effects on this time scale. One possible explanation for the failed FWM experiment, as in the case of the laser-ablated sample, is that the diffracted signal could perhaps be buried under the relatively large noise from the scattering of the pump signals into the detector, which could not be eliminated.

CHAPTER 6

CONCLUSIONS

6.1 Nonlinear optical Results

The previous chapters described the experimental work carried out to investigate the nonlinear optical properties of novel silicon structures. The major aim was to determine if the large values for the third order nonlinear susceptibility, $\chi^{(3)}$, were due to thermal or electronic contributions by studying these materials with femtosecond and picosecond pulses. Ultrashort optical pulses availed to us higher peak powers, and energy densities and also enabled us to measure ultrafast dynamics we would otherwise be unable to do with nanosecond (ns) pulses or longer.

The earlier work was done by Vijayalaksmi et. al[1-2] at NJIT with 8 ns pulses from a 10 Hz Q-switched Nd: YAG laser, which emits light at 1.06 μm. The wavelength was frequency doubled to 532 nm and frequency tripled to 355nm with the uses of nonlinear crystals[1]. They performed Z-scan measurements at 532 nm and 355 nm on both the ion-implanted and laser-ablated samples. At 355 nm, they estimated a value of nonlinear of the index of refraction, γ, 4.0 x 10^{-7} cm^2/W and a value for χ^3_{Re} 2.28x 10^{-5} esu for laser ablated Si sample. The conversion from the nonlinear index of refraction, n_2 to $\chi^{(3)}_{Re}$ is $\gamma\left(\frac{cm^2}{W}\right) = \frac{0.0395}{n_o^2}\chi^{(3)}_{Re}$.[21] At 532 nm, a value for γ was estimated at (-5 ± 0.13) x 10^{-8} cm^2/W which corresponded to a value of –2.8 x 10^{-8} esu for the real part of χ^3 for laser-ablated Si sample. For the ion-implanted Si samples, they calculated a value of γ (0.96 ± 0.25) x 10^{-8} cm^2/W ($\chi^3_{Re} = 5.5x10^{-7} esu$) at 355 nm. For the measurements done at the

532 nm, they estimated a value of $(3.7 \pm 0.9) \times 10^{-8}$ cm^2/W for the nonlinear refractive index coefficient for the ion-implanted sample.

6.2 Discussion

To investigate the source for the enhanced optical nonlinearity in novel Silicon microstructured and nanostuctured materials, we performed the same measurements with fs and ps pulses. Our results do indicate a large value for the nonlinear index of refraction, however they are 1-2 orders of magnitude smaller than the values reported with the ns pulses. For the laser-ablated sample, we performed experiments at 375 nm and compared these results to ns results at 355 nm and obtained a value of $\chi^3_{\mathrm{Re}} = -9.2x10^{-8} esu$. Our value is little over an order of magnitude smaller. For the measurement done in the green, we estimated the value for $\chi^3_{\mathrm{Re}} = 3.2\mathrm{X}10^{-8}$ based on the z-scan experiments. In comparison to the ns results, our value is two orders of magnitude smaller. The values for the nonlinear index of refraction and nonlinear absorption are tabulated in table 6.1. We attribute the discrepancy between the ns and ultrashort pulse results to processes that are not electronic in nature and occur on timescales longer than femtoseconds such as thermal effects and excited absorption or refraction due to excited free carriers.

Table 6.1 Z-scan measurements of Si nanoclusters prepared by laser ablation

cw-modelocked Ti-Sapphire laser.

λ(nm)	I_0 (W/cm^2)	Rep. Rate	τ_p	β(cm/W)	γ(cm^2/W)	$\chi^{(3)}$(esu)
790	2.9 X 10^8	82 MHz	90 fs	1.4 X 10^{-4}	2.1X10^{-9}	1.2 X 10^{-7}
375	8 x 10^8	82 MHz	70 fs	1.48 x 10^{-5}	-1.6 x 10^{-9}	-9.2 x 10^{-8}

50 KHz regenerative amplifier

800	2.9 X 10^8	50 kHz	138 fs	1.5 x 10^{-5}	1.1 x 10^{-8}	6 x 10^{-7}

Nondegenerate pump probe

λ_{pump}(nm)	λ_{probe}(nm)	Rep. Rate	τ_{decay}	τ_{decay}
405	800	50 kHZ	138 fs	5.7 ns

Q-switched cw-modelocked and frequency doubled Nd:YAG laser

λ(nm)	I_o	Rep. rate	τ_P	γ(cm^2/W)	$\chi^{(3)}$(esu)
532	5.8 X 10^7	36 kHz	70ps	5.6 X 10^{-10-}	3.2X10^{-8}

Second & third harmonics of a pulsed Q-switched Nd:YAG Laser

(Vijayalakshmi and Grebel)

λ(nm)	Rep. rate	τ_p	γ(cm^2/W)	$\chi^{(3)}$(esu)	I_0(MW/cm^2)	τ_{decay}*
532	10 Hz	8 ns	-0.5 X 10^{-7}	-2.8 x 10^{-6}	6	3.5± .5 ns
355	10 Hz	8 ns	0.7 x 10^{-8}	3.9 x 10^{-7}	6	143± 20 ns

*Limited by laser pulse width

Porous Silicon :$\chi_{Re}^{(3)}$=7.5 x10^{-9} esu[50]

Silica Fiber: $\chi_{Re}^{(3)} \approx 9 \times 10^{-14}$ esu

The samples were also investigated with amplified fs pulses at 50 kHz to determine if any thermal effects played a role. Here, we were careful to attenuate the amplified pulse to obtain the equivalent peak power at the 82 MHZ repetition rate of the Ti:sapphire laser. Effectively, we have done the same experiment at 82 MHz (12 ns pulse periods) and 50 kHz (20 μs) to estimate the thermal effects. However, because the surface of laser-ablated samples is not uniform, it produced much scattering, which affects the Z-scan signals. Additionally, the earlier laser ablated samples had a size distribution of 3-50 μm, and its effective thickness varied between 100-400 nm. The spacing between the microstructures was not uniform; therefore, depending on the area irradiated, a slightly different response occurs. However, we believe that the laser-ablated Si materials do have a greatly enhanced nonlinearity, which can be attributed to its hexagonal wurtzite structure. Although these samples are not nanostructured materials as first believed they exhibits many interesting properties. It was proposed that the enhanced nonlinearity was due to inter-cluster coupling within the microstructures.[45] However, its been determined that the crystalline composition of the laser ablated material are 75% hexagonal wursite and 25 %cubic. The large nonlinearity measured can be attributed to the concentration of the hexagonal wurtzite structure of the μm size droplets. The breakdown of symmetry from the cubic to hexagonal structural phase most likely leads to local field effects and may play a crucial role. In which case, the enhanced nonlinear optical response of the laser-ablated materials can be ascribed to the change of symmetry. In contrast to porous silicon, ($\chi^{(3)}_{Re}$ = 7.5 x 10^{-9} esu), our values are 1-2 orders of magnitude larger. For the ion-implanted Si nanocomposites we attribute the large nonlinear absorption to the

defects created by the ion implantation process. Moreover, we are unable to extract any information concerning χ^3_{Re} due to the dominate signal of the photo-induced absorption.

In a larger context, since the origin of the enhanced nonlinearity is speculative for the laser ablated Si microstructures, examining materials with a similar hexagonal wurtzite crystalline structure may give an insight into the underlying physics. In the case of cubic and hexagonal II-IV semiconductors, i.e. CdS, ZnSe, ZnS, the linear and nonlinear response has been previously studied by other groups.[46, 47] For the cubic and hexagonal structures, the structural phases are similar and equivalent up to and including the second-nearest-neighbor positions, in the limit of perfect tetrahedral bonding. It was observed that below the band gap, the structural properties played a limited role in the linear optical case. In the case of CdS, the linear optical response was for the most part independent of the crystal phase[46]. However, above the gap the reverse was true. It was concluded that the structure in the imaginary part of the dielectric tensor is sensitive to the localized regions in k space and thus more global aspects of the structure. Therefore greater difference is expected between the phases.

Although there is very little literature concerning the relationship between the crystalline structure of a material and the third order nonlinear susceptibility, there is one study that examined the correlation between the structural composition and the second order nonlinear susceptibility, χ^2. Hughes and Sipe[46] examined the second order nonlinear susceptibility of materials mentioned in the previous paragraph and determined that at half-bandgap, $E_g/2$, where the optical frequency's energy is equivalent to $E_g/2$, the values differs little from $\chi^{2(zzz)}$ of the cubic phase when specified in the same coordinate systems. They have concluded that in II-VI semiconductors that the second

order nonlinearity is independent of the structural composition particularly hexagonal.[46] The difference between the crystalline structures becomes apparent above half-bandgap for the same rationale as in the linear case. However, in the case of $\chi^{2(xyz)}$, this is not the case. For the hexagonal phase specified in the same coordinate system, the nonlinear response are different where components not allowed by symmetry in the cubic phase are in the hexagonal phase. This is attributed to the complicated nature of the nonlinear effect characterized the $\chi^{2(xyz)}$ component involving electric fields in two orthogonal directions and a polarization in the third orthogonal directions. The third order susceptibility case was not investigated however; the low symmetry of the hexagonal wurtzite may play an important role third order nonlinear optical response[46].

Krauss and Wise[48] measured the nonlinear index of refraction for CdS, ZnSe and ZnS using femtosecond pulses at 610 nm, 780 nm, and 1.27 μm. These materials were polycrystalline with the exception of CdS. Their experimental result confirmed the electronic nature of the observed nonlinearities and is given in Table 6.2[48].

Table 6.2. Measured nonlinear indices. Asterisks indicate that the signal was below the sensitivity of the experiment; these entries are upper bounds[48].

Materials	610 nm	780 nm	1270 nm
CdS	-50×10^{-12} esu	9.5×10^{-12} esu	4×10^{-12} esu
ZnSe	$<2.2 \times 10^{-12*}$ esu	10×10^{-12} esu	3.5×10^{-12} esu
ZnS	3.31×10^{-12} esu	2.1×10^{-12} esu	1.7×10^{-12} esu

They also calculated the theoretical nonlinear refractive index using a simple two-parabolic-band and the Kramers-Krönig relation, which described the nonlinear refractive as[49]

$$n_2(\omega) = \frac{K'\sqrt{E_p}}{n_o E_g^4} G_2\left(\frac{\hbar\omega}{E_g}\right) \tag{6.1}$$

The predictions based on the theoretical model fit reasonably well with the qualitative trends of their data, which also confirmed the electronic nature of the nonlinearity. However, whether or not the crystalline structure played any role has not been determined.

The pump-probe measurements were more successful. The degenerate pump probe measurements were originally at 810 nm with both 82 MHz and 50 kHz pulse trains. A coherent coupling artifact was observed in both cases. The photoexcited population was too small to measure the dynamics within the limit of our detection system, due to the extremely small sample thickness (200 nm). Earlier transient photo-induced absorption experiments on ion-implanted Si nanocrystals were performed by Klimov et. al[4]. The ion-implanted for Klimov's samples as well as ours was done by C.W. White of Oak Ridge national Laboratory. The samples, in our case, were excited by frequency-doubled light at 405 nm and probed with the fundamental at 810 nm. By pumping at 405 nm, instead of 810 nm, we were able to create enough of a photo-excited population to measure its dynamics. We were able to measure decay lifetimes for both the laser ablated and ion-implanted sample. For the laser ablated Si microstructure, we measured a decay time of 5.7 ns that is due to the photoexcited population decay. Although the lifetime is shorter than bulk silicon whose lifetime is several μs it is

consistent with the micro-Raman data (Fig. A.2). The relatively long lifetime for the laser ablated Si is consistent with the high quality crystalline like nature of microstructures. For the ion-implanted sample, two relaxation decays were measured. We observed fast decay of 2.3 ps, due most likely to the population of quantized states. It is also an indication of efficient carrier trapping at the surface and or interface states. This result indicates that the population is short-lived and decays on a ps timescale. The slower decay, τ_2= 150 ps, is most likely due to the defects at the surface due to ion implantation damage. These fast decays are also consistent with the micro-Raman data for the ion-implanted Si. In figure A.2, the width of the micro-Raman peak for the laser-ablated sample is very similar to the crystalline Si peak, which implies a high degree of crystallinity. On the other hand, the broad micro-Raman peaks for the ion-implanted samples imply a large amount of disorder due to the implant damage- this disorder is consistent with a fast optical decay time. We compared our time resolved data to the ns results. The lifetime measurements were carried out at 355 nm and 532nm using 8 ns pulses for the laser ablated samples. A lifetime of 143 ns was estimated for 355 nm and for 532 nm, 3.5± .5 ns. They concluded that this was an electronic effect. [1.2] The investigation of carrier transport of ultrafast dynamics in semiconductors is limited by the optical pulsewidth. To examine the associated lifetimes such as electron hole or intersubband scattering and optical phonons, to name a few, which occur on timescales much less than 100 ps, femtosecond pulses are required. Degenerate four wave mixing (FWM) experiments were attempted but were unsuccessful. The calculated value for the diffraction efficiency is 2.6×10^{-4}, we could not experimentally detect the diffracted FWM signal. Thus, this suggests that they are other contributions to the nonlinear index

of refraction. This can also be attributed to the small sample's thickness, which was not sufficient to generate a measurable diffracted signal.

Although extensive studies were done with both the laser ablated and ion-implanted Si, it would be interesting if further investigation can be made using degenerate pump probe measurements at 400 nm to corroborate the lifetime measurement done at 355 nm with ns pulses. A more careful study is needed to examine if any thermal contributions plays a role to the change in index of refraction. The values obtained for nonlinear index of refraction and nonlinear absorption in the present studies appear to have an electronic contribution to the nonlinearity, considering the fact measurements done with ultrashort pulses at various repetition rates gave similar results. In addition, it crucial to determine the role of the crystalline nature as it relates to the enhancement of the third order susceptibility as it does in the case of second order effect in other hexagonal wurtzite structures. Finally, further work is needed to understand the electronic band structures of the laser-ablated and ion-implanted Si materials.

APPENDIX A

RAMAN SPECTRA

Micro-Raman Spectra of Hexagonal-wurtzite

The micro-Raman spectra were obtained using 514.5 nm laser excitation with a power density of approximately 1 kW/cm^2 corresponding to <1 mW power at the sample and detected by a cooled charge coupled device array. The spectra were obtained at a spatial resolution of 1 μm and integration time of 100 s.

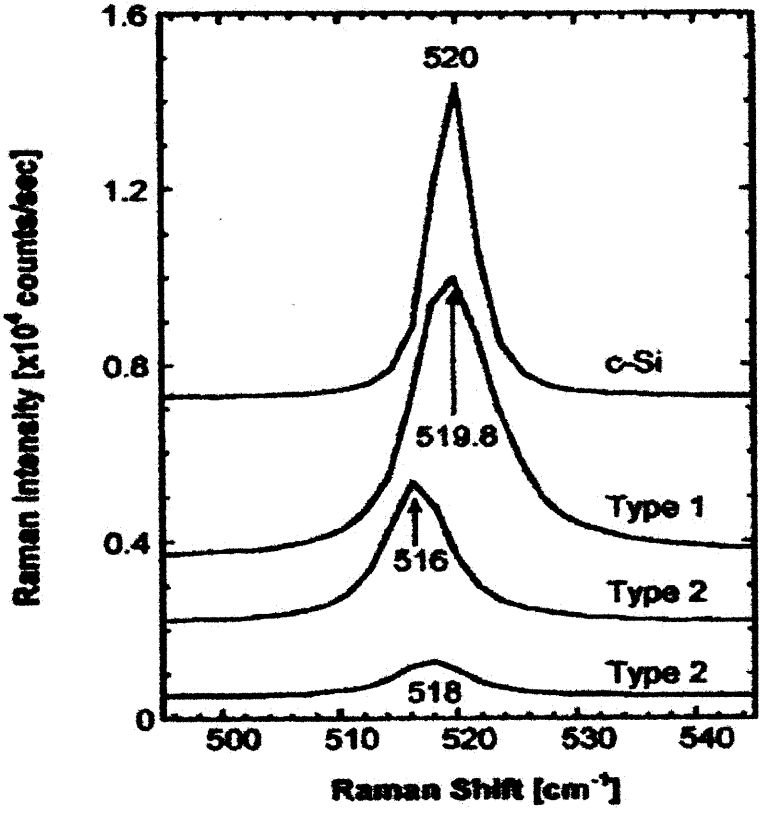

Figure A.1 Unpolarized, backscattered micro-Raman spectra for single-crystal cubic-diamond silicon (type 1) and hexagonal-wurtzite (type 2) crystallites.[51]

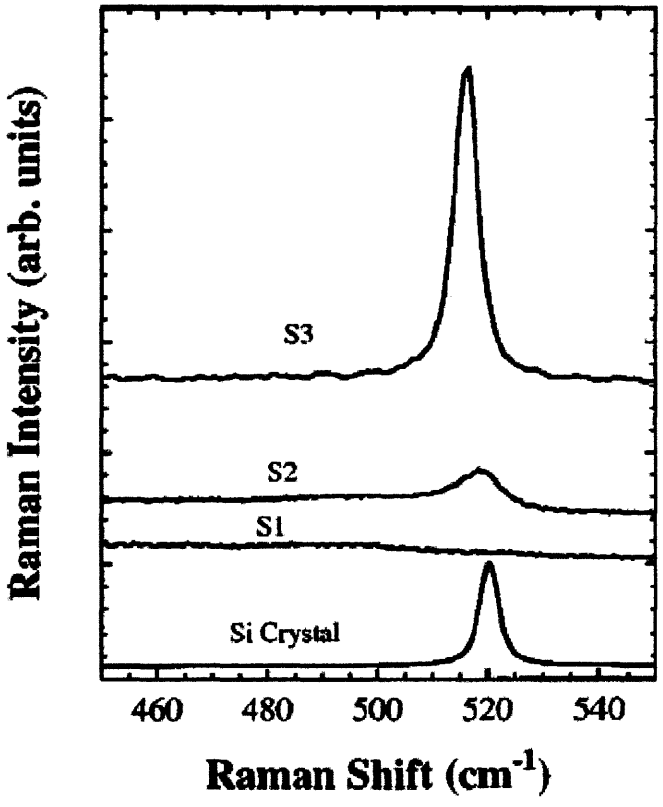

Figure A-2 Micro-Raman spectra of S1 and S2 (ion-implanted) and S3 (laser ablated) samples. Also shown is a reference signature from a <100> Si wafer.[52]

Based on the spectra, the Raman peak for the hexagonal wurtzite structure of the laser ablated Si is broader than the single cubic silicon crystal however; it still indicates the high quality crystalline nature of the laser ablated Si microstructures. In figure A-2 , the Raman data is shown for the ion implanted and laser ablated samples. The laser-ablated sample exhibited the same behavior as the previous figure. However, for the ion-implanted with a cluster mean size of 3-4 nm represented by S1, the Raman data indicated very small shift which is an indication of the disorder in the crystalline structure of the sample. For the S2 ion-implanted Si with a mean cluster size of 5-6 nm, the Raman peak is broad which indicated that it is crystalline but of poor quality which also due to the damage created by the ion implantation technique.

Microscopic Image

These images were taken at Bell Labs, Lucent using a CCD camera of the microscopic images of the ion-implanted and laser ablated Si structures. The resolution is 100 μm. These images give an illustration of the morphology of these structures.

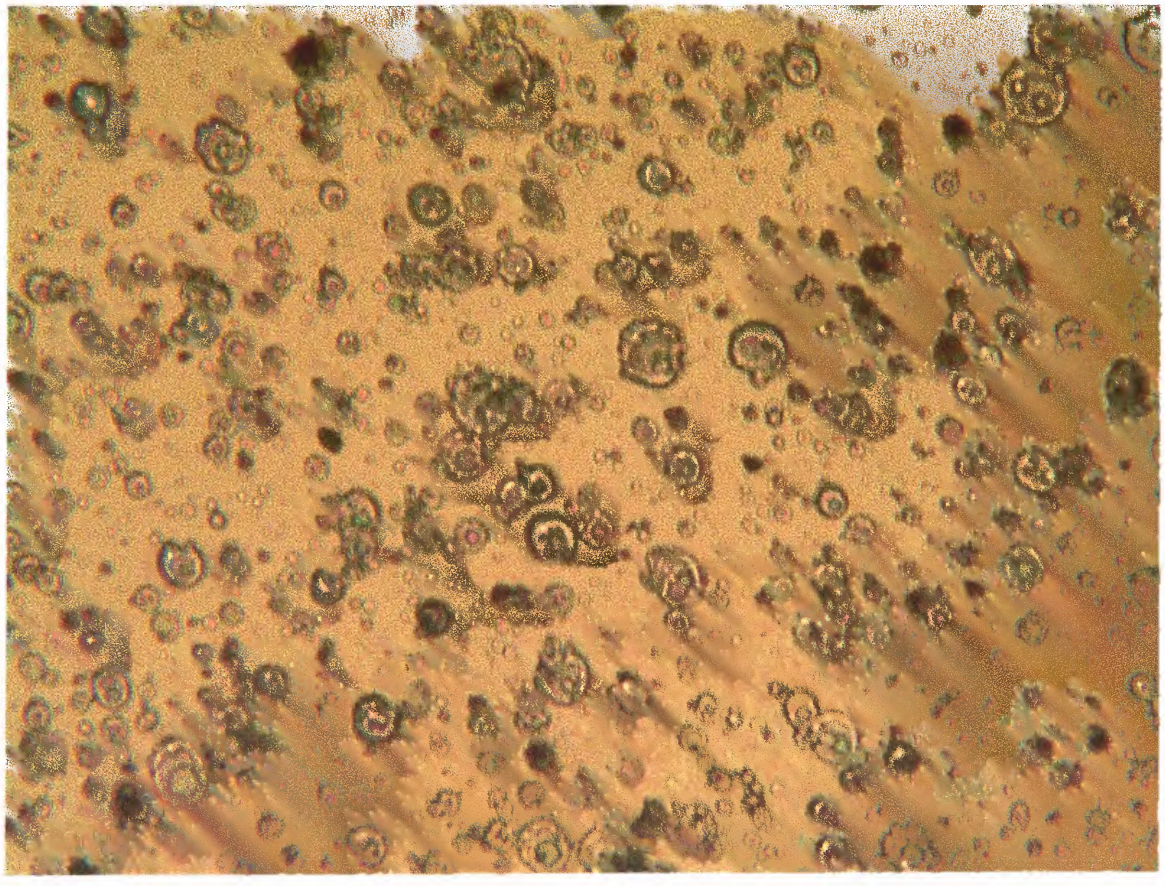

Figure A-3 Microscopic image of the laser ablated Si microstructures.

Figure A-4 Microscopic image of ion-implanted Si microstructures

APPENDIX B

Z-SCAN CALCULATION OF THE NONLINEAR INDEX OF REFRACTION COEFFICIENT

In the close aperture z-scan trace, the parameter,$\Delta\phi_o$, obtained from the curve fitting routine is proportional to the nonlinear index of refraction coefficient. $\Delta\phi_o$ is the on axis phase shift at the focus and is given by this expression

$$\Delta\phi_o = k\Delta n_o(t)L_{eff} \tag{B-1}$$

where $k = \frac{2\pi}{\lambda}$, and λ is the wavelength of the beam. Here L_{eff} is given by

$$L_{eff} = \frac{\left(1 - e^{-\alpha L}\right)}{\alpha}, \tag{B-2}$$

L is the sample thickness and α is the linear absorption coefficient. The change in the refractive index is expressed as $\Delta n_o(t) = \gamma I_o(t)$, the nonlinear refractive index coefficient is represented by γ and $I_o(t)$ is the on-axis intensity at the focus i.e., z =0. To calculate γ substitute the expression for $\Delta n_o(t)$ into equation B-1 and solve for the nonlinear refractive index coefficient. The expression for γ is

$$\gamma = \frac{\Delta\phi_o}{kI_oL_{eff}} \tag{B-3}$$

Also the correct definition of the intensity at the focus must be used. The instantaneous input power within the sample is defined as

$$P_i(t) = \frac{\pi\omega^2 I_o(t)}{2} \tag{B-4}$$

The input power is also equal to the peak power of the laser pulses and is also expressed as

$$P_{peak} = \frac{P_{avg}\tau_{rep.rate}}{\tau_p} \tag{B-5}$$

where P_{avg} is the average power of the beam, τ_p is the pulse width and $\tau_{rep.rate}$ is the pulse period of the pulse train . Therefore, equating equations B-5 and B-6 and deriving for the Io give the intensity at the focus as

$$I_o = \frac{2P_{peak}}{\pi\omega_o^2} \tag{B-6}$$

Once we calculated the intensity using the measured average power and the spot size obtained from the calibration of the well known CS_2, coupled with the value obtained from the fit for the nonlinear phase shift then we can estimate a value for the nonlinear refractive index coefficient in units of cm^2/W. The real part of the third order nonlinear susceptibility is related to γ by

$$\chi^3_{\mathrm{Re}}(esu) = 2n_o^2\varepsilon_o c\gamma = \frac{n_o^2}{0.0395}\gamma\left(\frac{cm^2}{W}\right) \tag{B-7}$$

APPENDIX C

CURVE FITTING ROUTINES

In this section, the software programs that were utilized in the curve fitting procedures are listed.

Mathematica Computer Code for Open Aperture trace for calculation β, nonlinear absorption coefficient

```
data = ReadList["temp.dat", Number, RecordLists → False]
dataplot = ListPlot[data] ;

< Statistics`NonlinearFit`
" L is the sample thickness in unit of mm"
L = 200 * 10^-6
" P is the peak power; Average Power / Rep. rate X Pulse width "
P = 30 * 10^-3 / (82 * 10^6 * 70 * 10^-15)

"λ is the wavelength in mm"
λ = 790 nm
"A is π/λ"
A = π/λ
"Parameters"
"β is nonlinear absorption coeficient in (mm/W)"
"w is the spot size also in mm"
"x is the distance from the focal point in mm"
"y is the offset from Z=0"
```

```
fitdata = NonlinearFit[data, Sum[((((-β*P*L)/(π*w^2))^n)/((1+((x+y)/(A*w^2))^2)^n*(n+1)^(3/2)), {n, 0, 1}], x,
  {{β, .0445}, {w, .029}, {y, 2}}, RegressionReport ->
   BestFitParameters, ShowProgress -> True]
fitplot = Plot[fitdata, {x, -60, 60}, PlotStyle -> RGBColor[1, 0, 0]];
bothplots = Show[dataplot, fitplot]
"Generate fit data, using the List command to obtain the
 equation for the fitted data"
List[fitdata]
"Using Range command to generate x-axis data"
M = Range[-80, 80]
"To combine the x-axis and y-axis, Tableform command is called"
R = TableForm[{M, A}, TableDirections -> {Row, Column}, TableSpacing → 1]
Export["tempout1.dat", R, "Table"]
```

This program is used to fit the open aperture Z-scan experimental data using Mathematica 4.0. From the fit the value of β can be easily obtained.

Program s for closed aperture Z-scan

```
data = ReadList["cs2red.dat", Nu...  ...ecordLists -> True]
```



```
dataplot = ListPlot[data, PlotRa...  ...ll]

<< Statistics`NonlinearFit`

λ = 532 * 10^-6
"λ is the wavelength in unit of mm"

P = π/λ
"P is a constant equal to  π/λ (mm) "
```

```
"Parameters"
"w is the spot size"
"x is Z-axis, the distant relative to the focal point of the lens"
"xo is the offset from the focus, z=0"
"ϕ is the nonlinear phase shift"

fitdata = NonlinearFit[data, 1 + 4 * ϕ * ((x-xo)/(p*w^2)) / ((1 + ((x-xo)/(p*w^2)))^2) * (9 + ((x-xo)/(p*w^2)))^2), x,
  {{ϕ, 1}, {w, .050}}, RegressionReport -> BestFitParameters,
  ShowProgress -> True, MaxIterations -> 50, PrecisionGoal -> 10]

fitplot = Plot[fitdata, {x, -50, 50}, PlotStyle -> RGBColor[1, 0, 0]];

bothplots = Show[dataplot, fitplot]

"Generate fit data, using the List command to obtain the
 equation for the fitted data"
List[fitdata]

"Using Range command to generate x-axis data"

M = Range[-80, 80]

"To combine the x-axis and y-axis, Tableform command is called"
R = TableForm[{M, A}, TableDirections -> {Row, Column}, TableSpacing → 1]

Export["tempout1.dat", R, "Table"]
```

The analysis for the pump probe data is carried out with Origin 6.1 Software package to fit the experimental data. It has a built in exponential decay fitting routine, which is used to estimate the lifetime of the photo-induced absorption.

REFERENCES

1 S. Vijayalakshmi, M. George, H. Grebel, Appl. Phys. Lett. **70,** 708 (1997).

2 S. Vijayalakshmi, M. George, H. Grebel, Appl. Phys. Lett. **71,** 3332(1997).

3 P. Bettotti, M. Cazzanelli, L. Dal Negro, B. Danese, Z. Gaburro, C. J. Oton, G. V. Prakash, L. Pavesi, J. Phys. Condens. Matter **14,** 8253 (2002).

4 V. I. Klimov, C. J. Schwarz, D. W. McBranch, Appl. Phys. Lett. **73,** 2603.

5 R. Lenz, Intro to All Optical Switching, from the World Wide Web http://www.2cool4u.ch/wdm_dwdm/intro_allopticalswitching/ intro_allopticalswitching.htm#_Toc31771910, (retrieved December, 2002).

6 B. E. A. Saleh, M. C. Teich, Fundamentals of Photonics, John Wiley & Sons, New York (1991).

7 R. E. Hummel, Electronic properties, Springer Verlag, Berlin (1998).

8 Y. Zhang, Z. Igbal, S. Vijayalakshmi, H. Grebel, Appl. Phys. Lett. **75,** 2758 (1997).

9 C. W. White, J. D. Buhai, S. P. Withrow, J. G. Zhu, S. J. PennyCook, R. A. Zuhr, D. M Hembree, D. O. Henderson, R. H. Magruder, M. J. Yacaman, G. Mordragon, S. Prawer, Encapsulated Nanocrystals and Quantum Dots Formed by Ion Beam Synthesis, Reference No. 401 for Oak Ridge National Laboratory. (unpublished).

10 S. A. Campbell, The Science and Engineering of Microelectronic Fabrication, Oxford University Press, London (1996).

11 Spectra Physics Tsunami manual (1995).

12 Spectra Physics Spitfire-50 (1995).

13 D. E. Spence, P. N. Kean ,W. Sibbett, Opt. Lett. **16,** 42 (1991).

14 S. Backus, C. G. Durfee III, M. M. Murnane, H. Kapteyn, Rev. Sci. Instrum. **69,** 1207 (1998).

15 E. B Treacy, IEEE J. Quantum Electron. **QE-5,** 454 (1969).

16 O. E. Martinez, IEEE journal of Quantum Electron. QE-23, 59, (1987).

17 E. P. Ippen, C. V. Shank, in Ultrafast Light Pulses, S.L. Shapiro, ed., Vol. **18** of Topics in Applied Physics, p. 83 Springer-Verlag, Berlin (1977).

18 J. C. M. Diels, J. J. Fonatine, I. C. Michael, F. Simoni, Appl. Opt. **24,** 1270 (1985).

19 C. Rulliere, ed., Femtosecond Laser Pulse: Principle and Experiment, Springer-Verlag, Berlin (1998).

20 P. A. Farnken, A.E. Hill, C.W. Peters, G.Weinrich, Phys. Rev. Lett. **7**, 118 (1961).

21 R. W. Boyd, Nonlinear Optics, Academic Press, New York (1992).

22 D. L. Mills, Nonlinear Optics, Springer-Verlag, Berlin (1998).

23 J. E. Sipe, R. Boyd, in Nanocomposite Materials For Nonlinear Optics Based on Local Field Effects, Vladimir M. Shalaev, ed., Vol 82 of Topics in Applied Physics, p. 1, Springer-Verlag, Berlin (2002).

24 S. Schmidt-Rink, D. A. B. Miller, D. S. Chemla, Phys. Rev. B 35, 8113 (1987).

25 W. L. Wilson, P. F. Szajowski, L. E. Brus, Science **262,**1242 (1993).

26 H. Grebel, J. Federici, S. Vijayalakshi, Linear and Nonlinear effects in Nano-scale Composites, Project Summary (unpublished).

27 R. E. Collins, Field Theory of Guided Waves, McGraw Hill, New York (1993).

28 M. Sheik-Bahae, A. A. Said, T. H. Wei, D. J. Hagan, E. W. Stryland, , IEEE. J. Quantum Electron. **QE-26**, 760 (1990).

29 G. L. Wood, E. J. Sharp, in Nonlinear Optics, R. Waynant, M.Ediger, eds., Electro-Optics Handbook, p 13.1, McGraw-Hill, New York (1994).

30 D. Weaire, B. S. Wherrett, D. A .B. Miller, S .D. Smith, Opt. Lett. **4**, 331 (1974.)

31 S. L. Palfrey, T .F. Heinz,. J. Opt. Soc. Am. B **2**, 1985.

32 S. L. Palfrey, T. F. Heinz, K. B. Eisenthal., Opt. Lett. **9**, 359 (1985).

33 C. C. Hayden, R. Trebino, Appl. Phys. B **51,** 350 (1990).

34 R. Trebino, Ultrafast Spectroscopy, from the World Wide Web http://www.physics.gatech.edu/gcuo/UltrafastOptics/UFO15.ppt (retrieved August, 2002).

35 H. Han, S. Vijayalakshmi, A. Lan, Z. Iqbal, H. Grebel, E. Lalanne, A. M. Johnson, Appl. Phys. Lett. **82**, 1458 (2003).

36 S. Iijima and T. Ichihashi, Nature (London) **363**, 603 (1993).

37 M. S. Dresselhaus, G. Dresselhaus, P. C. Eklund, Science of Fullerenes and Carbon Nanotubes, Academic, New York (1996).

38 A. Thess, R. Lee, P. Nikolaev, H. Dai, P. Petit, J. Robert, C. Xu, Y. H. Lee, S. G. Kim, A. G. Rinzler, D. T. Colbert, G. E. Scuseria, D. Tomanek, J. E. Fischer, R. E. Smalley, Science, **273**, 483 (1996).

39 M. Ajgaonkar Y. Zhang, H. Grebel, C. W. White, Appl. Phys. Lett. **75**, 1532 (1999).

40 M. Ajgaonkar, Y. Zhang, H. Grebel, R. A. Brown, J. Opt. Soc. Am. B **19**, 1391 (2002).

41 M. Ajgaonkar Y. Zhang, H. Grebel, M. Sosnowski, D. C. Jacobson, Appl. Phys. Lett. **76**, 3876 (2000).

42 S. Vijayalakshmi, H. Grebel, G. Yaglioglu, R. Pino, R. Dorsinville, C. W. White, Appl. Phys. Lett. **78,** 1754 (2001).

43 A. D. Lan, Z. Iqbal, A. Aitouchen, M. Libera, H. Grebel, Appl. Phys. Lett. **81**, 433 (2002).

44 A. A. P. Phillipes, J. Mat. Sci. Lett. **8**, 1371 (1987)

45 Z. Iqbal, S. Vijayalakshmi, H. Grebel, Nanostructured Materials **12**, 271 (1999).

46 J. L. O. Hughes, J. E. Sipe, Phys. Rev. B, **58**, 7761 (1998).

47 B. Jensen, A. Torabi, J. Opt. Soc. Am. B, **3**, 857 (1986).

48 T. D. Krauss, F. Wise: Appl. Phys. Lett. **65**, 1739 (1994).

49 M. Sheik-Bahae, D.J. Hagan, E.W. Van Stryland, Phys Rev. Lett. **65** (1990).

50 F. Z. Henari, K. Morgenstern, W. J. Blau, V. A. Karavanskii ,V. S. Denprovskii, Appl. Phys. Lett. **67**, 323 (1995).

51 Y. Zhang, Z. Iqbal, S. Vijayalakshmi, H. Grebel, Appl. Phys. Lett. **75**, 2758 (1999).

52 S. Vijayalakshmi, H. Grebel, Z. Iqbal, C. W. White, J. Appl. Phys. **84**, 6502 (1998).

53 H. J. Eichler, P. Günter, D. W. Pohl, Laser-Induced Dynamic Gratings, Springer-Verlag Berlin (1986).